1990

Measurement of Positron-Electron Going to Baryon-Antibaryon Forward-Backward Charge Asymmetry.

Jit Ning Lim
Louisiana State University and Agricultural & Mechanical College

INFORMATION TO USERS

The most advanced technology has been used to photograph and reproduce this manuscript from the microfilm master. UMI films the text directly from the original or copy submitted. Thus, some thesis and dissertation copies are in typewriter face, while others may be from any type of computer printer.

The quality of this reproduction is dependent upon the quality of the copy submitted. Broken or indistinct print, colored or poor quality illustrations and photographs, print bleedthrough, substandard margins, and improper alignment can adversely affect reproduction.

In the unlikely event that the author did not send UMI a complete manuscript and there are missing pages, these will be noted. Also, if unauthorized copyright material had to be removed, a note will indicate the deletion.

Oversize materials (e.g., maps, drawings, charts) are reproduced by sectioning the original, beginning at the upper left-hand corner and continuing from left to right in equal sections with small overlaps. Each original is also photographed in one exposure and is included in reduced form at the back of the book.

Photographs included in the original manuscript have been reproduced xerographically in this copy. Higher quality 6" x 9" black and white photographic prints are available for any photographs or illustrations appearing in this copy for an additional charge. Contact UMI directly to order.

U·M·I

University Microfilms International
A Bell & Howell Information Company
300 North Zeeb Road, Ann Arbor, MI 48106-1346 USA
313/761-4700 800/521-0600

Order Number 9112246

Measurement of $e^+e^- \rightarrow b\bar{b}$ forward-backward charge asymmetry

Lim, Jit Ning, Ph.D.

The Louisiana State University and Agricultural and Mechanical Col., 1990

U·M·I
300 N. Zeeb Rd.
Ann Arbor, MI 48106

Measurement of $e^+e^- \rightarrow b\bar{b}$ forward-backward charge asymmetry

A Dissertation

Submitted to the Graduate Faculty of the

Louisiana State University and

Agricultural and Mechanical College

in partial fulfillment of the

requirements for the degree of

Doctor of Philosophy

in

The Department of Physics and Astronomy

by

Jit Ning Lim

B.S., National University of Singapore, 1984

M.S., Louisiana State University, 1986

August 1990

Acknowledgments

For the education which allows me the freedom to pursue my hopes, dreams and aspirations, I owe a great debt to my family. My sincerest thanks to my parents, Lim Heng Say and Tan Tew Hiew, who devoted their lives to their children; to my sisters and brother who sacrificed their education and took early work so that I might continue, Tuay Cheng, Toi Ming, Mui Kim and Boon Tong; to my professors Richard Imlay, Bill Metcalf and Richard Haymaker who made it possible for me to come to America to study; to my thesis advisor, Professor Roger McNeil, for his encouragement, guidance and immense patience in reading this thesis countless times over and giving valuable insights into the various aspects of the analysis; to Dr. Kazuo Abe and Dr. Hiroyuki Sagawa who taught me much about Experimental Physics while I was in Japan so I didn't sink into total "whale shit"; to Professor Stephen Olsen and Dr. Aki Maki for their leadership in providing an excellent enviroment for serious research; to all the members of AMY who built the detector and wrote the detector-specific software; especially Roger McNeil, S. Igarashi, S.S. Myung and N.M. Shaw for the work they have done on the muon analysis, T.Kumita for his work on punchthrough, H. Sagawa and T. Mori on their work on total hadronic cross-section; my analysis is built upon a part of theirs. My wife and I give thanks to Professor Stephen Olsen who allowed the graduate students the use of "Rochester" truck for survival; to Yosida-san who kept my wife and I alive clearing red tape at the hospital; to Dr. Aki Maki who called the ambulance when

I was ill and for staying many hours with us, and to Delores Hart who made all arrangements at LSU on our behalf. Finally and most dearly I thank Eden, my wife, lover, teacher and companion of life, for her support and love and for sharing the good times and the hard times. She is the "wind beneath my wings."

To Victoria Mai-Ying Eden Elizabeth Mountbatten-Lim

Table of Contents

List of Tables

Abstract

This dissertation describes the measurement of the forward-backward charge asymmetry, A_b, for $e^+e^- \rightarrow b\bar{b}$ at TRISTAN by the AMY detector. A measurement of the ratio, R_b, of the cross section for $e^+e^- \rightarrow b\bar{b}$ to the theoretical QED cross section for $e^+e^- \rightarrow \mu^+\mu^-$ is also obtained. A_b is an effect of the weak-electromagnetic interference. The measurement of A_b is therefore a direct test of the standard model electroweak theory. TRISTAN is the only e^+e^- collider in the world to explore the center-of-mass energy region of 50 GeV to 62 GeV, where the effects of weak-electromagnetic interference becomes maximum. The data were collected between June 1987 and July 1989 with a total integrated luminosity of 33.3 pb^{-1} and center-of-mass energies ranging from 52 GeV to 61.8 GeV. Multihadronic events with a muon were used for the analysis. The measured values were

$A_b = -0.82 \pm 0.25(\text{stat}) \pm 0.14(\text{syst})$ and $R_b = 0.47 \pm 0.12 \pm 0.12$ at an average center-of-mass energy of 57.2 GeV. These results were consistent with the standard model electroweak theory predictions of $A_b = -0.58$ and $R_b = 0.56$ at this energy. The measurement of the charge asymmetry is used to set a limit on $B^0 - \overline{B}^0$ mixing of $\chi < 0.20$ at the 90% confidence level.

Chapter 1

Introduction

According to the standard model, the fundamental particles of the universe consist of spin-half quarks and leptons which come in at least six "flavors". Each particle has an anti-particle counterpart which has the same mass, but opposite quantum numbers. The quarks and leptons form left-handed doublets and right handed singlets as shown in figure 1.1.

Interactions among these fundamental particles are of four types: strong, electromagnetic, weak and gravitational.

The strong interaction originates from a hidden "color" charge carried by quarks and the theory of the strong interaction is known as Quantum Chromodynamics (QCD). Leptons do not carry color charges and therefore are not affected by the strong interaction. The weak and electromagnetic interactions are low energy manifestations of a single unified electroweak interaction. The electroweak theory is

$$\begin{pmatrix} u \\ d \end{pmatrix}_L \quad \begin{pmatrix} c \\ s \end{pmatrix}_L \quad \begin{pmatrix} t \\ b \end{pmatrix}_L \qquad \textit{quark doublets}$$

$$\left(u \right)_R \quad \left(d \right)_R \quad \left(c \right)_R \quad \left(s \right)_R \quad \left(t \right)_R \quad \left(b \right)_R \qquad \textit{singlets}$$

$$\begin{pmatrix} \mathrm{e}^- \\ \nu_e \end{pmatrix}_L \quad \begin{pmatrix} \mu^- \\ \nu_\mu \end{pmatrix}_L \quad \begin{pmatrix} \tau^- \\ \nu_\tau \end{pmatrix}_L \qquad \textit{lepton doublets}$$

$$\left(e^- \right)_R \quad \left(\mu^- \right)_R \quad \left(\tau^- \right)_R \qquad \textit{singlets}$$

Figure 1.1: Families of quarks and leptons

based on the SU(2) × U(1) gauge group. QCD combined with this electroweak theory is referred to as the "standard model".

In spite of its remarkable successes in explaining a wide range of experimental phenomena, the standard model still has many problems. It is complicated and unable to predict fundamental constants such as masses of quarks and leptons, nor is it able to explain the fact that electric charges of the electron and proton have the same magnitude but opposite sign. The family classification of quarks and leptons is not well understood since matter is made almost entirely of particles from the first of the three families, nor is it understood why there are three families of quarks and leptons. It does not explain the one to one correspondence between the quark and lepton flavors. Also, the t quark and ν_τ which are required to complete the third quark and lepton family have yet to be observed experimentally.

Thus experimental tests of the standard model are extremely important and are carried out at all the major accelerators today.

The standard electroweak model makes an absolute prediction for the forward-backward charge asymmetry (A_f) for the process $e^+e^- \rightarrow f\bar{f}$ (where f is a quark or lepton). A_f is due to the interference between the weak interaction mediated by the neutral boson Z^0 and the electromagnetic interaction mediated by the photon (figure 1.2). Therefore a direct measurement of A_f is an unambiguous test of the standard electroweak theory. A_f is energy dependent and is defined by

$$A_f = \frac{N_F - N_B}{N_F + N_B} \tag{1.1}$$

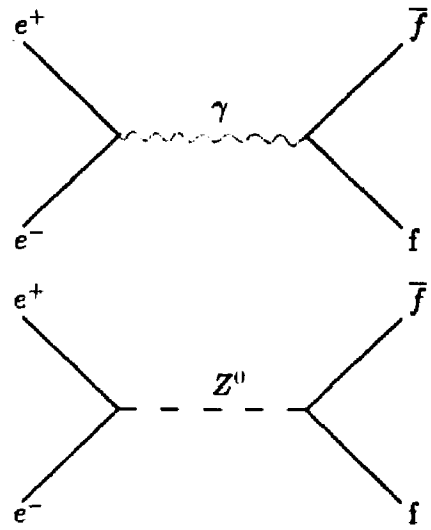

Figure 1.2: Feynmann diagrams for $e^+e^- \rightarrow f\bar{f}$: The forward-backward asymmetry is due to the interference between these two contributions.

where N_F and N_B are the number of f's produced in the forward and backward region respectively (figure 1.3). The forward direction is defined by the direction of the e^- beam.

This dissertation describes the measurement of the forward-backward charge asymmetry (A_b) for the process $e^+e^- \rightarrow b\bar{b}$ at TRISTAN by the AMY detector. A measurement of the ratio of the cross-section for $e^+e^- \rightarrow b\bar{b}$ to the lowest order theoretical QED cross-section for $e^+e^- \rightarrow \mu^+\mu^-$ (R_b) is also obtained. R_b is given by

$$R_b = \frac{\sigma(e^+e^- \rightarrow b\bar{b})_{\text{measured}}}{\sigma(e^+e^- \rightarrow \mu^+\mu^-)_{\text{QED}}} \tag{1.2}$$

Measurements for $e^+e^- \rightarrow b\bar{b}$ made at center-of-mass energies of 29 - 43 GeV at

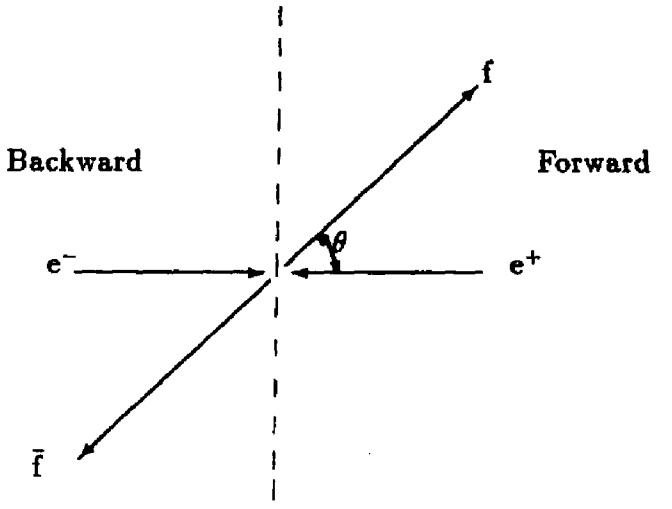

Figure 1.3: Forward-Backward region

PEP and PEPTRA [1] are shown in figure 1.4. The best results were obtained by the JADE and MAC collaborations. JADE's result of $A_b = -0.228 \pm 0.06 \pm 0.025$ agrees with the standard model prediction of -0.252. However, MAC's measurement of $A_b = 0.034 \pm 0.070 \pm 0.035$ differs from the standard model prediction of -0.16 (unless substantial $B^0 - \overline{B}^0$ mixing is assumed).

An independent measurement of A_b by AMY is therefore timely and important. This measurement by AMY is also interesting since TRISTAN operates in the center-of-mass energy region where A_b is expected to be at its maximum negative value (figure 1.4).

Topless models

The standard model assums that the b and t quarks are members of a left-handed

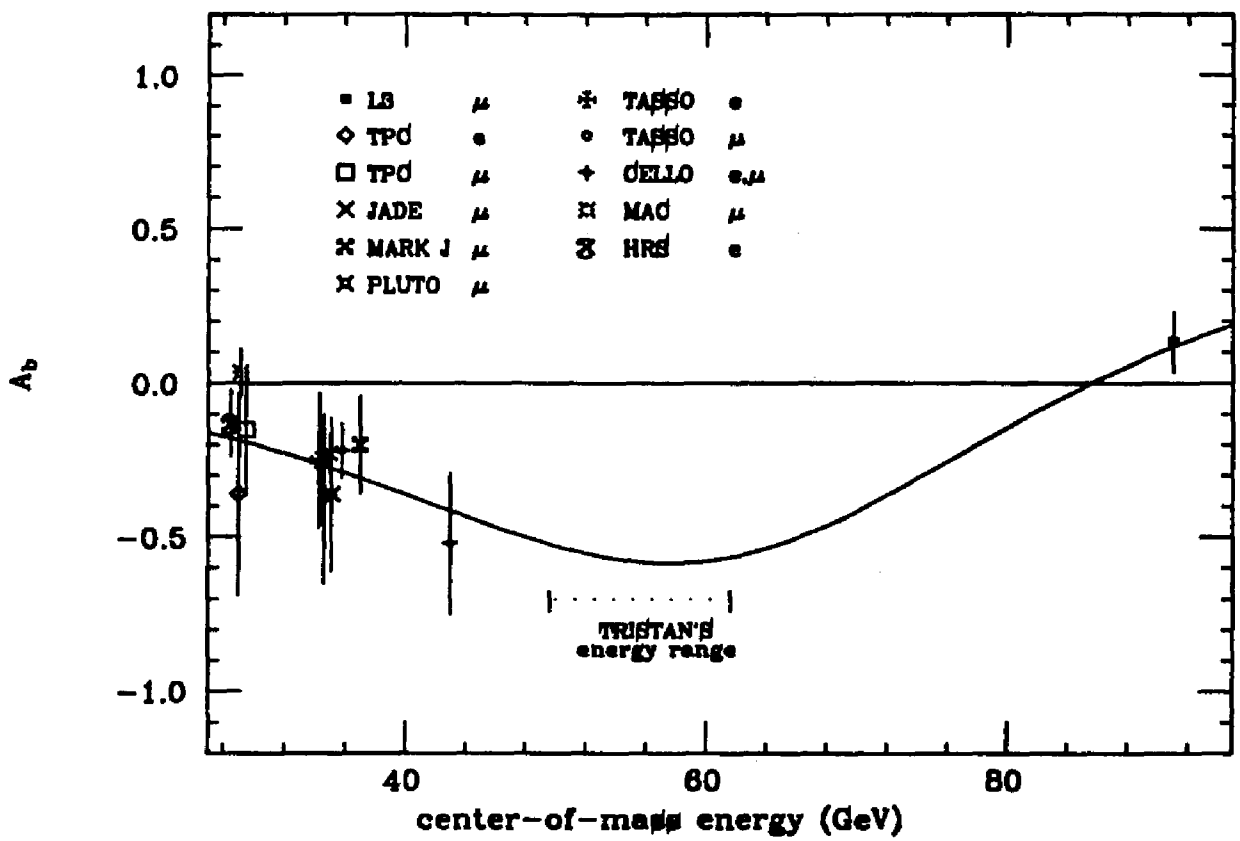

Figure 1.4: Forward-Backward asymmetry measurement for $e^+e^- \rightarrow b\bar{b}$ by previous experiments

weak isospin doublet since all the other observed quarks and leptons belong to left-handed doublets. Hence it is generally accepted that the t quark will eventually be found as higher energy accelerators become operational. Meanwhile, the absence of the t quarks in experimental searches has sustained interest in five quarks models. In the simplest alternative model without a t quark, the left- and right-handed b quarks are assigned to weak isospin singlets [2]. Such a model predicts A_b to be zero. The standard model prediction for A_b at a center-of-mass energy of 57.2 GeV is -0.58. Therefore the measurement of A_b is also a direct test of the viability of this alternative model.

The data were taken between 1987 and 1989 with an integrated luminosity of 33.3 pb^{-1}. This data sample contains 197 multi-hadronic inclusive muon events which were used for the measurement of A_b and R_b .

Chapter 2 gives a short description of the electroweak theory. Chapter 3 describes the TRISTAN e^+e^- accelerator and the AMY detector. Chapter 4 gives details of the selection of $e^+e^- \rightarrow b\bar{b}$ events. Chapter 5 describes the measurement of A_b and R_b . Chapter 6 talks about future measurements. Conclusions are drawn in chapter 7.

Chapter 2

Theory

The electroweak theory is based on the gauge group SU(2) $\times$ U(1) first proposed by S. Glashow [3] to account for the electromagnetic and weak interactions. S. Weinberg [4] and A. Salam [5] independently introduced the Higgs mechanism to generate mass for the gauge bosons, thereby making the gauge theory more realistic.

This chapter gives a brief description of the electromagnetic and weak interactions, their unification, derivation of the differential cross-section and prediction of the $e^+e^- \rightarrow b\bar{b}$ forward-backward charge asymmetry, A_b . $B^0 - \bar{B}^0$ mixing and topless models are also discussed.

2.1 Electromagnetic theory

Quantum electrodynamics (QED) is the quantum theory of the electromagnetic interaction and its basic formulation was completed by 1930. However, the calculation of higher order terms which involve divergences was not resolved until the late 1940's. The problem of divergences was solved by rescaling the fields so that all the divergences occur in the renormalization of the mass and charge of the electron. This means that the terms for the electron mass and charge were replaced by their experimentally measured values.

QED is a guage theory with the Lagrangian invariant under gauage transformations. A local gauge transformation is given by

$$\begin{aligned} \psi(x) &\rightarrow e^{i\alpha(x)}\psi(x) \\ \overline{\psi}(x) &\rightarrow e^{-i\alpha(x)}\overline{\psi}(x) \end{aligned} \tag{2.1}$$

The Lagrangian of a free particle

$$\mathcal{L}_1 = i\overline{\psi}\partial\psi - m\overline{\psi}\psi \tag{2.2}$$

is not locally gauge invariant since

$$\begin{aligned} \mathcal{L}_1 &\rightarrow ie^{-i(\alpha(x)}\overline{\psi}\gamma^\mu\partial_\mu(e^{i\alpha(x)}\psi(x)) - me^{i\alpha(x)}\overline{\psi}e^{i\alpha(x)}\psi \\ &= \mathcal{L}_1 - \overline{\psi}\gamma^\mu\psi\partial_\mu\alpha(x) = \mathcal{L}_1 - J^\mu\partial_\mu\alpha \end{aligned} \tag{2.3}$$

where J^μ is the conserved particle current. Additional terms are needed in order

to make the Lagrangian gauge invariant. Letting

$$\partial_\mu \rightarrow D_\mu = \partial_\mu + ieA_\mu(x) \tag{2.4}$$

$$A_\mu \rightarrow A_\mu - \frac{1}{e}\partial_\mu \alpha \tag{2.5}$$

where $A_\mu(x)$ is some vector field. The lagrangian when written as

$$\mathcal{L} = \mathcal{L}_1 - eJ^\mu A_\mu \tag{2.6}$$

is invariant under gauge transformation (2.1). The gauge field A_μ is identified with the electromagnetic potential and e with the electric charge.

QED is a theory that has been vigorously tested by measurements of Lamb shift, the hyperfine splitting in hydrogen, the magnetic moments of the electron, etc.

2.2 Weak Interaction

The weak interaction is responsible for such processes as the β-decay observed in radioactivity. The energy spectrum of the β rays (electrons) was bound to be continuous, violating the conservation of energy and momentum if it were a two body decay phenomenon. W. Pauli (1931) suggested that an unobserved massless particle must be emitted along with the β rays ($n \rightarrow pe^- +$ massless particle).

E. Fermi (1933) named the massless particle the "neutrino" and formulated a weak interaction theory of the form

$$\mathcal{M} = \frac{G}{\sqrt{2}} J^\mu J^\dagger_\mu \tag{2.7}$$

where $\mathcal{M}$ is the invariant amplitude and G is Fermi's constant. J^{μ} and $J^{\dagger}_{\mu}$ are the charged vector currents which describe the transitions involving a charge of one unit in the electric charge ($n \rightarrow p$, $\nu_e \rightarrow e^-$). Fermi theory is a four-fermion interaction that does not have a propagator term. The amplitude for β-decay is given by

$$\mathcal{M} = -\frac{4}{\sqrt{2}} G(\overline{p}\gamma^{\mu} n)(\overline{\nu}_e \gamma_{\mu} e) \tag{2.8}$$

Observations of the kaon decays

$$K \rightarrow 2\pi \ , 3\pi$$

led T.D. Lee and C.N. Yang (1956) to propose that the weak decay violates parity since these two final states have opposite parities. This was confirmed within months by C.S. Wu. Subsequent experiments showed that only left-handed neutrinos, ν_L, and right-handed anti-neutrinos, $\overline{\nu}_R$, participate in the weak interaction. If the ν_L and $\overline{\nu}_R$ are the only ones to exist, neutrinos must necessarily be massless since the scalar mass term is given by

$$\begin{aligned} m\psi\overline{\psi} &= m\overline{\psi}\left[\frac{1+\gamma^5}{2} + \frac{1-\gamma^5}{2}\right]\left[\frac{1+\gamma^5}{2} + \frac{1-\gamma^5}{2}\right]\psi \\ &= m\left(\overline{\psi}_R \psi_L + \overline{\psi}_L \psi_R\right) \end{aligned} \tag{2.9}$$

where γ^5 is the eigenvalue of chirality with $\gamma^5 = 1$ corresponding to right-handed and $\gamma^5 = -1$ to left-handed. The "elementary entities" of weak interactions are therefore massless and have definite chiralities. An eigen-state of finite mass is obtained by a superposition of the left- and right-handed states with equal weight (2.9). It is possible for electrons to have mass since left- and right-handed e^-'s exist

(figure 1.1) but neutrinos must be massless if ν_R does not exist. Charge conjugation is then also violated because a ν_L state is transformed by charge conjugation to a $\bar{\nu}_L$ state. Taking parity violation into consideration, the amplitude for β-decay is re-written as

$$\mathcal{M}(\mathrm{p} \rightarrow \mathrm{n e^{+} \nu_e}) = -\frac{1}{\sqrt{2}} \mathrm{G} \left[\bar{\mathrm{p}} \gamma^{\mu} (1-\gamma^5) \mathrm{n}\right] \left[\bar{\nu}_{\mathrm{e}} \gamma_{\mu} (1-\gamma^5) \mathrm{e}\right] \qquad (2.10)$$

Intermediate vector boson model

The Fermi theory violats unitarity (the requirement that probabilities add up to unity) in the high energy limit. A modification to correct this was first proposed by Hideki Yukawa (1935). This is the intermediate boson model that was improved upon by J. Schwinger (1957). The model introduces massive spin-1 charged bosons, W^+ and W^-, to mediate the weak interaction. This gives a β-decay amplitude of

$$\mathcal{M}(\mathrm{n} \rightarrow \mathrm{p e^{-}} \bar{\nu}_e) = \left(\frac{g}{\sqrt{2}} \bar{\mathrm{p}} \gamma^{\mu} \frac{1}{2} \left(1-\gamma^5\right) \mathrm{n}\right) \frac{1}{\mathrm{m_W^2} - \mathrm{q^2}} \left(\frac{g}{\sqrt{2}} \bar{\nu}_{\mathrm{e}} \gamma_{\mu} \frac{1}{2} \left(1-\gamma^5\right) \mathrm{e}\right) \qquad (2.11)$$

where $g/\sqrt{2}$ is a dimensionless weak coupling, and q the momentum carried by the weak boson, which has a mass of m_W. Comparison between (2.10) and (2.11) for low energies ($q^2 \ll m_W^2$) gives

$$\frac{\mathrm{G}}{\sqrt{2}} = \frac{\mathrm{g^2}}{8 \mathrm{m_W^2}} \qquad (2.12)$$

The fact that a weak decay is weak can now be explained by the large mass of the intermediate boson. However, at high energy, the amplitude for $e^+e^- \rightarrow W^+W^-$ diverges. This problem can be solved by introducing a neutral vector boson W^0 to cancel the divergence figure 2.1.

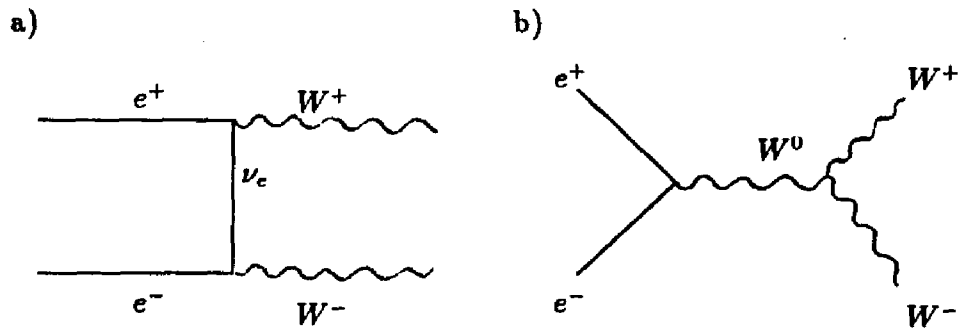

Figure 2.1: Feynman diagrams for $e^+e^- \rightarrow W^+W^-$

2.3 Electroweak Theory

S.L. Glashow (1961) proposed using an SU(2) × U(1) gauge group such that the necessary relations between the $W^{\pm}$ and W^0 couplings would emerge automatically. In doing so, he also unified the weak and electromagnetic interactions.

Quarks and leptons were assigned weak isospin and weak hypercharge internal symmetries. The left-handed components of the particles in each family form a doublet representation of the weak isospin group SU(2) and the right-handed components are SU(2) singlets (figure 1.1).

The generators of SU(2) symmetry obey the algebra

$$\left[T^i, T^j\right] = i\epsilon_{ijk}T^k. \tag{2.13}$$

The weak hypercharge denoted by Y has a U(1) symmetry and is defined such that

$$Q = T^3 + \frac{Y}{2} \tag{2.14}$$

where Q is the electric charge and T^3 the third component of the weak isospin.

The SU(2) gauge group has 3 generators and U(1) has 1 generator. So using SU(2) × U(1) introduces 4 gauge fields naturally, one for each group generator. The gauge fields for SU(2) are W_i^μ (i=1,2,3) and U(1) is B_0^μ. The electroweak interaction amplitude is then

$$\mathcal{M} = -ig\left(J^i\right)^\mu W_\mu^i - i\frac{g'}{2}\left(j^Y\right)^\mu B_\mu \tag{2.15}$$

The isotriplet vector field W_μ^i is coupled to the weak isospin current J_μ^i with strength g and a single vector field B_μ is coupled to the weak hypercharge j_μ^Y with strength $g'/2$. The fields

$$W_\mu^\pm = \frac{1}{\sqrt{2}}(W_\mu^1 \mp iW_\mu^2) \tag{2.16}$$

describe massive charged bosons $W^\pm$. W_μ^3 and B_μ are neutral fields.

The SU(2) × U(1) symmetry introduced by Glashow describes massless gauge bosons interacting with massless fermions. This cannot be used to describe the physical world since the gauge bosons are massive. Hence S. Weinberg (1967) and A. Salam (1968) were motivated to use the Higgs mechanism to generate guage boson and fermion masses without destroying the renormalizibility of the theory.

Spontaneous symmetry breaking

Consider the Lagrangian for a scalar particle

$$\mathcal{L} \;=\; T - V = \frac{1}{2}(\partial_\mu\phi)^2 - \left(\frac{1}{2}\mu^2\phi^2 + \frac{1}{4}\lambda\phi^4\right) \tag{2.17}$$

where $\lambda > 0$. For $\mu^2 < 0$, the potential has 2 minima satisfying

$$\frac{\partial V}{\partial\phi} = \phi(\mu^2 + \lambda\phi^2) = 0 \tag{2.18}$$

at $\phi = \pm v$ with $v = \sqrt{-\mu^2/\lambda}$. In order to use the perturbation theory, the expansion has to be made at one of the minima

$$\phi(x) = v + \eta(x) \tag{2.19}$$

where $\eta(x)$ represents the fluctuations around the minimun $\phi = v$. Expanding the Lagrangian around $\phi(x)$ gives

$$\mathcal{L}' = \frac{1}{2}(\partial_\mu \eta)^2 - \lambda v^2 \eta^3 - \frac{1}{4}\lambda \eta^4 + constant \tag{2.20}$$

with the "generation" of a mass term

$$\begin{aligned} -\frac{1}{2}m_\eta^2 &= -\lambda v^2 \\ m_\eta &= \sqrt{-2\mu^2} \end{aligned} \tag{2.21}$$

The physics is not changed by using $\mathcal{L}'$ instead of $\mathcal{L}$. This process of using the expansion of $\mathcal{L}'$ in η around the $\phi = v$ minimum to "generate" mass is referred to as "spontaneous symmetry breaking".

Higgs Mechanism

To generate mass for the $W^{\pm}$ and Z^0 bosons, the Higgs scalar is introduced. A lagrangian for the scalar fields is given by

$$\mathcal{L}_1 = \left| \left(\partial_\mu + ig\mathbf{T} \cdot \mathbf{W}_\mu + ig' \frac{Y}{2} B_\mu \right) \phi \right|^2 \tag{2.22}$$

The simplest choice of the Higgs scalar ϕ which is an SU(2) $\times$ U(1) multiplet is

$$\phi = \begin{pmatrix} \phi^+ \\ \phi^0 \end{pmatrix} \tag{2.23}$$

where

$$\phi^+ = \frac{1}{\sqrt{2}}(\phi_1 + i\phi_2)$$
$$\phi^0 = \frac{1}{\sqrt{2}}(\phi_3 + i\phi_4) \tag{2.24}$$

and ϕ_i are real.

The Lagrangian can also contain a self-interaction term between the Higgs fields

$$\mathcal{L}_2 = -V(\phi) \tag{2.25}$$

where

$$V(\phi) = \mu^2(\phi^\dagger\phi) + \lambda(\phi^\dagger\phi)^2 \tag{2.26}$$

with $\lambda > 0$. For $\mu^2 < 0$, the potential $V(\phi)$ has its minimum at a finite value of

$$\phi^\dagger\phi = \frac{1}{2}(\phi_1^2 + \phi_2^2 + \phi_3^2 + \phi_4^2) = -\frac{\mu^2}{2\lambda} \tag{2.27}$$

ϕ_i can be chosen such that

$$\begin{aligned} \phi_1 &= \phi_2 = \phi_4 = 0 \\ \phi_3 &= \sqrt{-\frac{\mu^2}{\lambda}} = v. \end{aligned} \tag{2.28}$$

$\phi(x)$ is then expanded about

$$\phi_0 = \frac{1}{\sqrt{2}}\begin{pmatrix} 0 \\ v \end{pmatrix} \tag{2.29}$$

Due to gauge invariance, the expansion

$$\phi(x) = \frac{1}{\sqrt{2}}\begin{pmatrix} 0 \\ v + h(x) \end{pmatrix} \tag{2.30}$$

can be substituted into the lagrangian $\mathcal{L} = \mathcal{L}_1 + \mathcal{L}_2$. The relevant terms are [6]

$$|(-ig\frac{\tau}{2}\cdot W_\mu - i\frac{g'}{2}B_\mu)\phi|^2$$

$$= (\frac{1}{2}vg)^2 W_\mu^+ W^{-\mu} + \frac{1}{8}v^2 \begin{pmatrix} W_\mu^3 & B_\mu \end{pmatrix} \begin{pmatrix} g^2 & -gg' \\ -gg' & g'^2 \end{pmatrix} \begin{pmatrix} W^{3\mu} \\ B^\mu \end{pmatrix} \quad (2.31)$$

where

$$W^\pm = \frac{1}{\sqrt{2}}(W^1 \mp iW^2) \quad (2.32)$$

The first term (2.31) is the mass term for the charged bosons $W^\pm$

$$M_W = \frac{1}{2}vg \quad (2.33)$$

The term which is off-diagonal in the W_μ^3 and B_μ basis is

$$\frac{1}{8}v^2[g^2(W_\mu^3)^2 - 2gg'W_\mu^3 B^\mu + g'^2 B_\mu] = \frac{1}{8}v^2[gW_\mu^3 - g'B_\mu]^2 + 0[g'W_\mu^3 + gB_\mu]^2 \quad (2.34)$$

Rotating to fields given by

$$\begin{aligned} A_\mu &= \frac{g'W_\mu^3 + gB_\mu}{\sqrt{g^2+g'^2}} \\ Z_\mu &= \frac{gW_\mu^3 - g'B_\mu}{\sqrt{g^2+g'^2}} \end{aligned} \quad (2.35)$$

leads to mass terms

$$\begin{aligned} M_A &= 0 \\ M_Z &= \frac{1}{2}v\sqrt{g^2+g'^2}. \end{aligned} \quad (2.36)$$

The masses of the $W^\pm$ and Z^0 bosons are related by

$$\frac{M_W}{M_Z} = \frac{g}{g^2+g'^2} = \cos\theta_W \quad (2.37)$$

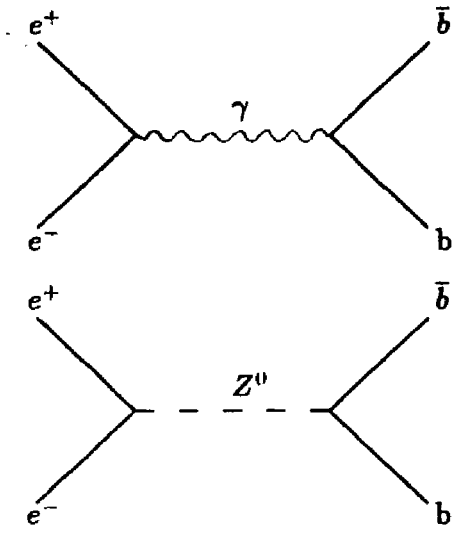

Figure 2.2: Feynmann diagrams for $e^+e^- \rightarrow b\bar{b}$

where θ_W is Weinberg angle, measured experimentally to be $\sin^2\theta_W \sim 0.23$ [7]. A_μ is identified with the electromagnetic potential.

2.4 Differential cross section

The differential cross-section for $e^+e^- \rightarrow b\bar{b}$ is given by

$$\frac{d\sigma}{d\cos\theta} = \frac{1}{32\pi s}|\mathcal{M}_\gamma + \mathcal{M}_Z|^2 \tag{2.38}$$

The invariant amplitudes $\mathcal{M}_\gamma$ and $\mathcal{M}_Z$ correspond to the Feynman diagrams in figure 2.2.

$$\mathcal{M}_\gamma = -\frac{eQ_b}{q^2}\left(\bar{b}\gamma^\beta b\right)\left(\bar{e}\gamma_\beta e\right) \tag{2.39}$$

$$\mathcal{M}_Z = -\frac{3g^2}{4\cos^2\theta_W}\left[\bar{b}\gamma^\nu\left(g_V^b - g_A^b\gamma^5\right)b\right]\left(\frac{g_{\beta\lambda} - q_\beta q_\lambda/M_{Z^0}^2}{q^2 - M_{Z^0}^2 + iM_{Z^0}\Gamma_Z}\right)\left[\bar{e}\gamma^\lambda\left(g_V^e - g_A^e\gamma^5\right)e\right] \tag{2.40}$$

The invariant amplitudes $\mathcal{M}_Z$ and $\mathcal{M}_\gamma$ can also be expanded in terms of right- and left-handed spinors since $\frac{1}{2}(1 \pm \gamma^5)$ are projection operators.

$$\mathcal{M}_Z = -\frac{3g^2}{4\cos^2\theta_W(s - M_{Z^0}^2 + i\Gamma_Z)}\left[g_R^b\left(\bar{b}_R\gamma^\beta b_R\right) + g_L^b\left(\bar{b}_L\gamma^\beta b_L\right)\right] \times$$
$$\left[g_R^e\left(\bar{e}_R\gamma_\beta e_R\right) + g_L^e\left(\bar{e}_L\gamma_\beta e_L\right)\right] \tag{2.41}$$

$$\mathcal{M}_\gamma = -\frac{eQ_b}{q^2}\left[\left(\bar{b}_R\gamma^\beta b_R\right) + \left(\bar{b}_L\gamma^\beta b_L\right)\right]\left[\left(\bar{e}_R\gamma_\beta e_R\right) + \left(\bar{e}_L\gamma_\beta e_L\right)\right] \tag{2.42}$$

where $g_R = g_V - g_A$, $g_L = g_V + g_A$ and

$g_V - g_A\gamma^5 = (g_V - g_A)\frac{1}{2}(1 + \gamma^5) + (g_V + g_A)\frac{1}{2}(1 - \gamma^5)$. Hence the differential cross sections for definite helicities are

$$\frac{d\sigma}{d\cos\theta}(e_L^- e_R^+ \to b_L\bar{b}_R) = \frac{3\pi\alpha^2}{2s}(1 + \cos\theta)^2\left|Q_b + 4\chi g_L^b\right|^2 \tag{2.43}$$

$$\frac{d\sigma}{d\cos\theta}(e_L^- e_R^+ \to b_R\bar{b}_L) = \frac{3\pi\alpha^2}{2s}(1 - \cos\theta)^2\left|Q_b + 4\chi g_L^b\right|^2 \tag{2.44}$$

$$\frac{d\sigma}{d\cos\theta}(e_R^- e_L^+ \to b_R\bar{b}_L) = \frac{3\pi\alpha^2}{2s}(1 + \cos\theta)^2\left|Q_b + 4\chi g_L^b\right|^2 \tag{2.45}$$

$$\frac{d\sigma}{d\cos\theta}(e_R^- e_L^+ \to b_L\bar{b}_R) = \frac{3\pi\alpha^2}{2s}(1 - \cos\theta)^2\left|Q_b + 4\chi g_L^b\right|^2 \tag{2.46}$$

where χ is a function of s

$$\chi(s) = \frac{1}{16\cos^2\theta_W\sin^2\theta_W}\left[\frac{s}{s - M_{Z^0}^2 + i\Gamma_Z}\right]. \tag{2.47}$$

The average over the four allowed L and R helicities combinations then gives

$$\frac{d\sigma}{d\cos\theta} = \frac{\pi\alpha^2}{2s}\left[R(1 + \cos^2\theta) + A\cos\theta\right] \tag{2.48}$$

with

$$\begin{aligned} \mathrm{R} &= 3\{Q_b^2 - 8Q_b g_V^e g_V^b \mathrm{Re}(\chi) + \\ &\quad 16[(g_V^e)^2 + (g_A^e)^2][(g_V^b)^2 + (g_A^b)^2]|\chi|^2\} \qquad (2.49) \\ A &= 8[-6Q_b g_A^e g_A^b \mathrm{Re}(\chi) + 48 g_V^e g_V^b g_A^e g_A^b |\chi|^2]. \qquad (2.50) \end{aligned}$$

Integrating (2.48) over dcosθ gives,

$$\sigma(\mathrm{e^+e^-} \rightarrow \mathrm{b\bar{b}}) = (\frac{4\pi\alpha^2}{3\mathrm{s}})\mathrm{R} = \sigma_0 \mathrm{R} \qquad (2.51)$$

where σ_0 is the lowest order QED cross section. R is then identified as $\mathrm{R_b}$.

The forward-backward charge asymmetry, $\mathrm{A_b}$ is defined as

$$\mathrm{A_b} = \frac{\sigma_\mathrm{F} - \sigma_\mathrm{B}}{\sigma_\mathrm{F} + \sigma_\mathrm{B}} \qquad (2.52)$$

where σ_F and σ_B are the forward and backward cross-section respectively and are defined as

$$\begin{aligned} \sigma_\mathrm{F} &= \int_{\theta=0}^{\theta=\pi/2} \frac{\mathrm{d}\sigma}{\mathrm{dcos}\theta} \mathrm{dcos}\theta \\ \sigma_B &= \int_{\theta=\pi/2}^{\theta=\pi} \frac{d\sigma}{dcos\theta} dcos\theta \qquad (2.53) \end{aligned}$$

Substituting σ_F and σ_B into (2.58) gives

$$\begin{aligned} \mathrm{A_b} &= \frac{3}{8}\frac{\mathrm{A}}{\mathrm{R_b}} \\ &= 3\left[-6Q_b g_A^e g_A^b \mathrm{Re}(\chi) + 48 g_V^e g_V^b g_A^e g_A^b |\chi|^2\right]/\mathrm{R_b}. \qquad (2.54) \end{aligned}$$

The differential cross-section for $\mathrm{e^+e^-} \rightarrow \mathrm{b\bar{b}}$ then becomes

$$\frac{\mathrm{d}\sigma}{\mathrm{dcos}\theta} = \frac{\pi\alpha^2}{2\mathrm{s}}\mathrm{R_b}\left[(1+\cos^2\theta) + \frac{8}{3}\mathrm{A_b}\cos\theta\right]. \qquad (2.55)$$

f	Q_f	g_A^f	g_V^f
$\nu_e, \nu_\mu, \ldots$	0	$\frac{1}{2}$	$\frac{1}{2}$
$e^-, \mu^-, \ldots$	-1	$-\frac{1}{2}$	$-\frac{1}{2} + 2\sin^2\theta_W \sim -0.03$
u,c,t,...	$\frac{2}{3}$	$\frac{1}{2}$	$\frac{1}{2} - \frac{4}{3}\sin^2\theta_W \sim 0.19$
d,s,b,...	$-\frac{1}{3}$	$-\frac{1}{2}$	$-\frac{1}{2} + \frac{2}{3}\sin^2\theta_W \sim -0.34$

Table 2.1: The $Z^0 \rightarrow f\bar{f}$ vertex factors in the standard model with $\sin^2\theta_W = 0.234$.

The $Z^0 \rightarrow f\bar{f}$ vertex factors for the standard model are shown in table 2.1. The weak isospin and hypercharge quantum numbers are shown in table 2.2.

R_b is modified by QCD terms corresponding to a contribution from gluons (figure 2.3). The result in (2.49) is then increased [8] by a factor of

$$\left[1 + \frac{\alpha_s(s)}{\pi} + C_2\left(\frac{\alpha_s(s)}{\pi}\right)^2\right] \tag{2.56}$$

$\alpha_s(s)$ is the "running" strong coupling constant, which is given by [9]

$$\alpha_s(s) = \frac{12}{(33 - 12N_f)\ln(s/\Lambda^2)} \times \left\{1 - 6\frac{153 - 19N_f\ln[\ln(s/\Lambda^2)]}{(33 - 2N_f)^2\ln(s/\Lambda^2)}\right\} \tag{2.57}$$

where Λ is the QCD scale parameter and N_f is the number of available flavors at the center of mass energy $\sqrt{s}$. The constant C_2 is given by $C_2 = 1.986 - 0.115N_f$ [10]. $N_f = 5$ for TRISTAN's energy range and the effect of this QCD correction is to increase R_b by about 5%.

Substituting for the variables in (2.49) and in the QCD correction (2.56) gives the standard model prediction for A_b and R_b at $\sqrt{s} = 57.2$ GeV as -0.58 and 0.56

Lepton	T	T^3	Q	Y	Quark	T	T^3	Q	Y
$\nu_e, \nu_\mu, \nu_\tau, \ldots$	$\frac{1}{2}$	$\frac{1}{2}$	0	-1	$u_L, c_L, t_L, \ldots$	$\frac{1}{2}$	$\frac{1}{2}$	$\frac{2}{3}$	$\frac{1}{3}$
$e_L^-, \mu_L^-, \tau_L^-, \ldots$	$\frac{1}{2}$	$-\frac{1}{2}$	-1	-1	$d_L, s_L, b_L, \ldots$	$\frac{1}{2}$	$-\frac{1}{2}$	$-\frac{1}{3}$	$\frac{1}{3}$
					$u_R, c_R, t_R, \ldots$	0	0	$\frac{2}{3}$	$\frac{4}{3}$
$e_R^-, \mu_R^-, \tau_R^-, \ldots$	0	0	-1	-2	$d_R, s_R, b_R, \ldots$	0	0	$-\frac{1}{3}$	$-\frac{2}{3}$

Table 2.2: Weak isospin and hypercharge quantum numbers of leptons and quarks in standard model

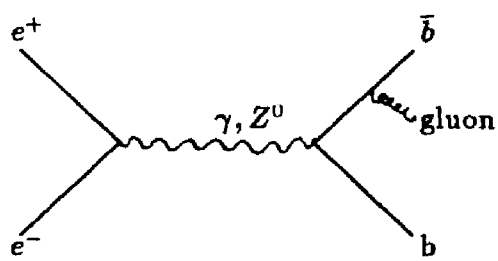

Figure 2.3: QCD correction to $e^+e^- \rightarrow b\bar{b}$

respectively. Here $M_Z = 91$ GeV and $\Gamma_Z = 2.5$ GeV.

2.5 Topless Model

The simplest model without a top quark has the left- and right-handed b quarks assigned to singlets. Such an assignment for the b quarks is allowed in the SU(2) $\times$ U(1) model. A direct consequence of this is that g_A^b becomes zero. Substituting this into (2.49) and (2.54) gives $A_b = 0$ and $R_b = 0.38$. This can be checked experimentally by the present analysis. Another distinctive feature of this model is that the flavor changing neutral current decay modes [11], $B \rightarrow X l^+ l^-$ where $l^\pm = e^\pm$ or $\mu^\pm$, are predicted to have branching ratios of 2%. This is above the experimental upper bound of 1.3% at 90% confidence level set by the CLEO collaboration [12].

A more sophisticated topless model was proposed by Ernest Ma [13] using Superstring theory. This model uses as its gauge group $SU(3) \times SU(2)_1 \times SU(2)_2 \times U(1)$ subgroup of E_6. The usual doublet assignment is given to $(u,d)_L$ and $(c,s)_L$ under $SU(2)_1$. A new doublet is assigned to $(c,b)_R$ under $SU(2)_2$. b_L is assigned a singlet under both $SU(2)_1$ and $SU(2)_2$. b_R is a singlet under $SU(2)_1$. There is no need for a top quark in this model. The flavor changing neutral current modes are greatly reduced by this enlarged model [14] and the decay mode $B \rightarrow X l^+ l^-$ is consistent with experimental upper limit. The axial-vector coupling g_A^b is zero in this model. The observed forward-backward charge asymmetry in $e^+e^- \rightarrow b\bar{b}$ is explained by introducing a new neutral scalar boson ϕ and a new heavy charged lepton E. These

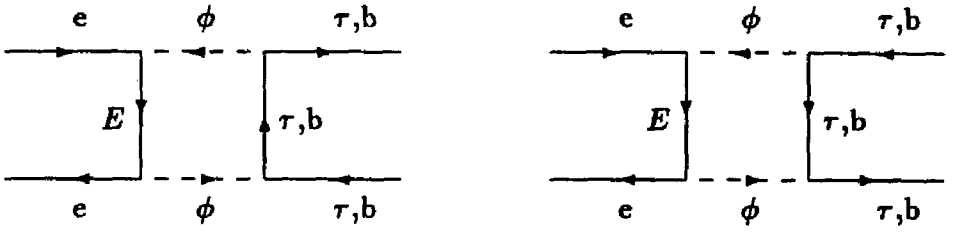

Figure 2.4: One loop amplitudes contributing to $e^+e^- \rightarrow b\bar{b}$

new particles contribute to $e^+e^- \rightarrow b\bar{b}$ as shown in figure 2.4.

The asymmetry A_b is given by [15]

$$A_b = \left(\frac{g_1^2}{4\pi}\right)\left(\frac{g_3^2}{4\pi}\right)\left(\frac{\sqrt{2}}{8m^2 G_F}\right)\left(1-\frac{s}{M_Z^2}\right)\left(1+\frac{1}{9}\left(\frac{s}{4m^2}\right)+\frac{7}{135}\left(\frac{s}{4m^2}\right)^2\right) \quad (2.58)$$

where g_1, g_2 and g_3 are Yukawa couplings and $m_E = m_\phi = m$. s is the square of the center-of-mass energy and G_F is the Fermi constant. The phenomelogical requirement is for

$$\left(\frac{g_1^2}{4\pi}\right)\left(\frac{g_3^2}{4\pi}\right)\frac{1}{m^2} \sim \frac{8G_F}{\sqrt{2}} \quad (2.59)$$

The masses of ϕ and E are expected to be much less than 100 GeV, otherwise the Yukawa couplings g_1, g_2 and g_3 would have to be very big to be consistent with (2.59). A search for ϕ and E were made at TRISTAN [16] but they were not found.

The charge asymmetry, A_b, for this Superstring model can still agree with the data depending on the as yet undetermined parameters in (2.57).

2.6 $B^0 - \overline{B}^0$ mixing and its effect on A_b

The neutral B^0 mesons are made from charge-conjugate quark-antiquark pairs (B_d^0 ($\bar{b}d$), $\overline{B}_d^0$ ($b\bar{d}$), B_s^0 ($\bar{b}s$), $\overline{B}_s^0$ ($b\bar{s}$)). So flavor-changing neutral current weak interactions can mix these states. The box diagrams for $B^0 - \overline{B}^0$ mixing are shown in figure 2.5. The eigenstates are

$$\begin{aligned} B_1 &= \frac{1}{\sqrt{2}}\left[< B_d^0 > + < \overline{B}_d^0 >\right] \quad \text{and} \\ B_2 &= \frac{1}{\sqrt{2}}\left[< B_d^0 > - < \overline{B}_d^0 >\right]. \end{aligned} \tag{2.60}$$

The mass difference between these two eigenstates is ΔM. For simplicity, the lifetime and total decay width Γ of B_1 and B_2 are assumed to be equal. Then, for a system which is entirely B^0 at time zero, $I_B(0) = 1$, the intensity $I_{\overline{B}}(t)$ to find it in a $\overline{B}^0$ state at time t is

$$I_{\overline{B}}(t) = \frac{1}{2}e^{-\Gamma t}(1 - \cos\Delta M t) \tag{2.61}$$

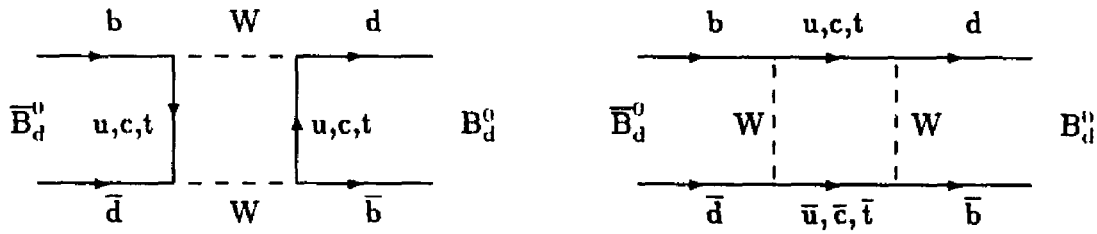

Figure 2.5: Box diagrams contributing to $B_d^0 - \overline{B}_d^0$ mixing

A mixing parameter is defined by $x = \Delta M/\Gamma$. Appreciable mixing only occurs for large x. The integrated transition probabilities are given by the mixing parameter r.

$$r_d = \frac{\Gamma(B_d^0 \to \overline{B}_d^0)}{\Gamma(B_d^0 \to B_d^0)} = \frac{x^2}{2+x^2} \tag{2.62}$$

where $0 \leq r < 1$. Frequently the parameter χ is used instead of r where

$$\chi_d = \frac{\Gamma(B_d^0 \to \overline{B}_d^0)}{\Gamma(B_d^0 \to B_d^0) + \Gamma(B_d^0 \to \overline{B}_d^0)} = \frac{r_d}{1+r_d} \tag{2.63}$$

where $0 \leq \chi_d < 0.5$. The standard model predicts [17] $r_d \sim 0.02 - 0.05$ and $r_s \sim 0.12 - 0.75$ (r_s is for $B_s^0 - \overline{B}_s^0$ mixing).

Effect of $B^0 - \overline{B}^0$ mixing on A_b

The ratio of production of $B_u^+ : B_d^0 : B_s^0$ is expected to be about 3:3:1 in e^+e^- annihilation at TRISTAN energies. This is deduced from the 3:3:1 ratio for the production of quark pair ($u\bar{u} : d\bar{d} : s\bar{s}$) from color fields. The $B^0 - \overline{B}^0$ mixing parameter χ is defined by

$$\chi_d = \frac{\Gamma(B_d^0 \to \overline{B}_d^0 \to \overline{X})}{\Gamma(B_d^0 \to X \text{ or } \overline{X})}.$$

The average χ is then

$$\chi = \frac{3}{7}\chi_d + \frac{1}{7}\chi_s \tag{2.64}$$

Charge conservation demands that there is no mixing for charged mesons. The range of possible values for χ_d and χ_s is from 0 to 0.5. The best measurement of χ_d are given by CLEO [18] ($\chi_d = 0.123 \pm 0.048$) and ARGUS [19] ($\chi_d = 0.167 \pm 0.055 \pm 0.046$).

In the presence of $B^0 - \overline{B}^0$ mixing a μ^- is sometimes produced from an initial $\overline{b}$-quark, thereby confusing the quark identification. Consequently the observed numbers of forward and backward events become

$$N_F^{obs} = N_F - \chi N_F + \chi N_B$$

$$N_B^{obs} = N_B - \chi N_B + \chi N_F$$

and the observed asymmetry is

$$A_b^{obs} = \frac{N_F^{obs} - N_B^{obs}}{N_F^{obs} + N_B^{obs}} = (1 - 2\chi)A_b. \tag{2.65}$$

If one varies χ_s from 0.0 to 0.5 and varies χ_d within errors given by the ARGUS and CLEO results ($0.075 \leq \chi_d \leq 0.239$), the effect of $B^0 - \overline{B}^0$ mixing is to reduce the magnitude of the observed asymmetry by 6% to 36%. Conversely, by measuring A_b^{obs} and using the standard model predicted value of A_b, one can measure or set a limit on χ.

Chapter 3

The AMY Experiment

The AMY [20] experiment is a collaboration of physicists from five countries; the USA, Japan, the People's Republic of China, Korea and from 1989 the Phillipines (see appendix A for list of collaborators). AMY is one of four collaborations at TRISTAN (Transposable Ring Intersecting STorage Accelerator in Nippon) which is an e^+e^- collider located at KEK (Kou Enerugii Butsuri-gaku Kenkyuu-jyo or National Laboratory for High Energy Physics) in Tsukuba City, Japan. The other three collaborations at TRISTAN are the VENUS and TOPAZ general purpose e^+e^- experiments and the specialized SHIP detector. This chapter gives a brief description of TRISTAN and the AMY experiment.

3.1 The TRISTAN e^+e^- collider

TRISTAN [21] consists of a positron generator, an electron linear accelerator (LINAC), an accumulation ring (AR) and a main ring (MR). Figure 3.1 shows the site layout of TRISTAN.

Positrons are generated by e^+e^- pair creation processes when a 200 MeV, 10 ampere, electron beam strikes Tantalum. The positrons are collected and accelerated to 250 MeV, then transferred to the LINAC.

The 400 m long LINAC accelerates the electrons and positrons to 2.5 GeV where they are injected into the AR. The AR has a circumference of 377 m. It accumulates the electrons and positrons and when currents of about 10 mA of electrons and positrons are accumulated, the AR accelerates them to 8 GeV and feeds them into the MR; first the positrons then the electrons.

The MR is buried 11m underground and has a circumference of 3 km. It consists of 4 straight sections of 200 m each and four curved sections of 550 m each. The center of each straight section is where the beams are made to collide. The AMY detector is built around one such collision point in the OHO experimental hall. The three other experiments, VENUS, TOPAZ and SHIP, occupy the FUJI, TSUKUBA and NIKKO experimental halls respectively.

In the MR, electrons and positrons are grouped into two bunches. A typical bunch size is about 2.3 mm along the x axis, 0.023 mm along the y axis and 1.17 mm along the z axis. The z direction at the AMY detector is defined as the direction of

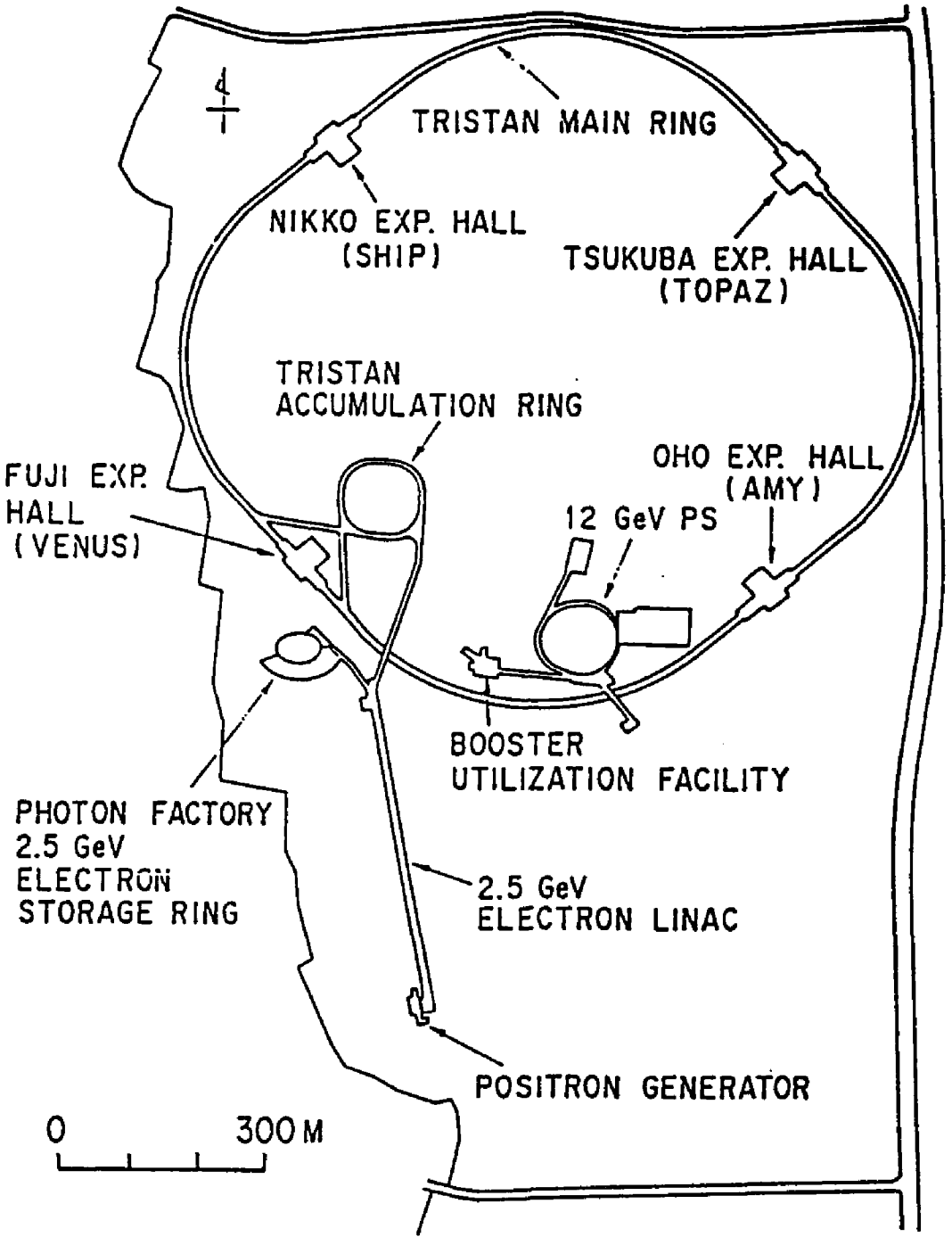

Figure 3.1: The site layout of TRISTAN

the e^- beam and the y direction is perpendicularly upward. Beam crossings occur once every 5.0 μs and the beam energy spread is $\sigma_E/E = 1.64 \times 10^{-3}$ (r.m.s.). This rather large beam spread is due to the small bending radius at the curved sections.

The first electron-positron collision occured on November 14, 1986 at a center of mass energy of 50.0 GeV. Since then a center of mass energy of 61.4 GeV has been achieved and an integrated luminosity of 33.3 pb^{-1} was accumulated by July 1989.

3.2 The AMY Detector

Electron-Positron annihilation at high center of mass energies results in the production of many particles which are either charged or neutral. These particles move away from the interaction point in all directions. The short-lived ones quickly decay into more stable particles within a few millimeters.

AMY is a general purpose particle detector that tracks and measures the energy and momenta of the particles emerging from the interaction point. Figure 3.2 shows the isometric and cross-sectional views of the AMY detector which is optimized for lepton identification. It is an extremely compact detector (about 120 m^3 compared with 600 m^3 for VENUS.) The z direction at the AMY detector is defined as the direction of the e^- beam and the y direction is perpendicularly upward. The r, ϕ and θ coordinates are define for the cylindrical coordinate system.

The tracking of the charge particles in the barrel region is done by the central

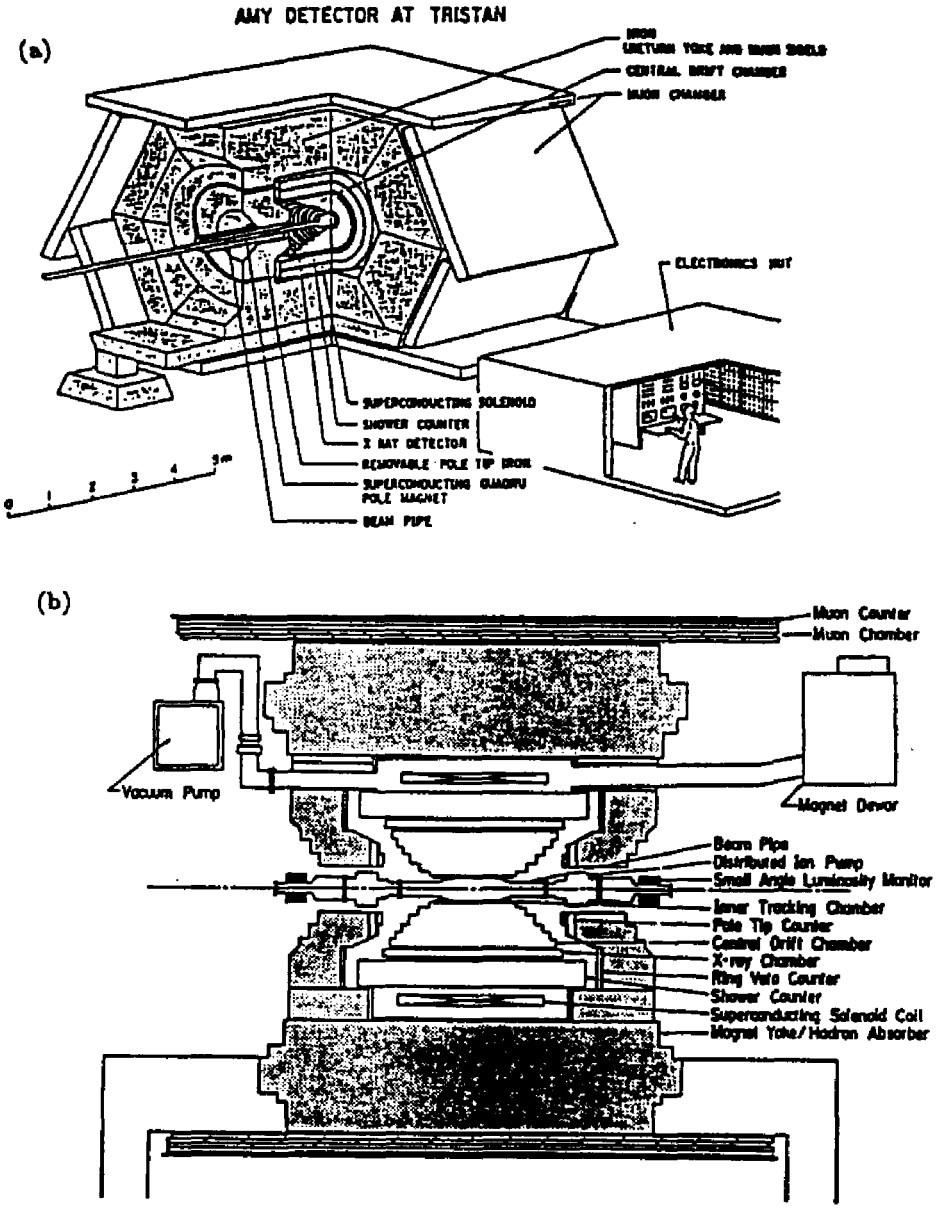

Figure 3.2: (a) The isometric and (b) cross-sectional views of AMY

drift chamber (CDC) and the charge particle momenta are calculated from the deflection in the 3 Tesla magnetic field produced by the superconducting magnet. The electromagnetic shower counter (SHC) provides energy measurement for gammas and electrons, and also identifies the electrons.

The measurement of A_b described in this thesis depends on the detection and identification of muons. This is done by the muon identification system (MUO) comprising the thick hadron absorber, muon chambers and counters.

The following sections give a brief description of the various components of AMY and its principle of operation.

3.2.1 Inner Tracking Chamber (ITC)

The ITC is a drift chamber located just outside the beam pipe, which detects charged particles after they have traversed only 1.7% radiation lengths of material. The ITC is designed to determine the vertices of charge tracks and also to help provide an efficient trigger for events of interest while minimizing triggers on background. The ITC consists of four layers of cylindrical plastic tubes. The innermost and outermost layers are 12.2 cm and 14.2 cm from the beam axis (z-axis) respectively. Each of the tubes is 55 cm long with a radius of 3mm and is aligned parallel to the beam axis. At the center of each tube is a 16μm diameter anode wire stretched the length of the tube. A voltage of +1700 is applied to the anode wire. The inside surface of the tube is coated with aluminium to provide the cathode.

When a charge particle passes through the gas in a drift chamber, it liberates electrons by ionisation. The electrons drift towards the anode wire and the position of the ionisation is calculated from the time it takes for the electrons to drift to the anode wire. Position measurement in the ITC is therefore achieved in the plane perpendicular to the beam axis ($r - \phi$) and has a spatial resolution of $\sigma \sim 80\mu m$. The staggered arrangement of the layers makes it possible to determine whether a charged particle passes by the right or left of a hit wire. This is commonly called the resolution of left-right ambiguity. The ITC is filled with 50% Ar and 50% C_2H_6 and the gas is pressurized to 1.48 kg/cm^2.

The signals are read by time-to-analog converters (TAC) and analog to digital converters (ADC). TAC signals are used to determine the hit position and ADC signals are used for rejecting noise signals in the TAC. A cross-sectional view of the ITC is shown in figure 3.3.

3.2.2 Central Drift Chamber (CDC)

The CDC is the main component of the AMY detector for tracking charged particles. Figure 3.4 shows a schematic diagram of the CDC. The CDC consists of 40 cylinders of wires forming six bands. It is outside the ITC radially and extends to a radius of 65 cm. The length of the bands increase radially outwards to maintain an angular coverage of $|\cos\theta| < 0.87$. There are 9,106 sense wires and 22,966 field wires. Each sense wire is in the middle of a cell surrounded by six field wires in a

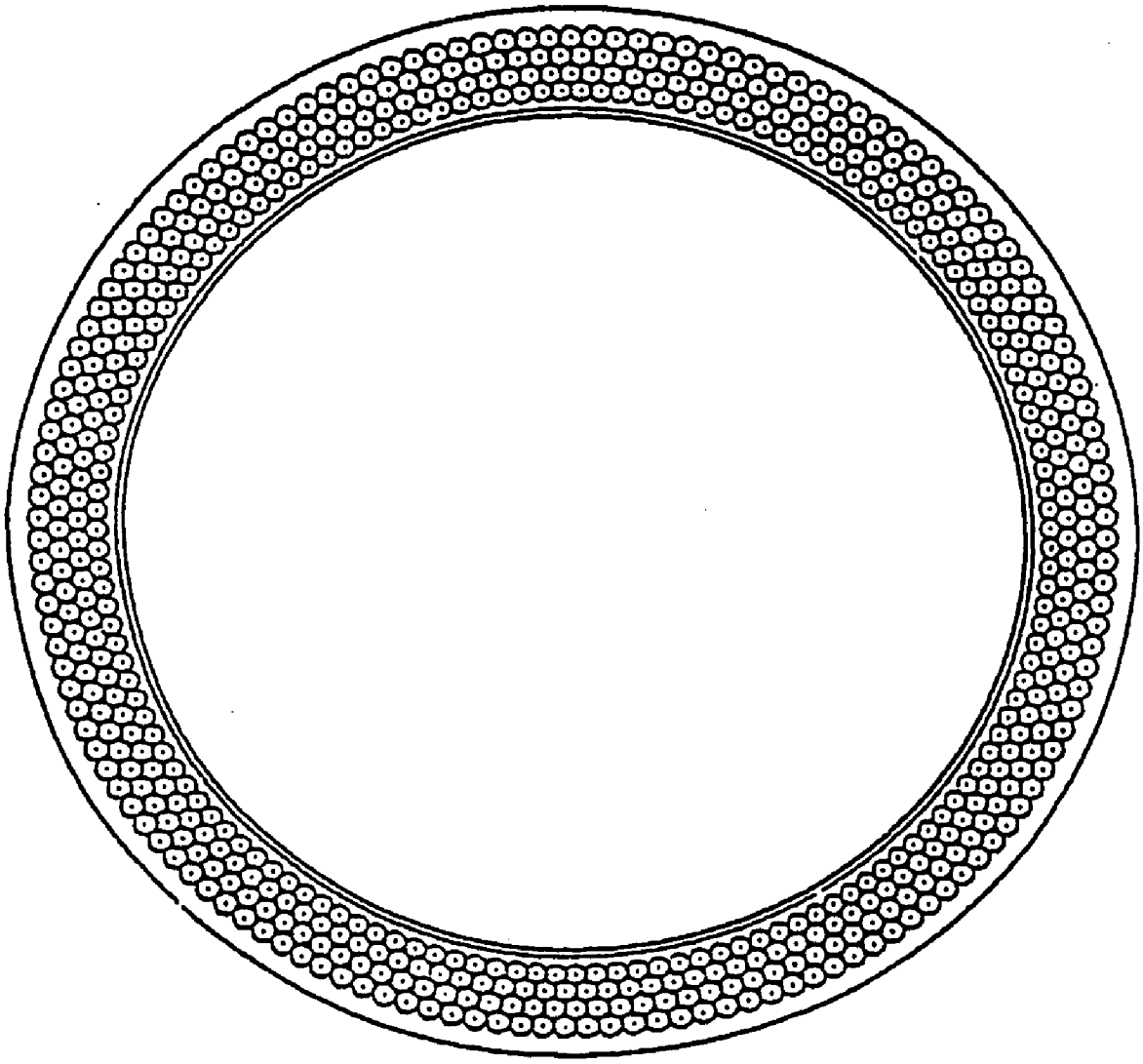

Figure 3.3: Cross-sectional view of ITC

hexagonal arrangement. The advantage of the hexagonal arrangement is that the contours of equal drift time around a sense wire are concentric circles even in a magnetic field as shown in figure 3.5. The sense wires are made of gold plated tungsten with a radius of 10 μm and the field wires are made of gold plated aluminium with a radius of 80 μm. There are two kinds of sense wires; axial and stereo. The axial wires are arranged parallel to the beam axis and they track the hit positions in the r-ϕ plane. The stereo wires are strung at an angle of 4° to the axial wires, enabling the tracking of charged particles trajectories in the z direction. Altogether there are 25 cylinders of axial and 15 cylinders of stereo wires in the CDC. The CDC was filled with HRS gas (89% Ar, 10% CO_2 and 1% CH_4) at atmospheric pressure. The gas was changed to neon/ethane (50%:50%) after the installation of the x-ray detector in May 1989. (All data accumulated after run 6899 were taken with the neon/ethane mixture. This includes some of the 60 GeV data, and all of 60.8 and 61.4 GeV data.) Neon absorbs fewer of the synchrotron x-rays than argon due to its smaller atomic mass number. The switch to neon/ethane was therefore made to increase the effeciency of the X-ray detector. The 50%:50% mixure of neon/ethane is chosen so that the drift velocity and gas gain characteristics are similar to those for HRS.

Charged particles follow a helical path in the presence of the 3 Tesla magnetic field. The CDC track finding software reconstructs the trajectory of a charged particle by grouping the hit positions in the CDC. The momentum and charge of

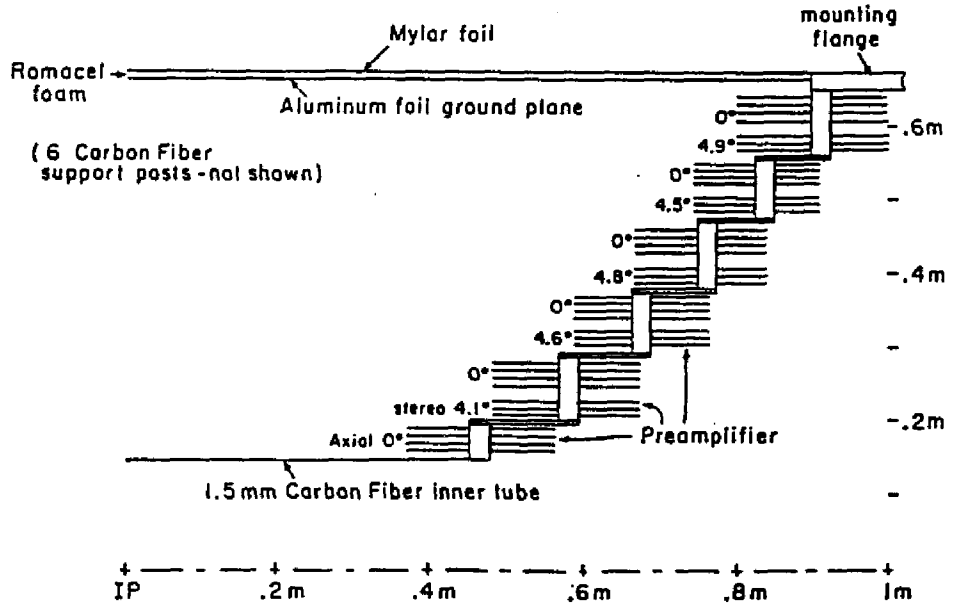

Figure 3.4: Schematic Diagram of CDC

(a) B = 0 Tesla (10 nsec drift time contours)

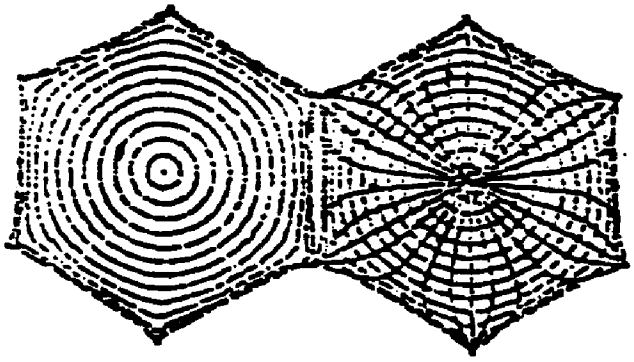

(b) B = 3 Tesla (10 nsec drift time contours)

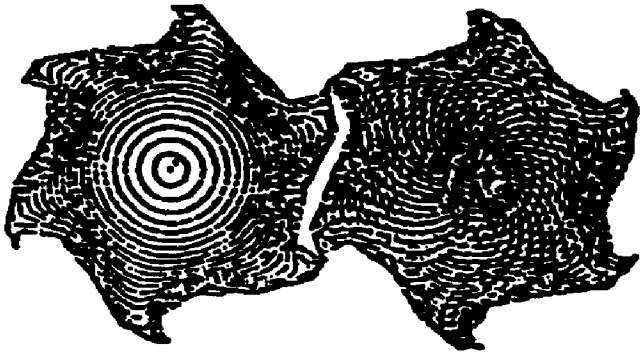

Figure 3.5: Countours of equal drift time for CDC

these particles are determined from the curvature of the reconstructed trajectory in the r-ϕ plane. The tranverse momentum is given by

$$p_t = 0.29979qBR \tag{3.1}$$

where q is the charge of the particle in units of electron charge, B the magnetic field in tesla and R the radius of curvature of the fitted trajectory in meter. The minimum p_t required of a charge track to reach the outside of the CDC is of the order of 300 MeV.

The software includes the effect of non-uniformity in the magnetic field. The spatial resolution was $\sigma \sim 170\mu$m and momentum resolution was $\Delta p_t/p_t = 0.8\%p_t$ (p_t in GeV/c). p_t is the component of the momentum in the r-ϕ plane.

3.2.3 X-Ray Detector (XRD)

The XRD is designed to detect synchotron x-rays produced by electrons as they pass through the 3 Tesla magnetic field. Energy emitted in synchotron x-ray is inversely proportional to the fourth power of the charged particle's mass,

$$\text{Radiated power} \propto \frac{E^2B^2}{m^4}$$

The electron being the lightest charge particle emits more energy than other charge particles and the XRD [22] provides a means for distinguishing electrons from hadrons. For example, a 10 GeV electron emits 1.3 MeV/m in the 3 Tesla magnetic field while a 10 GeV pion only emits 2×10^{-4}ev/m.

The XRD consists of 3 modules, covering polar angles from 37° to 143°. It occupies the space between the CDC and SHC. Figure 3.6 shows a schematic diagram of a module of the XRD. This detector was not installed until the spring of 1989 and was not used in this analysis.

3.2.4 Barrel Shower Counter (SHC)

The SHC is an electromagnetic calorimeter which measures the energy deposited by electrons, positrons and photons. It is comprised of twenty layers of gas proportional tubes interposed with lead. When a charged particle passes through the gas, it causes ionization and produces electrons. Charged and neutral particles can also interact with the lead to produce secondary charge particles which can ionize the gas. The electrons from the ionisation drift towards the anode wire which is maintained at a high voltage. These electrons gain kinetic energy T from the electric field and when T is greater than the ionization energy of the gas, fresh ions are produced. A chain of such processes leads to an avalanche of electrons and ions. The total number of secondary electrons reaching the anode is proportional to the number of initial ions, hence the name proportional counter. The secondary ions produced have lower mobility. They drift toward the cathode and do not cause an avalanche. This signal induced on adjacent cathode strips can be used to determine the position of the avalanche.

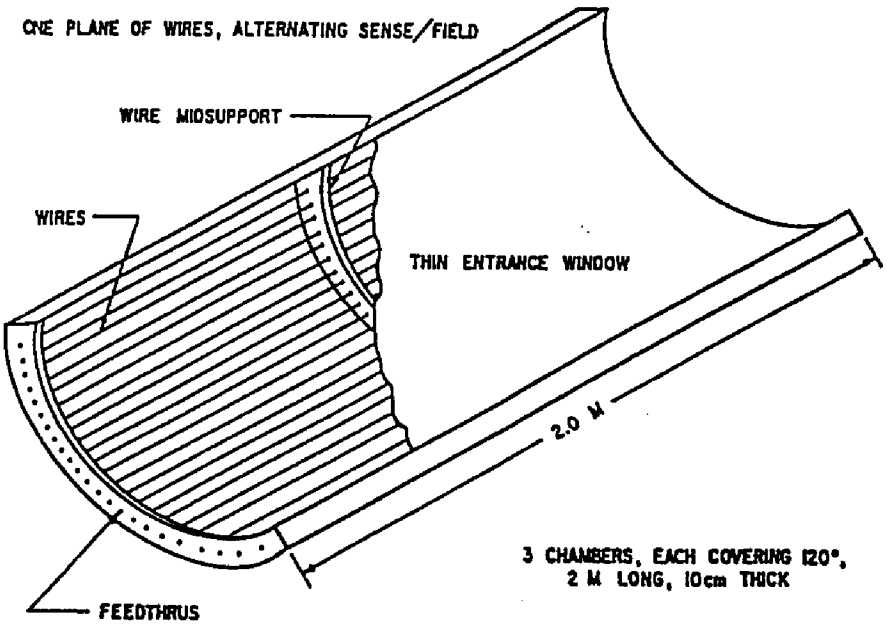

Figure 3.6: Schematic Diagram of XRD

Particle Identification

Electrons and photons

An electron or photon loses energy quickly in matter by Compton scattering, bremsstrahlung ($e \rightarrow e\gamma$) and pair creation ($\gamma \rightarrow e^+e^-$). These process repeats itself until there is no longer enough energy left for further reactions. This cascade is called an electromagnetic shower and the electron or photon deposit eventually all of their energies in the SHC. A "good" SHC particle is one with energy greater than 200 MeV and with not more than 95% of its energy deposited in any one of the five longitudinal layers. A "good" SHC particle which is matched to a CDC track within 2^0 is considered to be charged shower, otherwise it is a neutral shower. Electrons are charged particles, hence an electron shower can be matched to a CDC track. Photons, being neutral, do not leave any track in the CDC.

Electrons and charged pions

Electrons and charged pions are distinguished by their shower energy to CDC momentum (E/p) ratio and by their shower development profile. The development of an electromagnetic shower is a statistical process. The radiation length for an electromagnetic shower in lead is 0.56 cm whereas the nuclear absorption length in lead is 17.09 cm [23]. One *radiation length* is the distance over which the electron energy is reduced by a factor of e (67%) due to radiation loss (bremsstrahlung) only. One *nuclear absorption length* is the distance over which a particle such as a pion loses its energy by a factor of e by nuclear collisions. Hence electrons tend to

deposit their energies in the first few layers of the SHC while pions tend to shower deeper into the SHC. E/p for electrons $\sim$ 1 due to electromagnetic shower in the SHC while for pions E/p $\ll$ 1 (unless the pion charge exchanges: $\pi^{\pm} \rightarrow \pi^{0}$).

Neutral pions and photons

Neutral pions decay to two photons which cause electromagnetic showers. In the case of low energy pions, the pion invariant mass can be reconstructed from the two showers produced. The showers from high energies pions are not easily resolved, but are characterized by a large lateral spread. This can often be used to distinguish the pion showers from single photon showers.

Description of SHC

Figure 3.7 shows an overview of the SHC. Figure 3.8 shows the detailed view of one layer, figure 3.9 shows the longitudinal segmentation and figure 3.10 shows the layout of the phi and theta pads. The SHC consists of six sextants which form a cylinder with an inner and outer radius of 79 cm and 110 cm respectively. It is 220 cm in length covering the polar angle of $|\cos\theta| < 0.74$. Each sextant has twenty layers of gas proportional tubes made of resistive plastic material interposed with lead. The first sixteen layers of lead are 3.5 mm thick and the last four layers are 7 mm thick. The total thickness corresponds to 14.4 radiation lengths. The gas in the proportional tubes is 49.3% Ar, 49.3% C_2H_6 and 1.5% C_2H_2OH, maintained at atmospheric pressure.

SHC signals are read from both the anode wires and cathode pads which are

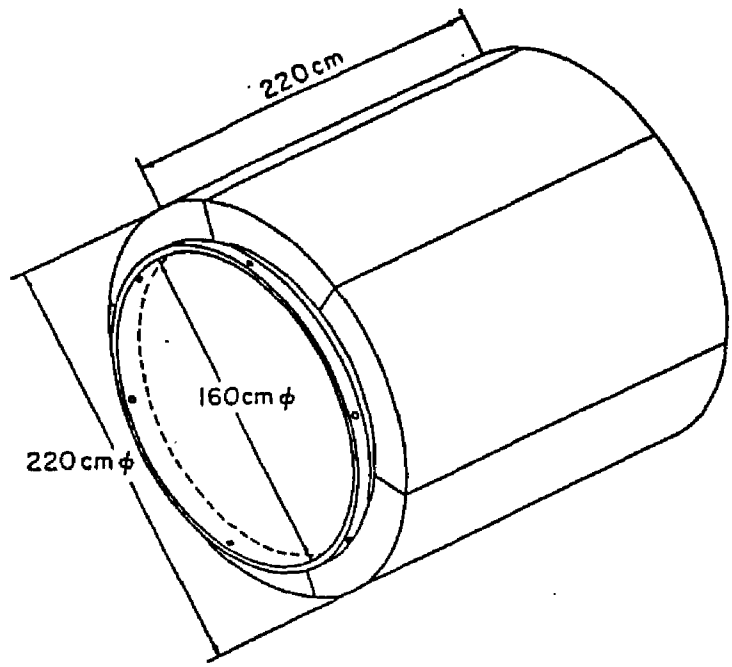

Figure 3.7: Overview of the SHC

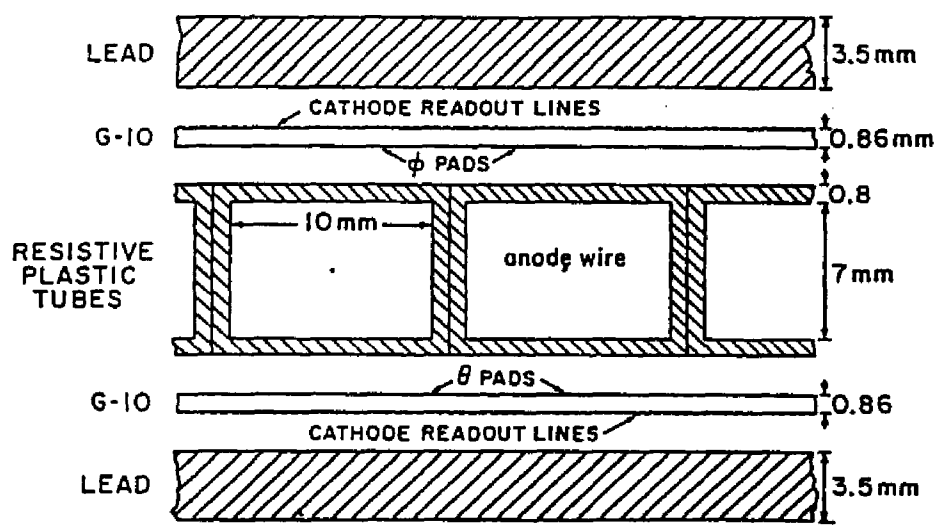

Figure 3.8: Detailed view of one layer of SHC

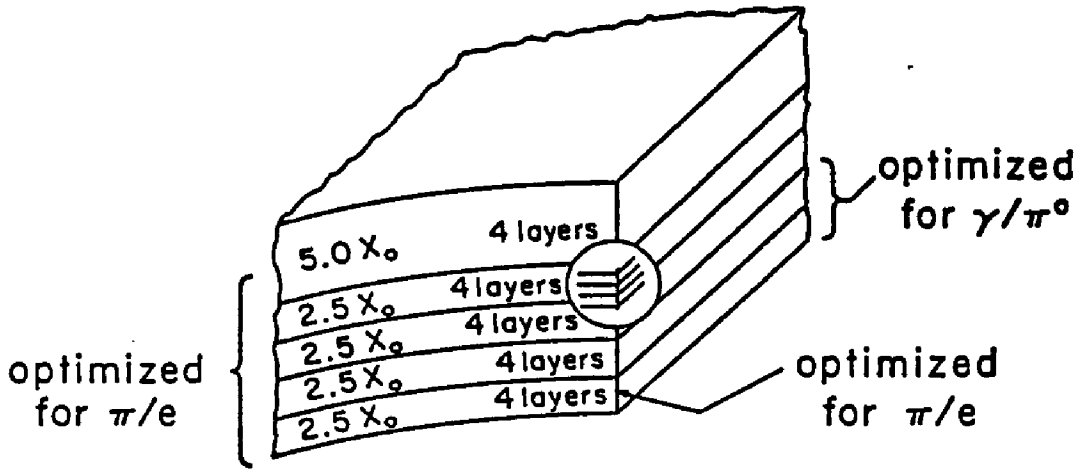

Figure 3.9: A longitudinal segmentation of SHC

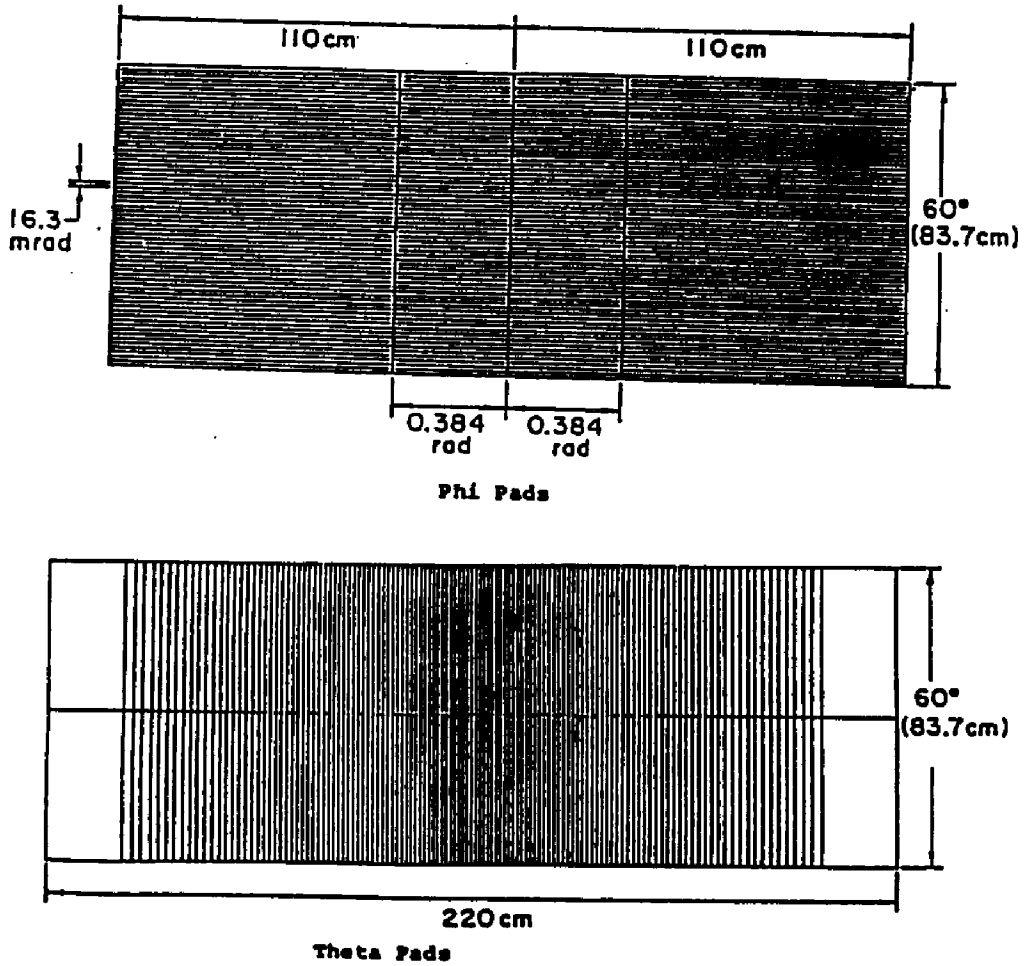

Figure 3.10: The phi and theta pads of SHC

etched on G10 boards. Four layers of cathode signals are ganged together to give a total of 5 gangs per sextant. The anode signals in each layer are also ganged together to give a total of 48 azimuthal towers. High voltage is applied to the anode wires.

There are twenty four ^{55}Fe sources embedded in the SHC. Monitor tubes are used to read their signal. This data is used to correct for fluctuations of SHC signals due to changes in gas pressure, temperature and composition.

The cathode pads measure the shower position with a precision of 3 mm or about 4 mrad in angle. The electron identification efficiency is 87% for isolated electrons and 70% for electrons in a jet. The energy resolution is $\sigma_E \sim \frac{23\%}{\sqrt{E}} + 6\%$ (E is in GeV). The minimum energy for a "good" shower cluster is 0.2 GeV.

3.2.5 Super Conducting Magnet

The high field 3 Tesla superconducting magnet [24] allows the AMY detector to be compact while achieving good momentum resolution for charged tracks. The compactness of AMY also minimizes the number of muons from the decay of pions and kaons. The probabity of decay is proportional to the path length and is given by

$$\text{Prob} \sim \frac{m_0 L}{\tau E} \tag{3.2}$$

for $m_0 L \ll \tau E$ where L is the average distance the pion or kaon travels before interacting, τ the mean lifetime, E and m_0 the energy and invariant mass of the

decaying meson.

The magnet coil was made with a superconductor (NbTi) wound into an 8 layer cylinder. The inner radius is 1.195 m, the outer radius is 1.29 m and the length is 1.54 m. The magnet weighs 17 tons and is cooled by liquid helium. During operation, a current of 5,000 amperes runs through the coil producing a 3 Tesla field in the central region.

Figure 3.11 shows the NMR measurement of the magnetic field in the central region. Figure 3.12 shows the deviation of the measured field from the field as calculated by the computer program, POISSON, and figure 3.13 shows the magnetic flux lines as calculated by POISSON.

3.2.6 Muon Detection System (MUO)

The Muon Detection System is the primary responsibility of the Louisiana State University group. The author was responsible for its maintenance and repair from March 1988 to January 1990.

The muon identification system consists of the hadron absorber, a high efficiency muon drift chamber for position measurement and scintillator counters for time-of-flight measurement.

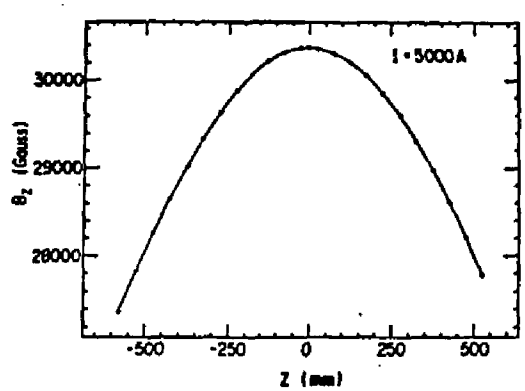

Figure 3.11: NMR measurement of the magnetic field in the central region

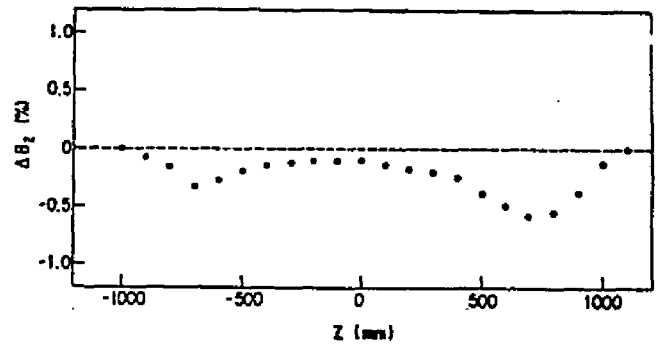

Figure 3.12: Deviation of the measured field from the field

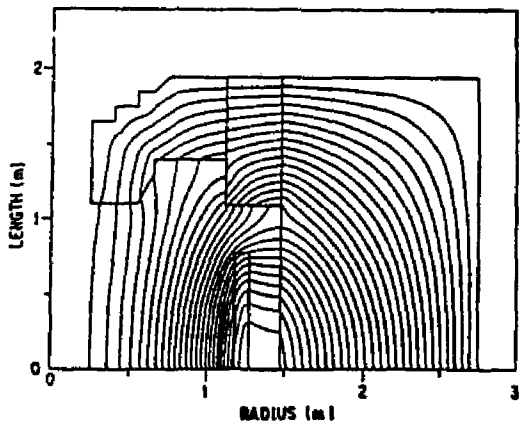

Figure 3.13: Magnetic flux lines as calculated by POISSON

Hadron Absorber and Drift Chamber

Muons do not interact strongly like hadrons nor produce electromagnetic showers like electrons. The design of a muon detector is therefore based on muons penetrating thick materials without interaction, other than ionization. A hadron, on the other hand, tends to undergo inelastic nuclear collisions with nuclei in the material resulting in the production of secondary hadrons. The secondary hadrons can again interact inelastically to produce more hadrons. One interaction length for a hadron in iron is about 16.8 cm. Few hadrons therefore will penetrate a thick iron absorbere. Electrons are even less likely to penetrate because of the short radiation length of iron (1.8 cm).

The hadron absorber, consisting of the SHC material, the superconducting magnet coil and the return yoke, has an average thickness of 165 cm equivalent of iron. This corresponds to over 9 nuclear absorption lengths. Figure 3.14 shows the thickness of the hadron absorber in terms of absorption length.

There are six sextants of drift chambers and scintillation counters located outside the magnet return yoke. Figure 3.15 shows the muon chamber configuration. There are a total of 1,184 drift tubes, each with a wire at the center. The chambers were assembled from aluminium modules. Each module consists of 4 tubes made by Kobe Steel using the extrusion method. The modules were welded together to make the different planes. Figure 3.16 shows an endview of two modules put together. Each tube has a cross-section of 10cm $\times$ 5cm. At its center is strung an anode wire

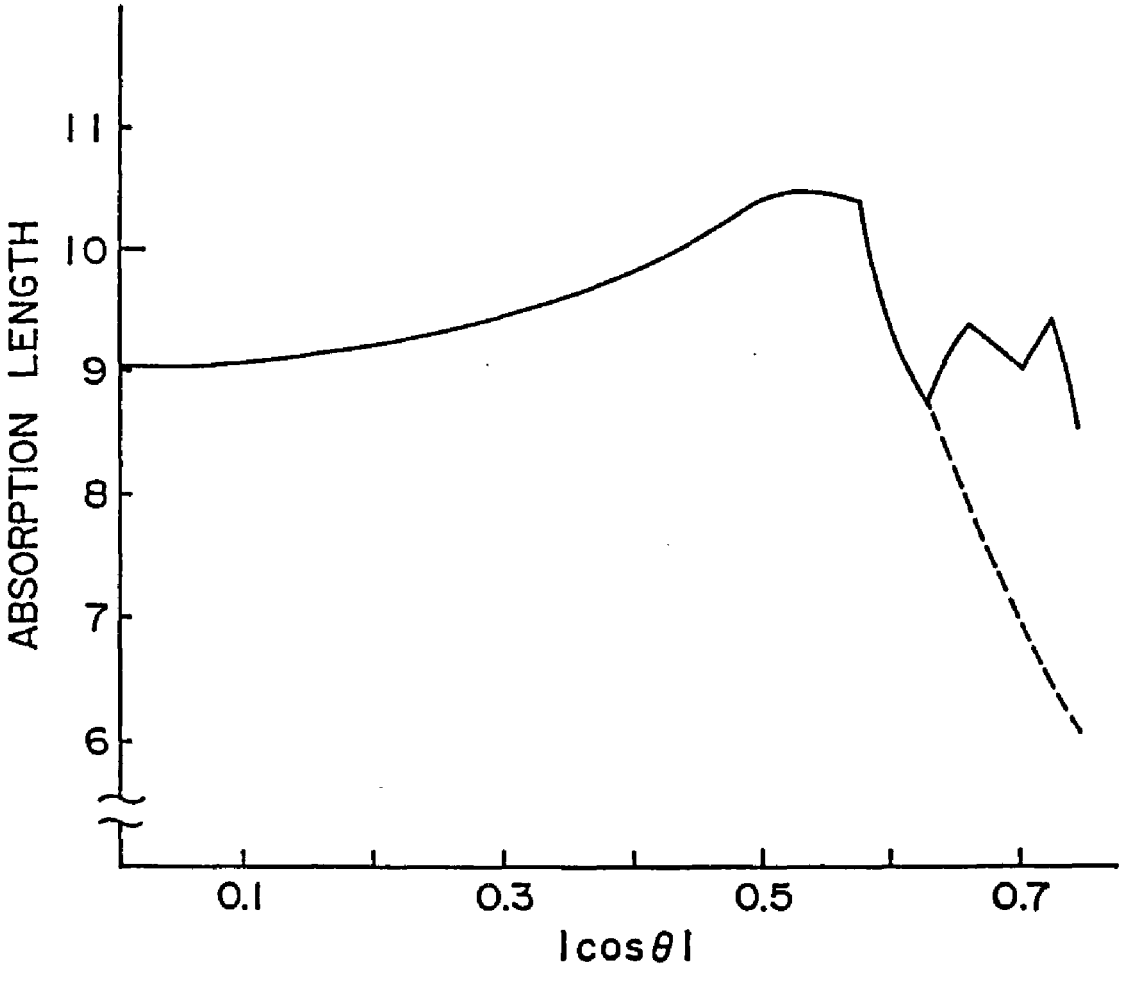

Figure 3.14: Thickness of hadron absorber in terms of absorption length

of gold plated tungsten. The anode wire has a diameter of 100 microns. Modules on adjacent planes are welded together with a 5 cm (half-cell) offset. This offset is necessary for determining whether a muon passed to the left or right side of a wire. The modules are welded together to form each sextant. Each sextant has 4 layers of drift tubes with layer 1 and 2 having anode wires strung perpendicular to the beam axis. These measure the z position of the hits. Layer 3 and 4 have wires in the direction along the beam axis. They measure the x position of the hits. The y position of the hit is determined from the geometry of the MUO. Layer 1 and 2 have 64 wires each. For layers 3 and 4, sextants 1 and 3 have 36 wires per layer, sextants 2 and 5 have 40 wires per layer and sextants 4 and 6 have 28 wires per layer. Each sextant of drift chamber is 6.5 m long and 2.8 m to 4.1 m in width. The drift chambers cover a polar angle of $|\cos\theta| < 0.74$.

High Voltage and Threshold Voltage

The high voltage here refers to the potential difference between the anode wire of the muon drift chamber and the aluminium wall which provides the ground. Threshold voltage refers to the minimum voltage required of a signal on the anode wire before it can be considered a hit. A study was made of chamber efficiency as a function of high voltage and threshold voltage [25] using cosmic rays. The results are given in figure 3.17 which shows (a) the wire hit efficiency and (b) the hit-pair efficiency. The wire hit efficiency is the efficiency of a single wire to register a hit whenever a cosmic ray particle passes through, and the hit-pair efficiency is the

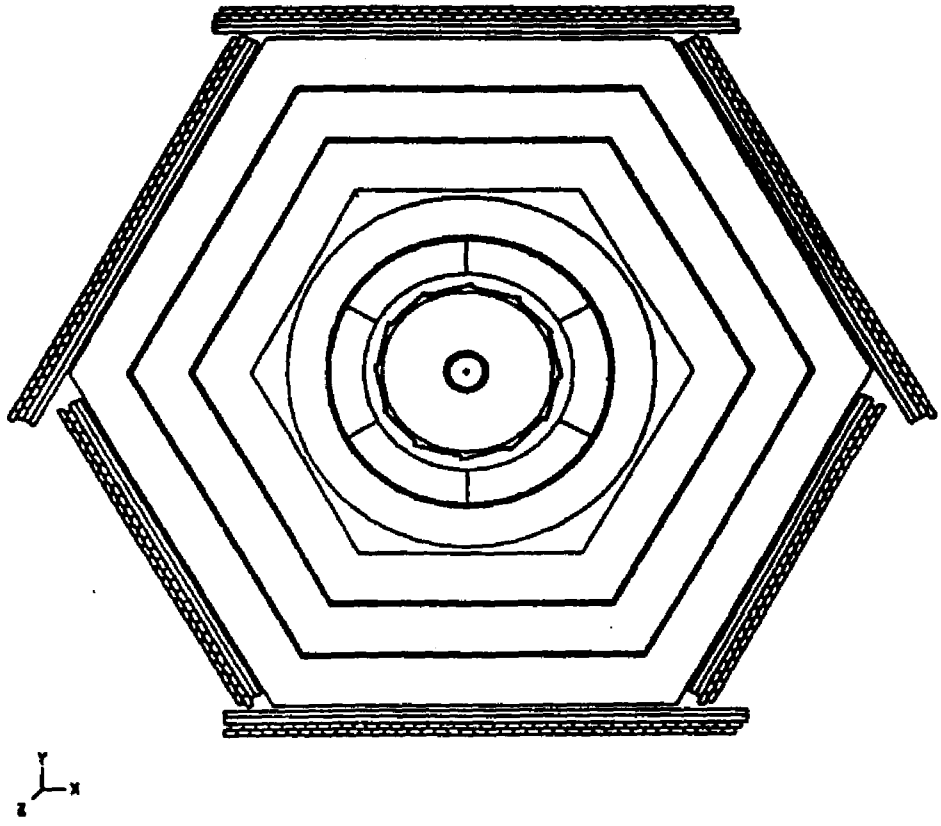

Figure 3.15: Muon chamber configuration

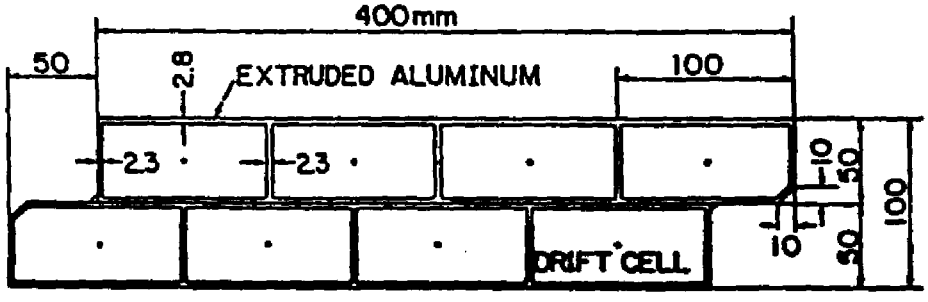

Figure 3.16: End view of two muon chamber modules welded together

efficiency of a pair of adjacent wires in different layers (layers 1-2 or 3-4) registering hits whenever a cosmic ray particle passes through. The wire hit efficiency levels off at nearly 100% and the hit-pair efficiency at 98.5% at a high voltage of around 3,000 volts with a threshold voltage of 0.8 volts. The wire hit-pair efficiency can never be 100% due to the finite size of the chamber cell walls which are 2 mm thick. Because a low threshold voltage tend to introduce more noise in the signal, the high voltage and threshold voltage were set at 3,100 volts and 1.5 volts respectively during data taking.

Finding a muon track

A muon track is defined as one which has hits in at least three of the four layers of the muon drift chamber, with two of the layers (1-2 or 3-4) having adjacent hits. Allowed combinations are shown in figure 3.18. The position of a muon track is determined from the hits and their drift time. Consider the z position of the track which is determined for the hits in layers 1 and 2. Since the distance between two anode wires in this direction is 5.0 cm, the z position of the muon track is defined as $z = z_1 + \text{zcor}$ where

$$\text{zcor} = \begin{cases} +5.0 \times \frac{t_1}{t_1+t_2} & \text{if } z_2 > z_1 \\ -5.0 \times \frac{t_1}{t_1+t_2} & \text{if } z_2 < z_1, \end{cases} \tag{3.3}$$

where z_1 and z_2 are the position of the hit wire in layer 1 and 2 respectively, and t_1 and t_2 are the drift times of the hits in layer 1 and 2 respectively. The positions of the anode wires are obtained from a survey of the detector. The x position is

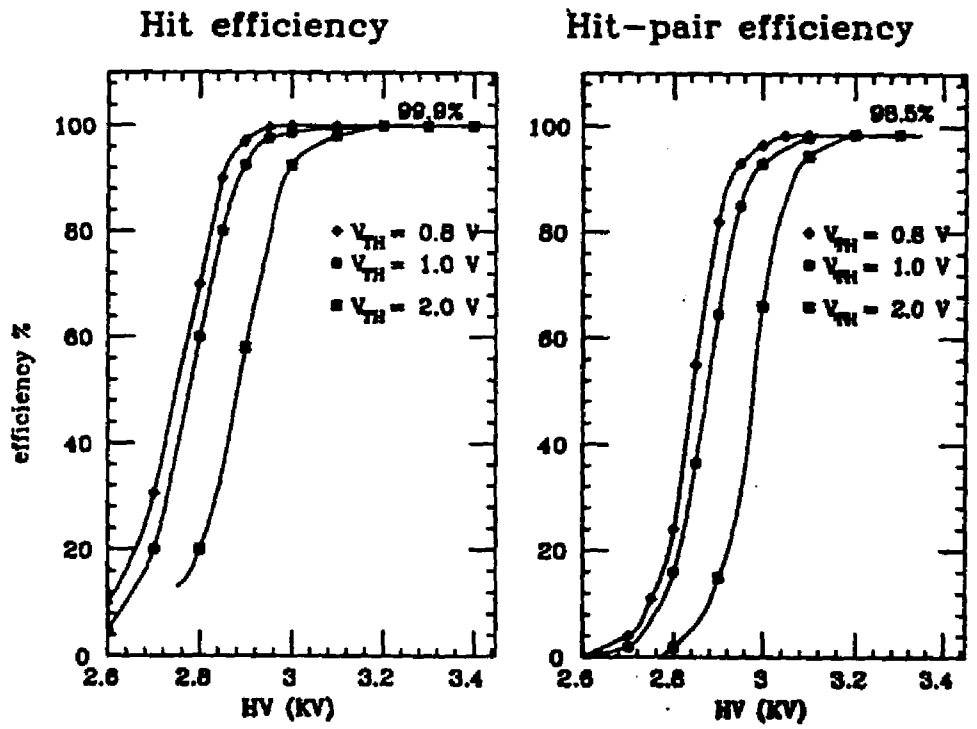

Figure 3.17: Wire hit and hit-pair efficiencies for MUO

similarly determined. In the case of only one hit wire in layer 1-2 or layer 3-4 pair, the hit position is taken as the position of the hit wire. The spatial resolution was measured by using vertical cosmic ray tracks prior to installation and found to be 1 mm. The spatial resolution after installation will not be as good since there is no correction for tracks transversing the MUO at an angle. In the worst case (t_1 or $t_2 = 0$ and the track makes an angle of 45^0), the error can be up to 25 mm.

Gas System

P10 gas (90% Ar + 10% CH_4) flows through the drift chambers at a total rate of about 1 litre per minute. Figure 3.19 shows a schematic diagram of the MUO gas system. The P10 gas is passed through a high pressure regulator and a gas filter to the input manifold. From there, each sextant of the MUO gets its gas from a separate 1/2 inch rubber tube. Figure 3.20 shows the flow of the gas within each sextant. The gas pressure inside the drift chamber is maintained at about 2 inches of water above atmospheric pressure.

Muon Scintillator Counter

The scintillator counters are the outer-most component of the AMY detector in the barrel region. There are a total of 159 plastic scintillator counters distributed over six hexagonal sextants having the same geometrical acceptance as the drift chamber. Photo-multiplier tubes measure the light produced by charged particles passing through the scintillator counter. The output signal is fed into CAMAC

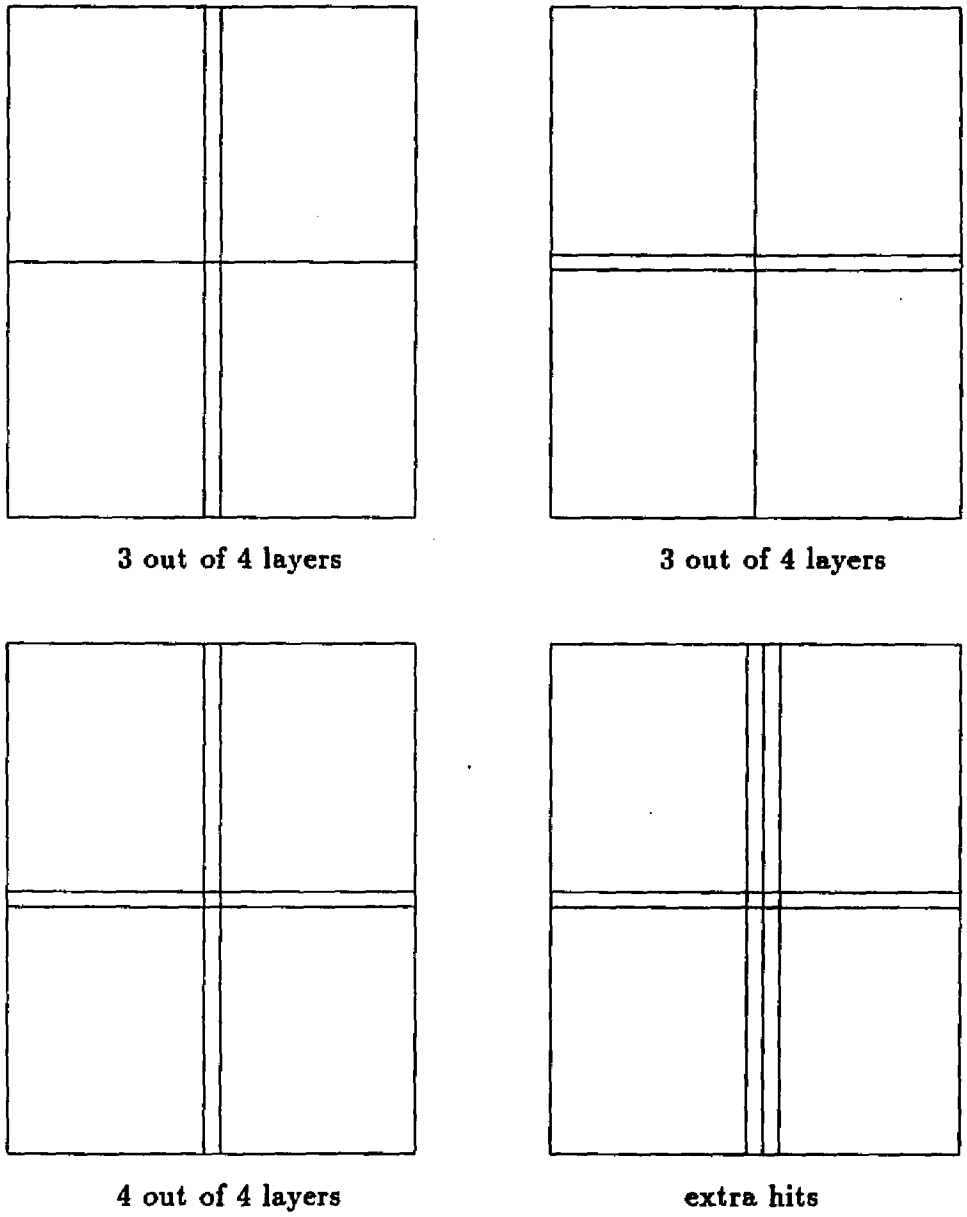

Figure 3.18: Allowed combinations of Muon tracks

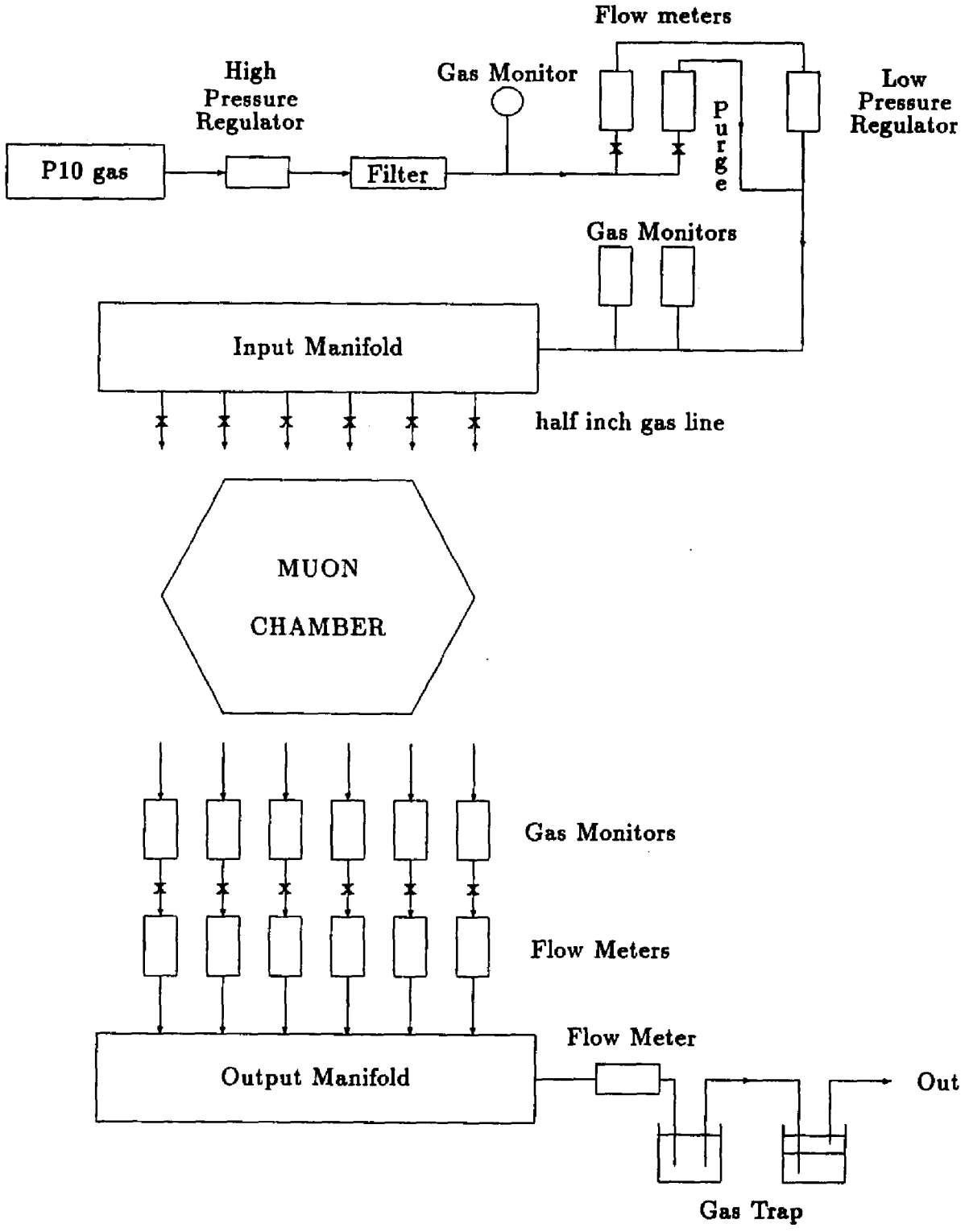

Figure 3.19: Schematic Diagram of MUO gas System

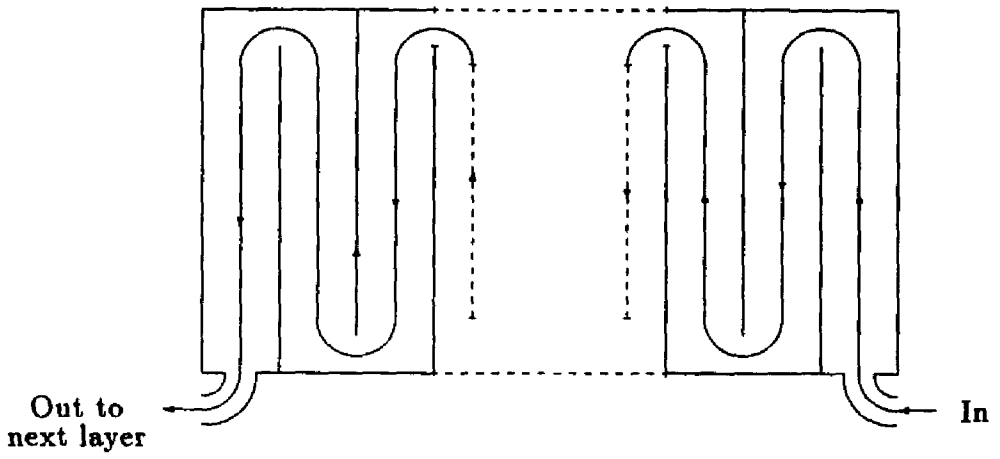

Figure 3.20: Gas flow within each sextant of MUO

discriminators, those signals above the discrimator threshold are then fed toTime-to-Analog Coverters. The time of flight of penetrating particles relative to the beam crossing time is thus measured. Using the position information from the drift chambers, a time resolution of 3 ns is achieved. This time information is used to reject background from cosmic rays.

3.2.7 End Cap Detector

The End Cap Detector consisting of the Ring Veto Counter (RVC), the Pole Tip Counter (PTC) and the Small Angle luminosity Monitor (SAM) covers both ends of the AMY detector.

The PTC consists of two lead scintillator calorimeters with a total thickness of 14 radiation lengths and one layer of proportional tubes sandwiched between them. It is designed to measure the position and energies of showers in the region

$14.6^{\circ} < \theta < 26.6^{\circ}$. The spatial resolution is 0.2^{0} in the theta direction and 0.8^{0} in the phi direction. The PTC measures luminosity with a 3% systematic error using Bhabha scattering events. It's efficiency is optimized for the detection of minimun ionizing particles. The luminosity information was used to normalize the Monte Carlo simulated events that were used for comparison with the data and also to obtain the cross sections of various processes. Figure 3.21 shows a schematic drawing of the PTC and figure 3.22 shows the integrated luminosity per day collected by AMY as measured by the PTC during the 1989 summer run.

The RVC was designed and built by P. Kirk of Louisiana State University. It covers the region $26^{\circ} < \theta < 38^{\circ}$. The RVC was made of two layers of lead sheets and scintillators, with a total thickness of 3.6 radiation lenghts. The CDC covers the region $29.5^{\circ} < \theta < 150.5^{\circ}$ and the SHC $42.3^{\circ} < \theta < 137.7^{\circ}$. The RVC was designed to provide shower information for CDC tracks entering the region just beyond the reach of the SHC. Electrons and minimum ionizing particles can be distinguished from a comparison of their deposited energy in the RVC. The energy resolution is 70%.

The SAM is used as an instantaneous luminosity montior. It consists of four calorimeters made of BaF_2 cystals. Each of the calorimeter has a cross-section of 4 cm $\times$ 6 cm. A photodiode is attached to the rear of the BaF_2 crystals to collect light from each module. The geometrical acceptance of $4^{\circ} < \theta < 6^{\circ}$ is defined by 5 mm thick plastic scintillators located at the front of the calorimeter.

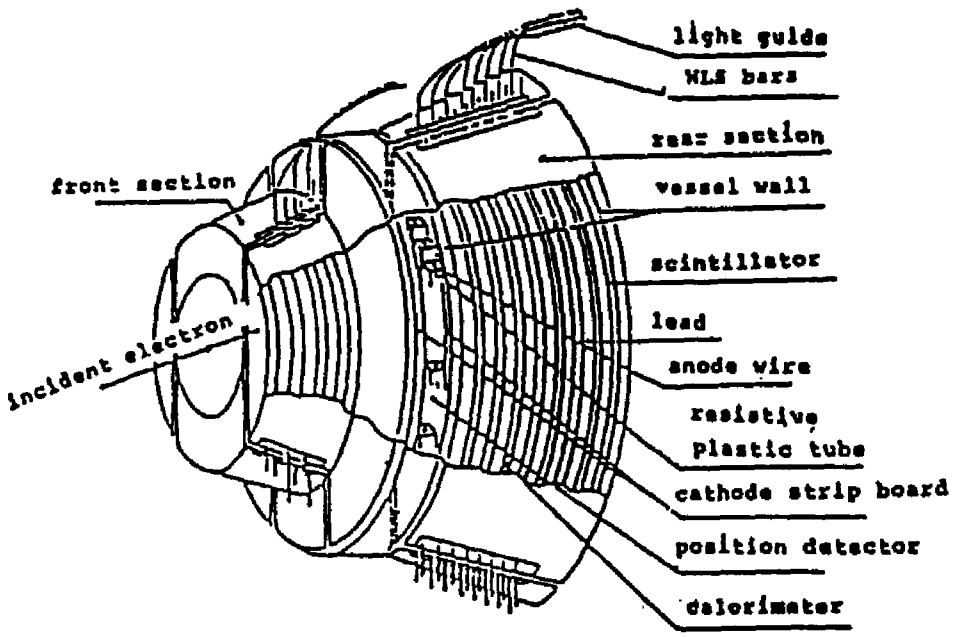

Figure 3.21: Schematic plot of the PTC

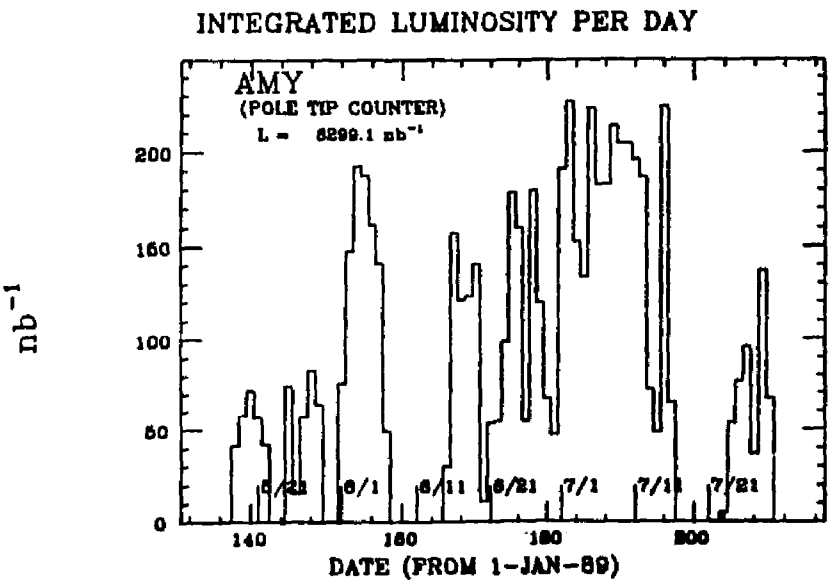

Figure 3.22: Integrated Luminosity per day during summer 1989 run

3.3 Triggering and Data Acquisition

A beam crossing signal sent to the Online computer from TRISTAN control "opens the beam gate" for 1.5 μs from the time of beam crossing. The triggering system [26] is activated whenever the beam gate is opened so that events of possible interest are stored. A beam off gate is opened for 1.5 μs after the beam crossing to provide cosmic rays trigger for background studies.

Figure 3.23 shows the list of triggers used for selecting data. The triggers that are important for selecting multihadronic events are the shower energy trigger (trigger 8), CDC tracks trigger (17), ITC tracks trigger (16) and various combinations of these three (13,15,19 and 14). The overall trigger inefficiency for selecting multihadronic events is estimated to be less than 0.3% and has a negligible effect on this analysis.

Whenever an event satisfies one of the trigger requirements, the software begins to save the event. That takes time. While it is doing this the detector is "dead", being unable to read in another event, even if it is an interesting one. The primary deadtime is about 30 ms for an average size event. The online system is ready for another event about 30 ms after it decides to save the detector information for an event. However the deadtime for the next event may be longer if it comes soon after the first event. Although the system is ready and can accept a trigger, it is has to wait until the information from the previously triggered event is read out before the VAX computer is ready to read the event. This is the secondary deadtime and

it can be up to 50 ms. At a trigger rate of 1 Hz, the dead time is around 3%. The maximun data acquisition rate is therefore limited to around 3 Hz. At this triggering rate about one event is saved out of every 100,000 beam crossings.

Data is accumulated at about 6000 events/hour during normal operation and from these only one or two inclusive muon events per day are obtained.

A schematic diagram of the data acquistion system is shown in figure 3.24. A FASTBUS and CAMAC system controlled by a VAX 11/780 was used to store data from the detector; the FASTBUS system for reading and digitizing of detector data and the CAMAC system for monitoring and control of detector performance. The VAX also performs online analysis and sends the data to a FACOM M382 computer via an optical link. The data were rearranged on the FACOM into the Tristan Bank System (TBS) format and stored in a Cassette Tape Library (CTL) for further analysis.

3.4 Monte Carlo Simulation

Electron-positron annihilation to hadrons is a complicated process and usually yields many particles in the final state. It is therefore very difficult to employ a simple analytical formula to calculate the detector effects on inclusive muon multihadronic events, especially since the AMY detector itself is very complex. Monte Carlo (MC) event simulation is therefore used to understand detector effects. There are two steps to this MC simulation:

Trigger Bit	Name of trigger
5	PTC trigger
8	Shower Total Energy
11	RVC + PTC Rear Inclusive
13	ITC 2 track + CDC + Shower Minimum Ionizing
14	ITC 2 track back-to-back + CDC
15	ITC 2 track + CDC + shower low Maj 1
16	ITC Multi Track
17	CDC Multi track
18	CDC looser multi track + shower Min Ionizing
19	(Sh Hi Maj 1 and Sh Lo Maj 2) or (Sh Lo Maj 3)
20	(Sh Hi Maj 1 and Sh Lo Maj 2) + CDC + NOT(T19)
21	ITC + CDC 2 track
22	CDC 3 or 4 track
23	ITC 2 track + Mu
24	ITC 2 track + CDC Sh Min I
26	CDC RV Dimuon
27	ITC RV Dimuon
28	ITC 2 track + CDC + RVC
30	CDC Perfect 2 track
31	CDC Perfect 1 track, Bachelor V

Figure 3.23: List of triggers used during data taking

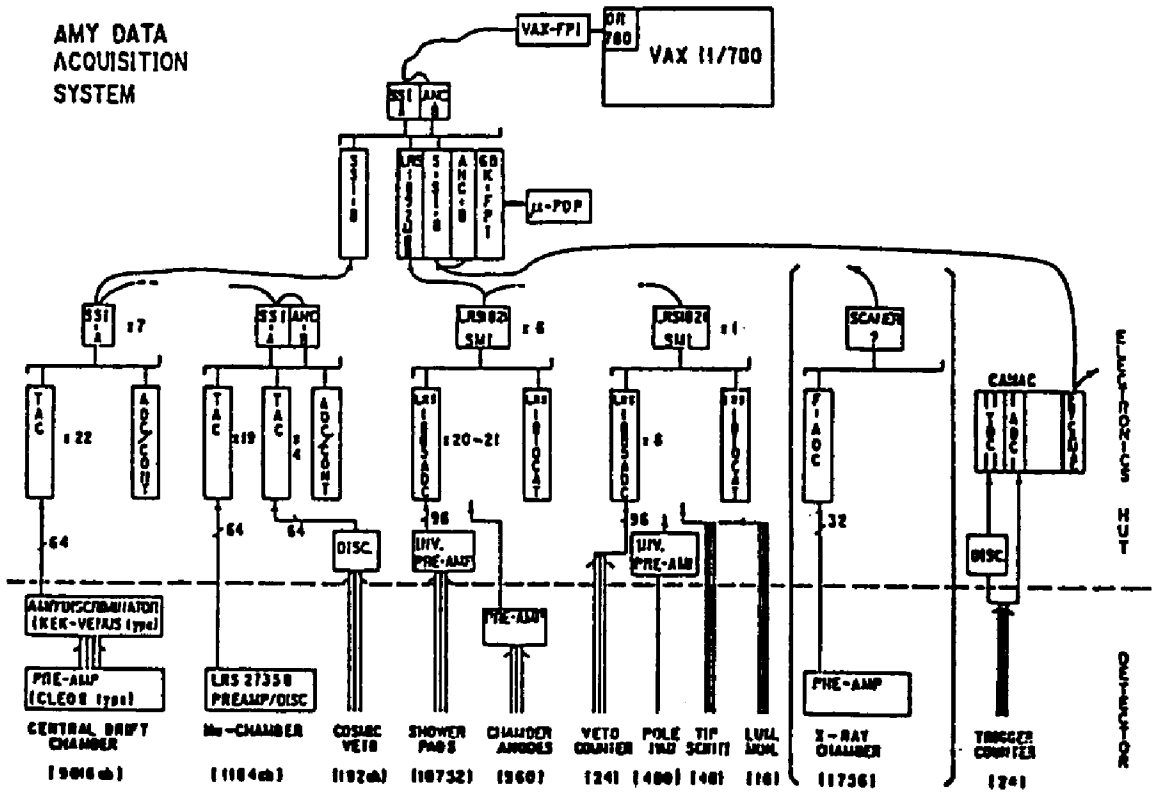

Figure 3.24: Data Acquistion of AMY

1. Event generation

2. Detector simulation

3.4.1 Event Generation

LUND 6.3 [27] was used for the generation of partons (quarks and leptons) and the String Fragmentation model [28] for the hadronization of the generated partons. In LUND 6.3, the process $e^+e^- \rightarrow q\bar{q}$ and $e^+e- \rightarrow q\bar{q}g$ are simulated with the momenta of the original partons obtained from a probability function determined from the Standard Model. Each of the generated partons branches into two other partons and each daughter parton branches into another two until a cut-off mass of about 1 GeV/c^2 is reached and the branching process stops. The leading logarithm approximation of perturbative QCD is used to calculate the branching probabilities of each parton. This development of a parton shower is called the "Parton Shower Method". A quark can branch into another quark and a gluon. A gluon can produce two other gluons or a quark-antiquark pair.

The hadronization of the quarks and gluons that were generated by the parton shower involves non-perturbative aspects of QCD and is done in the String Fragmentation model which has been found to model the processes $e^+e^- \rightarrow q\bar{q}$, $e^+e^- \rightarrow q\bar{q}g$ rather well [29]. In this model, the quark-antiquark pair is stretched out like a string. As the quark-antiquark pair moves further apart, the string breaks. In this breaking, a new quark-antiquark pair is created depending on the

energy in the string, giving two quark-antiquark pairs. The string fragmentation allows the quark-anti-quark pairs to keep dividing until there is not enough energy for further division. The short lived particles decay and at the end of the fragmentation process, only the long lived hadrons ($\pi^{\pm}$, K_S, K_L, $K^{\pm}$, p, n, Λ, $\Sigma^{\pm}$, Σ^0, Ξ^0 and Ξ^-), electrons, muons, neutrinoes and photons remain.

3.4.2 Detector Simulation

Each of the particles generated in the last section is traced through the detector in small steps. At each step, the particle may decay or interact with the various components of the detector material. The EGS4 [30] simulation program is used to simulate the electromagnetic showers produced by electrons and photons in the SHC and PTC. Hadronic showers are simulated by the GRANT [31] simulation program. The software simulates actual detector signals and creates event data records which can be analyzed using the same analysis programs as that used by experimental data.

A typical multihadronic event requires 12 seconds of FACOM CPU or 180 seconds of VAX 8800 CPU to simulate and requires 90 Kbytes of storage space.

Chapter 4

Inclusive Muon Event Selection

The objective of the data selection is to obtain a sample enriched in $e^+e^- \rightarrow b\bar{b}$ events. This is done by requiring a muon in each multi-hadronic event. Muons in e^+e^- annihilation to hadrons occur mainly from semileptonic decays of heavy quarks in the processes, $e^+e^- \rightarrow b\bar{b}$ ($b \rightarrow c\mu^-\bar{\nu}_\mu$) and $e^+e^- \rightarrow c\bar{c}$ ($c \rightarrow s\mu^+\nu_\mu$). These muons are referred to as prompt muons. Figure 4.1 shows the semi-leptonic decay of a B^- meson resulting in the production of a prompt muon. The charge of the muon is used to tag the charge of the parent quark ($b \rightarrow \mu^-$ and $\bar{b} \rightarrow \mu^+$).

Events that originate from u, d and s quark pair production do not produce many prompt muons (muons with origin at the interaction point) because they have smaller decay amplitudes as shown in table 4.1 [32]. Therefore mesons consisting of light quarks (u,d and s quarks) such as pions and kaons have longer lifetime ($\tau \sim 10^{-8}$ sec) than mesons containing a b- or c-quark ($\tau \sim 10^{-13}$sec.)

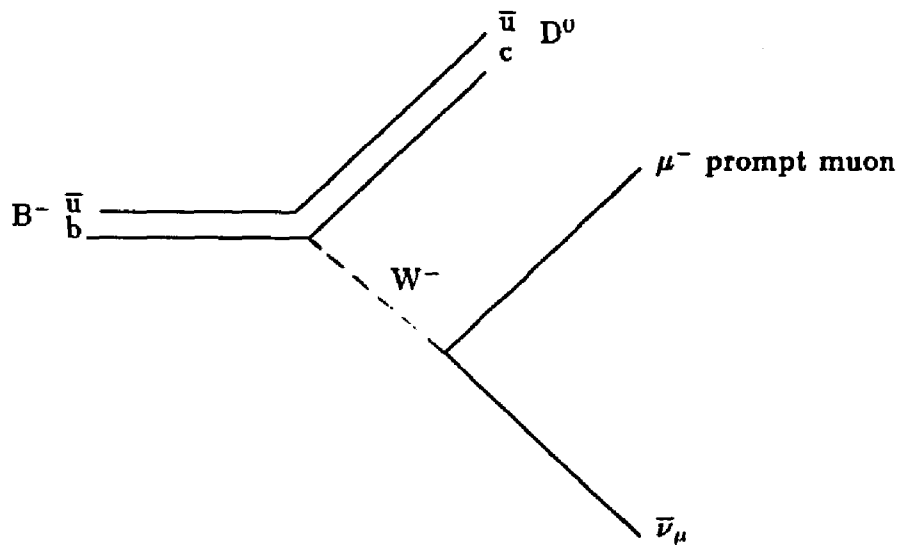

Figure 4.1: Semi-leptonic decay of $B^- \rightarrow D^0 \mu^- \bar{\nu}_\mu$

	Decay Amplitude (sec^{-1})
$\pi^\pm \rightarrow \mu\nu$	3.8×10^7
$K^\pm \rightarrow \mu\nu$	5.1×10^7
$c/\bar{c} \rightarrow \mu X$	7.6×10^{10}
$b/\bar{b} \rightarrow \mu\nu$hadrons	8.4×10^{10}

Table 4.1: Decay Amplitudes of Heavy and Light Mesons

The requirement of a prompt muon (origin at interaction point) in a hadronic event ensures that the event sample consists mostly of $e^+e^- \rightarrow b\bar{b}$ and $e^+e^- \rightarrow c\bar{c}$ processes. Backgrounds to the muon signal (hadron fakes) arise principally from hadron showers in the hadron filter, where the debris reaches the muon chamber (punchthroughs), or from the decay of $\pi^{\pm}$ and $K^{\pm}$ mesons to muons that reach the muon chamber (decay). The background includes events with punchthrough hadrons misidentified as muons or with muons from the decay of pions or kaons.

Hadronic event selection was done by the off-line analysis group. The inclusive muon events are selected from these hadronic events. This chapter gives a description of the selection criteria for hadronic events and the muon selection criteria. The background and the efficiency of the event selection are also discussed.

4.1 Multi-hadronic events

Electron-positron annihilation produce multi-hadronic events by the pair-creation of quark-antiquark pairs ($e^+e^- \rightarrow q\bar{q}$). The high center-of-mass energy imparts tremendous momentum to the quark-antiquark and forces them to move away from each other. The original quark (antiquark) excites the vacuum and generates a "sea" of $q\bar{q}$ pairs [33]; it then captures a "sea" antiquark and becomes a meson. The remaining "sea" quark picks up another "sea" antiquark to become a meson and this process continues until there is not enough energy to produce a "sea" quark-antiquark pair. As a result many hadrons are produced. This production

of hadrons from the original quark is called quark fragmentation. The Lorentz boost on the original quark tends to collimate the resulting hadrons into a jet. Consequently, multi-hadronic events are often characterized by the appearance of two jets. Sometimes there are more jets due to gluon production ($e^+e^- \rightarrow q\bar{q}g$) and subsequent gluon fragmentation. Figure 4.2 give an example of a multi-hadronic event with a muon as detected by the AMY detector.

Multi-hadronic event selection

Hadronic events tend to be collimated into jets with an angular distribution approximately of the form $(1 + \cos^2\theta)$. The total energy deposited in the barrel region of the detector is therefore expected to be nearly equal to the center-of-mass energy, $\sqrt{s}$, for many of the events. The momentum of all the particles should also be balanced. An extrapolation from lower energy data of other experiments indicate that the charge multiplicity at TRISTAN's energy region is expected to be about 15. The final corrected charge multiplicity at 56 GeV measured by AMY was 17.27 ± 0.16 [34].

Raw data were collected at a trigger rate of up to 3 Hz and between 5000 to 6000 events were collected per hour, with only one or two events that eventually pass all of the hadronic event cuts. About 80% of the triggers were background from interactions between beam particles and the walls of the beam pipe (beam-wall) or with the residual gas in the vacuum (beam-gas); and 20% of the triggers are from cosmic rays events. The interesting events, about 1% of the triggers, consist

Run: 3447, Ev: 1886, Ebeam: 28.00(Gev), Bfld: 3.03(T), Date:87-07-18, Time:14:16:35
ARRM.HADMU.MAR3.DATA
TRGbit: 29,24,18,17,15,14,13,12, 8, 7, 6,
DETbit: 7, 5, 3, 2, 1,

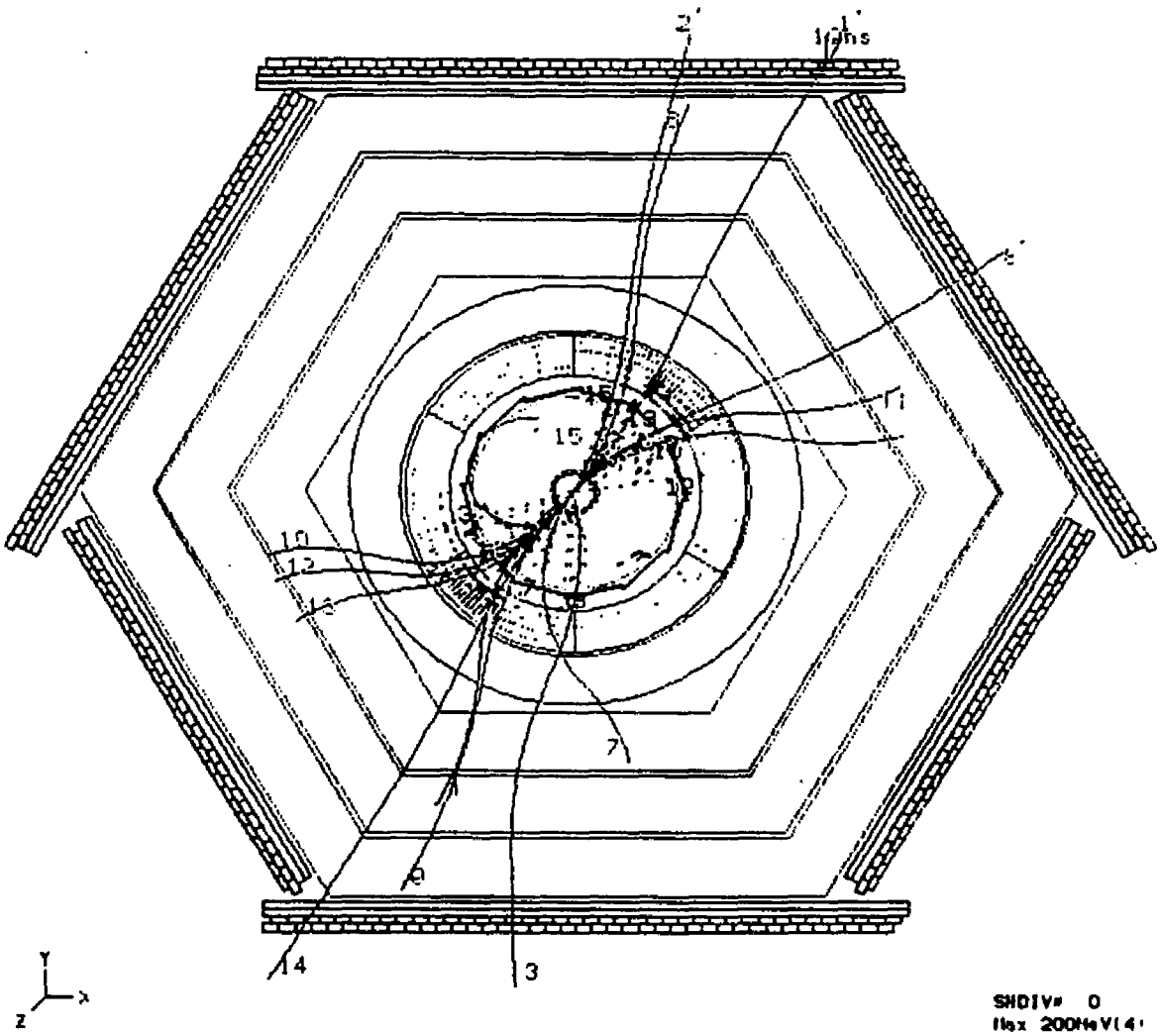

Figure 4.2: A multi-hadronic event with a muon

of multi-hadronic events, lepton pair production ($e^+e^- \rightarrow \tau^+\tau^-$, $e^+e^- \rightarrow \mu^+\mu^-$, $e^+e^- \rightarrow e^+e^-$), two photon collisions ($e^+e^- \rightarrow e^+e^-$ + hadrons, e^+e^-, $\mu^+\mu^-$, $\tau^+\tau^-$) and radiative bhabha events ($e^+e^- \rightarrow e^+e^- + \gamma$).

In order to sort through this enormous amount of raw data for the one or two hadronic events, the hadronic event selection is accomplished in three stages: [35]

- **First stage**: The first stage filter is designed to reject events which are obviously not from e^+e^- annihilation. Charge track segments were reconstructed and the cluster finding algorithm for the SHC was applied. Events that passed the following cuts were accepted:

  1. Total energy deposited in SHC, $E_{shc} > 2.8$ GeV or
  2. at least 2 charge tracks in the CDC and $E_{SHC} > 1.5$ GeV

  This filter rejects more than half the recorded events which are mainly from beam-wall and beam-gas interactions.

- **Second stage**: The trajectories and momenta of the charged tracks were determined using a fast tracking algorithm named ACE [36] (Amy CDC Event tracker). To survive this stage, the events must satisfy the following cuts:

  1. Vertex cut: At least 3 good vertex tracks are required. A good vertex track is defined to be a CDC track with $|Z_0| \leq 10$ and $|R_0| \leq 5$ cm. Z_0 and R_0 are the z and r components of the distance of closest approach to

the interaction point. In addition to the vertex requirement, a "good" CDC track must also have at least 8 axial and 5 stereo hits.

2. Shower energy cut: The total shower energy, E_{SHC} is at least 2.8 GeV.

Of the events that passed the first stage, less than 0.5% survive the second stage. Even with such a high rejection factor, the data sample is still dominated by background events.

- **Third Stage**: A more sophisticated tracking program is used to improve on the track reconstruction. This algorithm, DUET [37], was adapted from the original version developed for the CLEO detector at CESR e^+e^- storage ring. The shower cluster finding algorithm is used again, this time with a more accurate SHC calibration.

  The following hadronic cuts were developed in order to select hadronic events with a good efficiency and a high rejection for background:

  1. Total energy deposited in the SHC greater than 5 GeV (3 GeV for $\sqrt{s}$ = 50 and 52 GeV).
  2. The sum of the absolute momenta of all the "good" CDC and SHC particles, E_{vis}, greater than half the center of mass energy.
  3. Five or more "good" CDC particles.
  4. The sum of the z-component of the 3 momenta of all the "good" CDC and SHC particles (momentum balance) less than 0.4 E_{vis}.

$\sqrt{s}$ (GeV)	raw data	1st stage	2nd stage	3rd stage
52	1637857	839054	4027	490
55	1926857	1126649	2458	376
56	2452022	1553682	5300	735
56.5	617819	405324	1343	131
57	1291053	865023	3902	495
scan	726413	466706	2073	317
60	931046	526200	1798	405
60.8	2775822	1562678	6147	368
61.8	1555472	842892	4555	431

Table 4.2: Number of events passing each hadronic selection stage.

A "good" SHC particle is one with energy greater than 0.2 GeV and the energy deposited in any one of the five longitudinal layers of the SHC less than 95% of the particle's energy.

A Monte Carlo study shows that 64% of the multihadronic events pass the final hadronic cuts [38]. The background from $e^+e^- \rightarrow \tau^+\tau^-$, $\gamma\gamma$ and beam gas adds up to about 1.9%. Table 4.2 shows the number of events passing each selection stage.

4.2 Inclusive Muon Selection

The inclusive muon event sample consist of those events that pass the final hadronic event cuts and have at least one muon track. A muon track is defined by hits in the muon drift chamber in at least three out of a total of four planes and with at least one set of adjacent wires having hits in either of the double layers of the drift chamber. The timing measured by the muon scintillation counters must be consistent with the beam crossing; muon tracks with timing less than zero, counting from beam crossing are rejected. The hit position in the muon chamber must matched the extrapolated position of one of the CDC tracks within a momentum dependent matching distance cut (RCUT) described in the next section.

4.2.1 Matching the muon track to a CDC track

CDC track extrapolation

The DUET track finding program provides information about the initial position and momentum of each CDC track. Using this information, the magnetic field map and dE/dx losses, the extrapolation program [39] calculates and extrapolates the trajectory of all CDC track with momentum greater than 1.0 GeV/c.

The CDC tracks are assumed to be possible muons and the extrapolation is accomplished using the same routines as those used in the Monte Carlo simulation of muon tracks in AMY. Uncertainties in the track extrapolation arise from multiple scattering, dE/dx losses, survey, drift time, magnetic field and CDC track

reconstruction uncertainties.

RCUT

The matching distance (RDIF) is defined as the distance between the muon track and the charged track extrapolation at the muon chamber. In the local co-ordinates of the muon chamber, the z axis is defined as the direction parallel to the electron beam. The x axis is perpendicular to the z axis and lies in the plane of the muon sextant. In this co-ordinate system, all muon hits lie in the x-z plane.

XDIF and ZDIF are defined as the distance between the positions of the muon hit and the CDC extrapolated track along the x and z direction. The matching distance is then

$$\mathrm{RDIF} = \sqrt{\mathrm{XDIF}^2 + \mathrm{ZDIF}^2} \tag{4.1}$$

Figure 4.3 shows XDIF and ZDIF in an inclusive muon event. The RDIF cut is momentum dependent because the trajectory of a muon through iron is affected by multiple Coulomb scattering; a high momentum muon tends to suffer less multiple scattering and therefore has a smaller RDIF. Figure 4.4 show that the RDIF distribution of the Monte Carlo simulted events closely resembles that for the inclusive muon data.

The distribution of the momentum of Monte Carlo simulated inclusive muons at the muon chamber versus its RDIF is shown in figure 4.5. The three plots in figure 4.5 show that the decay-in-flight muons and fake muons from punchthrough

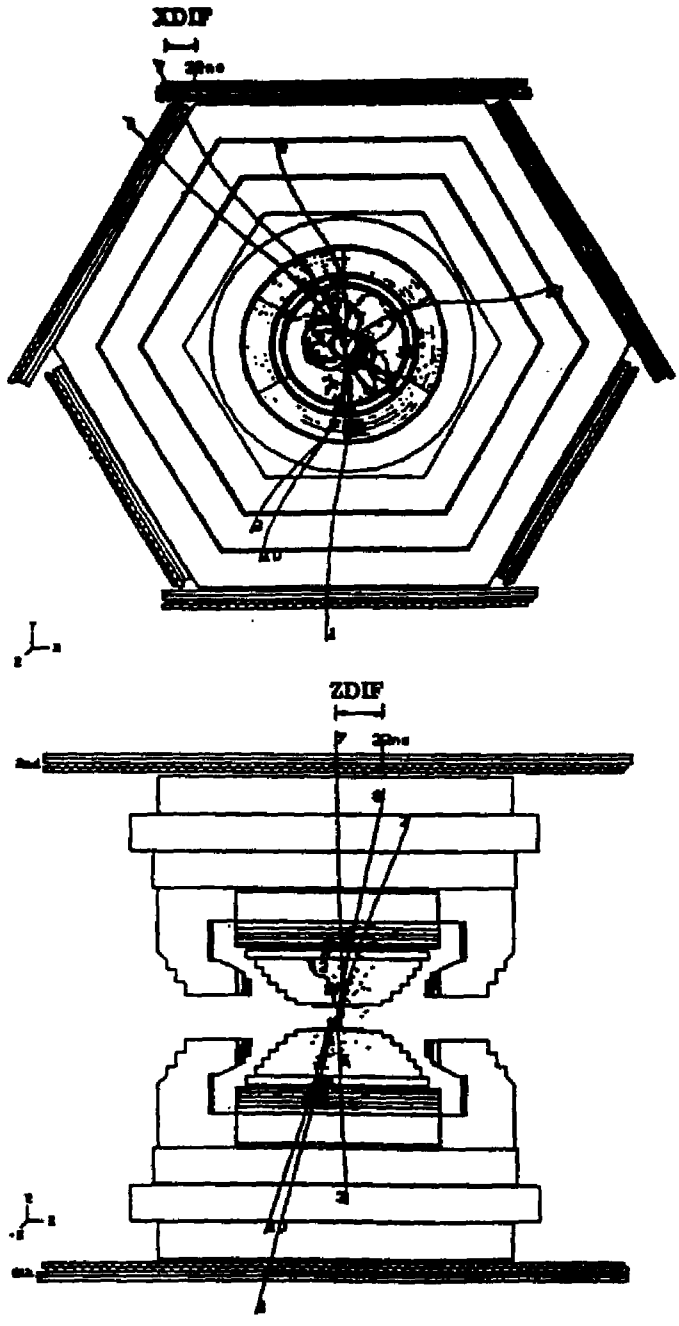

Figure 4.3: XDIF and ZDIF in an inclusive muon event

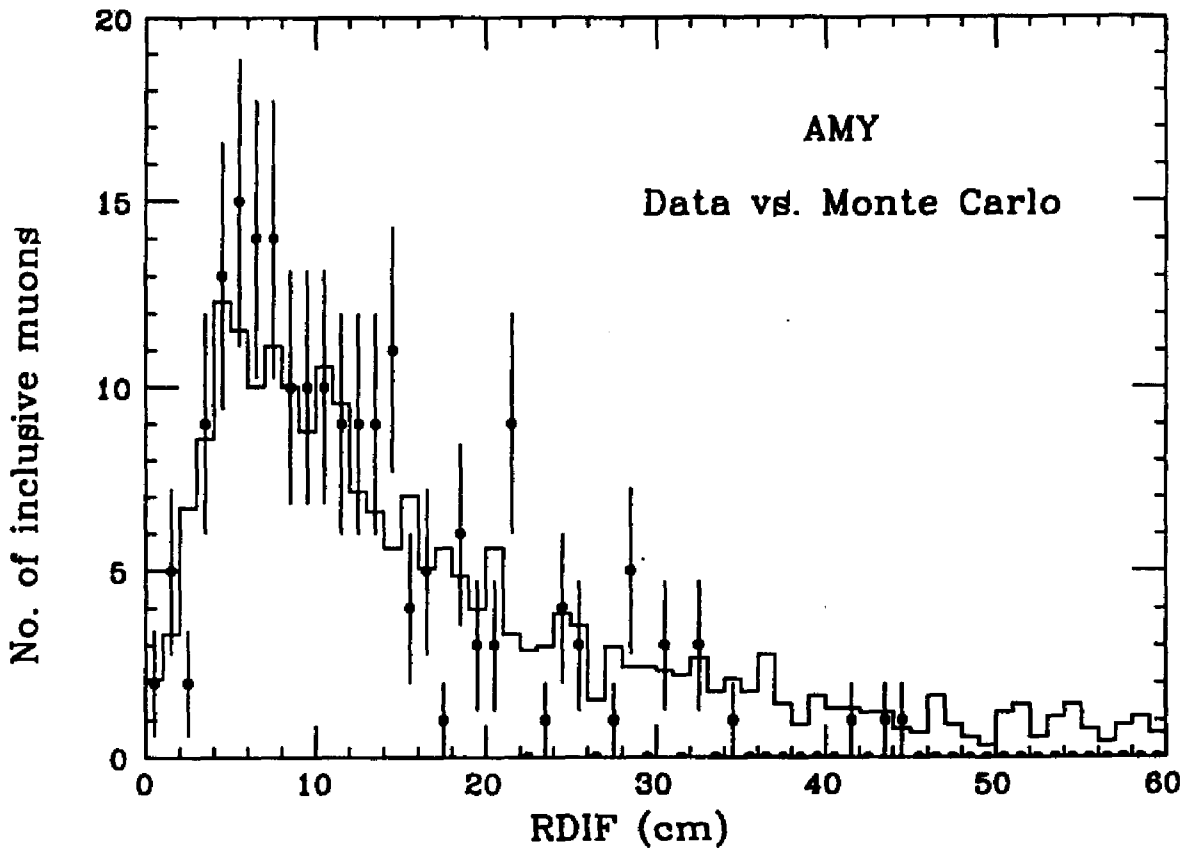

Figure 4.4: RDIF distribution for inclusive muon data and Monte Carlo

generally have bigger RDIF compared to the prompt muons. The distributions also show that RDIF tends to be smaller for higher momentum particles. A suitable momentum dependent RDIF cut (RCUT) is therefore more effective in enhancing the prompt muon fraction. The most logical way to determine this momentum dependent RCUT is to use a sample of real muons. Fortunately such a sample is available from the acollinear muon events ($e^+e^- \rightarrow e^+e^-\mu^+\mu^-$).

Figure 4.6 shows the momenta (P_F) of the muons from $e^+e^- \rightarrow e^+e^-\mu^+\mu^-$ events at the muon chamber versus RDIF. P_F is the final momemtum of a charge particle at the MUO obtained by extrapolating its initial momentum with muon energy loss as it traverses through the detector material. The accollinear muon sample was collected from $e^+e^- \rightarrow e^+e^-\mu^+\mu^-$ processes for 50 GeV $\leq \sqrt{s} \leq$ 61.4 GeV.

The muons tracks were divided into seven P_F bins of 1 GeV width. The last bin consists of P_F greater than or equal to 6 GEV. The momentum dependent RCUT is designed to accept 96% of the muon in each P_F bin, as shown by the solid line in figure 4.6. Muons with matching distances (RDIF) less than the RCUT were accepted. The statistical error for the efficiency of selecting accollinear muons using this RCUT is 0.6%. The event shown in figure 4.3 did not pass the RCUT.

Momentum cut

The minimum energy required by a muon track to penetrate the detector from the interaction point to MUO is at least 1.9 GeV. Hence any muon tracks with momentum less than 1.9 GeV are most likely to be from decay-in-flight or mis-

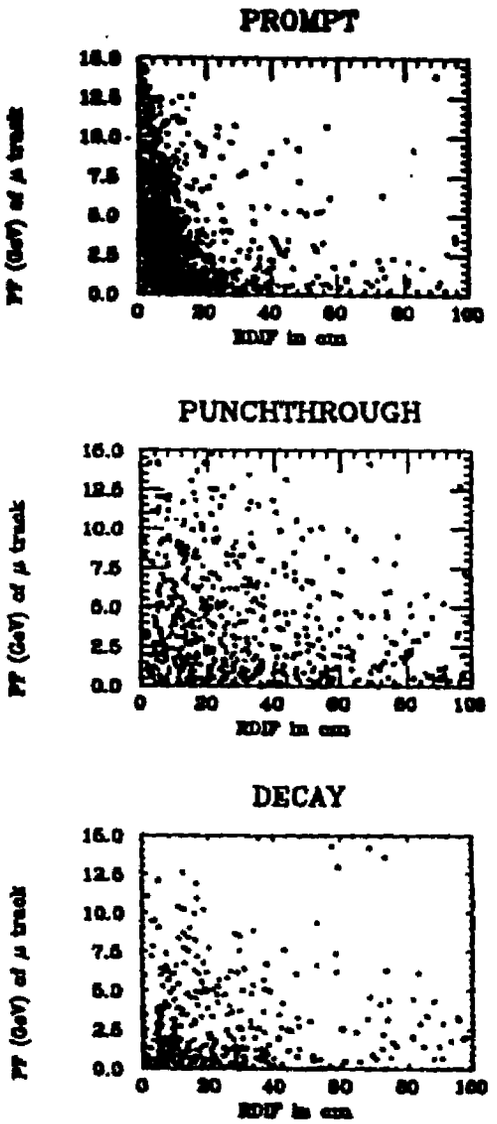

Figure 4.5: Distribution of final momentum of muons from Monte Carlo simulated events

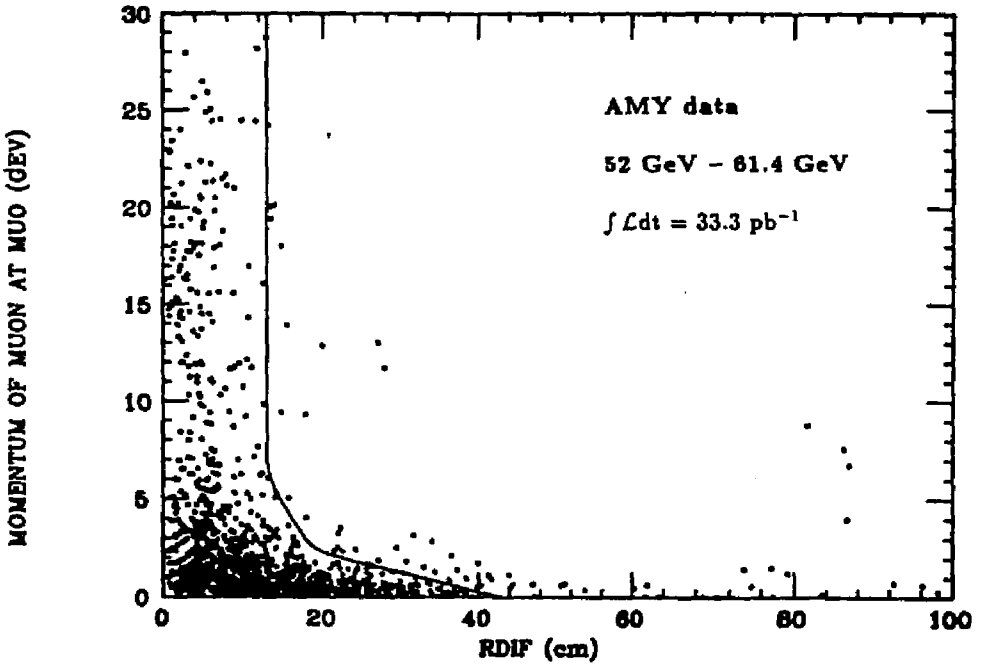

Figure 4.6: Final momentum of muons from $e^+e^- \rightarrow e^+e^-\mu^+\mu^-$ events versus matching distance (RDIF)

identification. A momentum cut of 1.9 GeV was therefore applied to the muon selection.

Figure 4.7 shows the efficiency of selecting muons from $e^+e^- \rightarrow e^+e^-\mu^+\mu^-$ events as a function of the momentum of the muon track. As can be seen, the efficiency is very low for momentum less than 2 GeV and levels off at an average of 96% for momentum greater than 3 GeV.

4.3 Background

The principal background to the multi-hadronic inclusive muon sample are events with:

1. Cosmic ray muons and accidental hits.

2. Fake muons from hadronic punchthrough.

3. Muons from pion and kaon decay.

4.3.1 Cosmic ray muons and accidental hits

This is the background where a cosmic ray or accidental hits make a muon track in coincidence with a hadronic event. The probabilty of such background was studied using a sample of bhabha events ($e^+e^- \rightarrow e^+e^-$). Bhabha events were used because they do not have any real muon tracks. Any muon track found in this sample must therefore come from cosmic ray muons or accidental hits. The bhabha

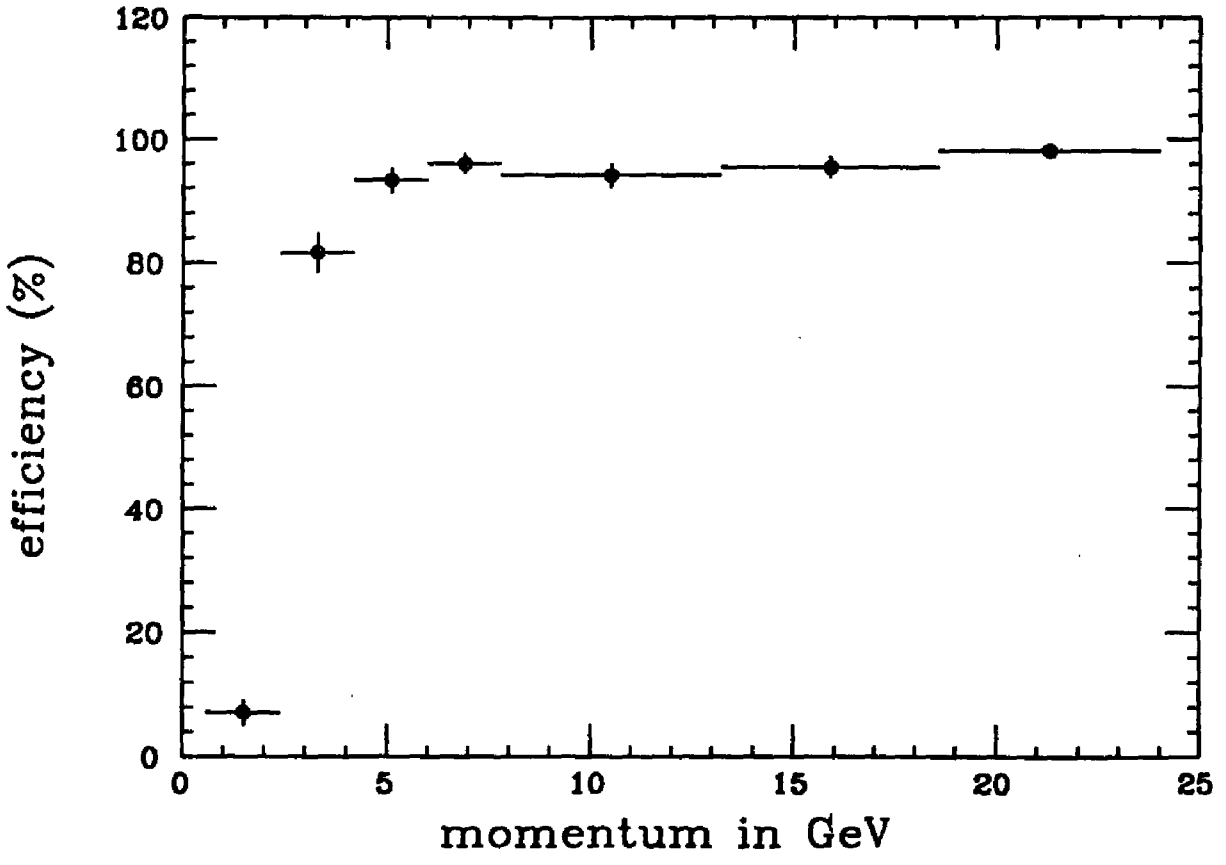

Figure 4.7: Efficiency for selecting muons from $e^+e^- \rightarrow e^+e^-\mu^+\mu^-$ events as a function of momentum

events usually have only two visible charged tracks. The criteria for the selection of Bhabha events is given by:

1. At least two SHC showers with energy greater than $E_{beam}/3$.
2. Two of the largest SHC showers matching CDC tracks within 2^{o}.
3. The matching CDC track has momentum greater than $E_{beam}/3$.
4. The acollinearity angle between the two matching tracks is required to be less than 10^{o}.

There were 7,079 Bhabha events from the 52 GeV to 60 GeV data sample. Of these there were 138 events with muon tracks. None of the events has tracks that passed the momentum dependent RCUT.

The probability of a cosmic ray or accidental hits in coincidence with a hadronic event is therefore

$$\text{Probability} < \frac{2.3}{7079 \times 2} = 0.016\% \text{ at } 90\% \text{ confidence level.} \qquad (4.2)$$

There were 2 tracks per bhabha event. The background expectation is given by the total number of CDC tracks with momentum greater than 1.9 GeV/c multiplied by the probability of a cosmic ray or accidental hits given above. On the average there are 5 CDC tracks in a multi-hadronic events with momentum greater than 1.9 GeV. The 52 GeV to 57 GeV data sample has 2192 multi-hadronic events. This gives an expectation of less than 1.7 cosmic ray events at 90% confidence level.

4.3.2 Punchthrough

Punchthrough arises from the products of hadron interactions in the SHC or iron that manage to reach the muon chamber, thereby giving a fake muon signal. A study of pion punchthrough by Harris *et.al.* [40] using data taken at the SLAC 20 GeV Spectrometer is shown in figure 4.8. The AMY Monte Carlo estimate [41] is compared with this data in figure 4.9. The 96% muon circle mentioned in the plot is the circle within which 96% of the muons will pass. GRANT/AMY in the plot refers to the result obtained from the Monte Carlo simulation using GRANT on the AMY detector. The result as shown in the plot indicates that GRANT systematically overestimates pion punchthrough by a factor of 2. The contribution from punchthrough as obtained by the Monte Carlo simulation events has therefore been reduced by a factor of two in this analysis.

There are no data on kaon punchthrough to compare with those obtained by Monte Carlo simulation. Figure 4.10 shows that the Monte Carlo punchthrough from K^+ is much higher than that from K^- and pions. This is due to the smaller K^+ cross-section for interaction in iron because K^- ($\bar{u}s$) can cause $u\bar{u}$ annihilations wiht nucleons whereas K^+ ($u\bar{s}$) cannot.

4.3.3 Muons from decay of $\pi^\pm$ and $K^\pm$

The probability of decay of $\pi^\pm$ or $K^\pm$ is given by

$$\text{Probability} \sim \frac{L}{\beta\gamma c\tau} \sim \frac{m_0 L}{E\tau} \tag{4.3}$$

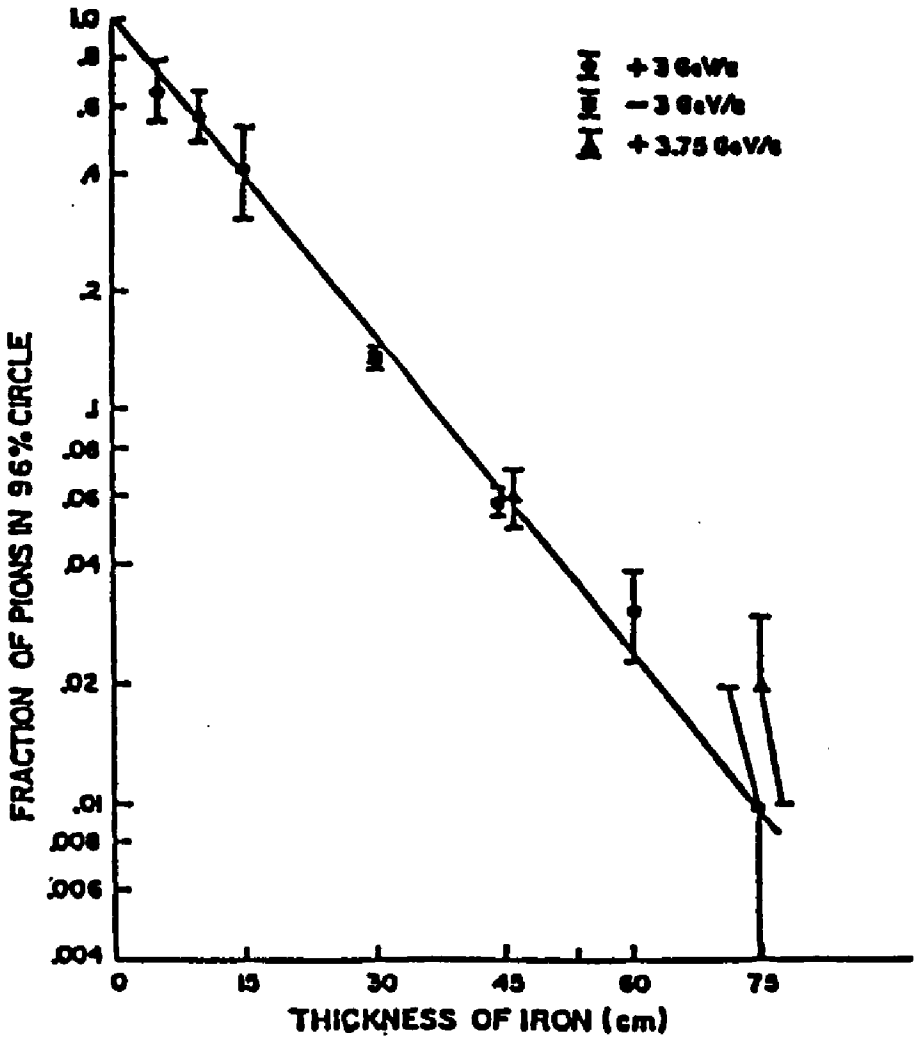

Fraction of the incident pions surviving within a multiple-Coulomb-scattering circle containing 96% of the incident muons, plotted as a function of the thickness of iron in cm.

Figure 4.8: Study of pion punchthrough by Harrris *et.al.* using data taken at the SLAC 20 GeV Spectrometer

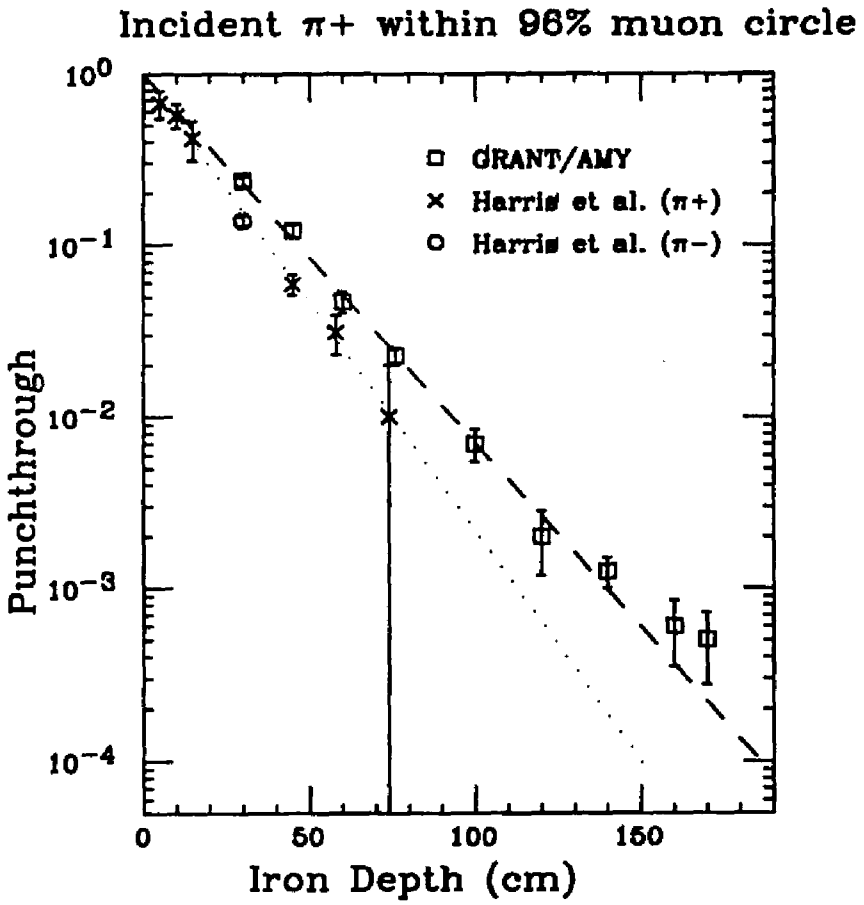

Figure 4.9: Punchthrough: SLAC 20 GeV Spectrometer pion data compare with Monte Carlo (GRANT/AMY) simulated π^+ at a momentum of 3.75 GeV

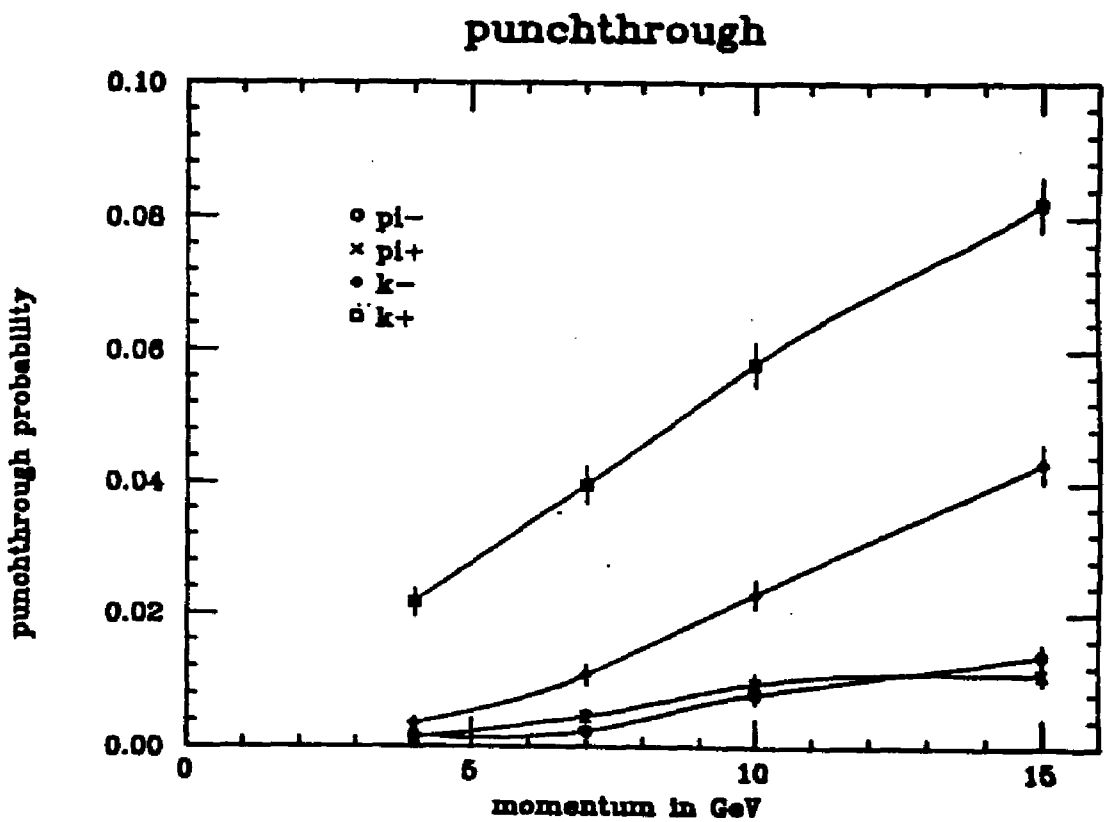

Figure 4.10: Punchthrough study using GRANT

for $m_0 L \ll E\tau$ where m_0 is the mass of the decaying meson, L is the path length, τ the mean lifetime and E the energy of the decaying meson.

In order to confirm that the Monte Carlo is giving the correct amount of decay, 5250 π^- events were generated using EPOCS [43] (**Electron POsitron Collision Simulator**) and simulated by the AMY/GRANT simulator. Each event has 4 π^- tracks with a center-of-mass energy of 4.7 GeV and θ of 90°. The first π^- track generated was random in ϕ. The next generated track has ϕ at right angles to the first. The third and fourth generated tracks have ϕ at right angle to the second and first track respectively. A typical event is shown in figure 4.11. A total of 21,000 π^- tracks were simulated and of these 51 ± 7.1 decayed to μ^- within 67 cm. The expectation from calculation was 53.5 ± 7.3.

750 K^+ events with the same event topology and energies were also simulated. 39 ± 6.2 decays were found from the 3,000 K^+ tracks within 67 cm. The branching ratio of $K^+ \rightarrow \mu\nu$ is 63.5% as given in the Particle Table and the calculation using (4.3) was therefore 36 ± 6 decays. Beyond $67/\sin\theta$ cm, the particle enters the dense shower counter and iron yoke which tend to cause it to interact rather than decay.

The agreement between the MC and calculation for $\pi^\pm$ and $K^\pm$ decay is therefore good. The total decay probability in an event also depends on the number of $\pi^\pm$ and $K^\pm$ per event. LUND was found to give a good agreement with data [44] for producing the relative number of pions, kaons and protons at 29 GeV. Prelimary results from the TOPAZ and VENUS experiments [45] also show good agreement

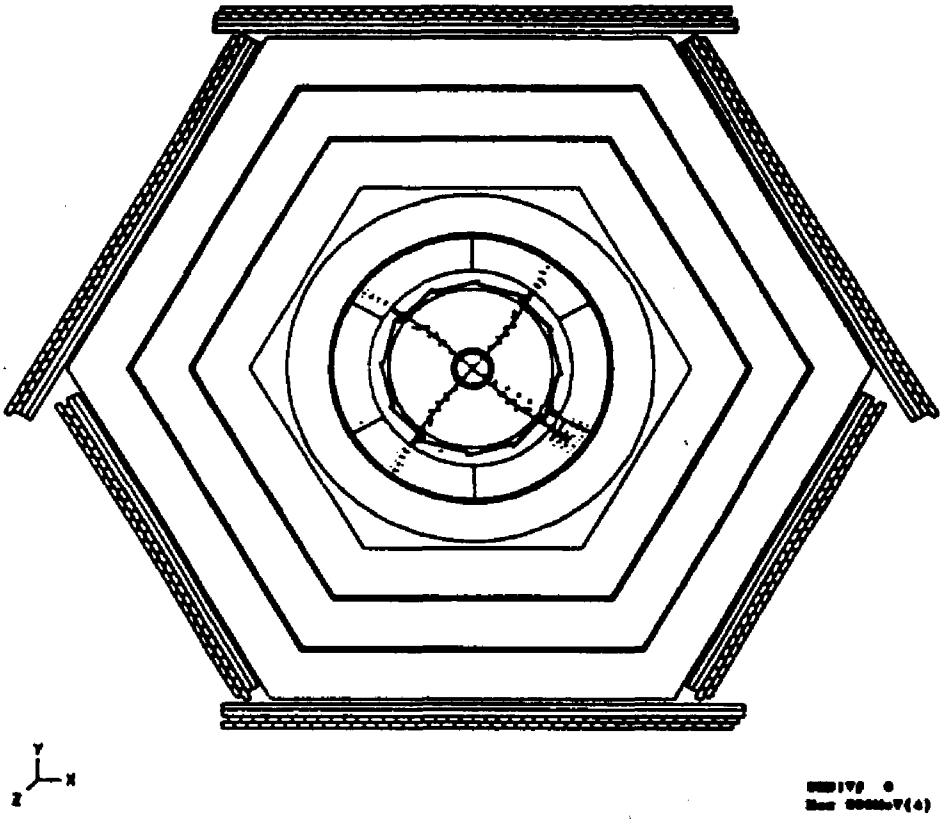

Figure 4.11: Monte Carlo 4 π tracks event

with LUND and data at TRISTAN's energies for the π : K : p ratio.

4.4 Efficiency for selecting prompt muons

The complex nature of AMY makes it impossible to use a simple analytical formula to calculate the efficiency of detecting the inclusive muon events. Monte Carlo simulated events were therefore used to give an estimate of this efficiency.

The *acceptance* for prompt muons ($b \rightarrow \mu$, $b \rightarrow c \rightarrow \mu$, $c \rightarrow \mu$) is given by

$$\text{acceptance} = \frac{\text{number of prompt muons reaching the MUO}}{\text{number of prompt muons generated}}$$

and the efficiency for selecting prompt muons is given by

$$\text{efficiency} = \frac{\text{number of prompt muons found by analysis software}}{\text{number of prompt muons reaching the MUO}}$$

Figure 4.12 shows the momentum distribution of (a) the generated prompt muons, (b) prompt muons reaching the MUO and (c) prompt muons found by the analysis software for the 67,400 five flavor monte carlo simulated multihadronic events. Figure 4.13 shows the (a) acceptance and (b) efficiency for selecting prompt muons as a function of momentum. The study shows that the acceptance for selecting prompt muons is 56% and the efficiency is 88%. The efficiency for selecting prompt muons is lower than the 96% efficiency for accepting accollinear muons because the multihadronic inclusive muons usually lie within jets making it harder to reconstruct the tracks. The larger track reconstruction errors within jets thereby lower the selection efficiency of the prompt muons. The efficiencies for selecting prompt

	efficiency
prompt (average)	88.4% ± 0.7%
$b \rightarrow \mu$	92.2% ± 1.0%
$b \rightarrow c \rightarrow \mu$	83.6% ± 1.9%
$c \rightarrow \mu$	87.8% ± 0.9%
decay	81.4% ± 1.5%
punchthrough	49.1% ± 2.0%
overall	82.0% ± 0.7%

Table 4.3: efficiency for selecting prompt and fake muons

and fake muons are summarized in table 4.3. The expression $b \rightarrow \mu$ is used for the process $B \rightarrow X\mu^{-}\overline{\nu}_{\mu}$ where B is the b flavor hadron.

4.4.1 MUO and CDC efficiency

The MC simulation assumed that AMY is a perfect 100% efficient detector. This is not true in practice. On top of the efficiencies as found by the MC simulation, the factors of muon track finding efficiency and CDC efficiency need to be added. The efficiency for CDC track reconstruction is 95% ± 0.8% [46] for multi-hadronic events. The muon track finding efficiency is the efficiency of satisfying the tracking requirements of 3 out of 4 layers discussed in section 3.2.6. This has been determined using cosmic ray tracks. From penetrating cosmic rays which satisfy the

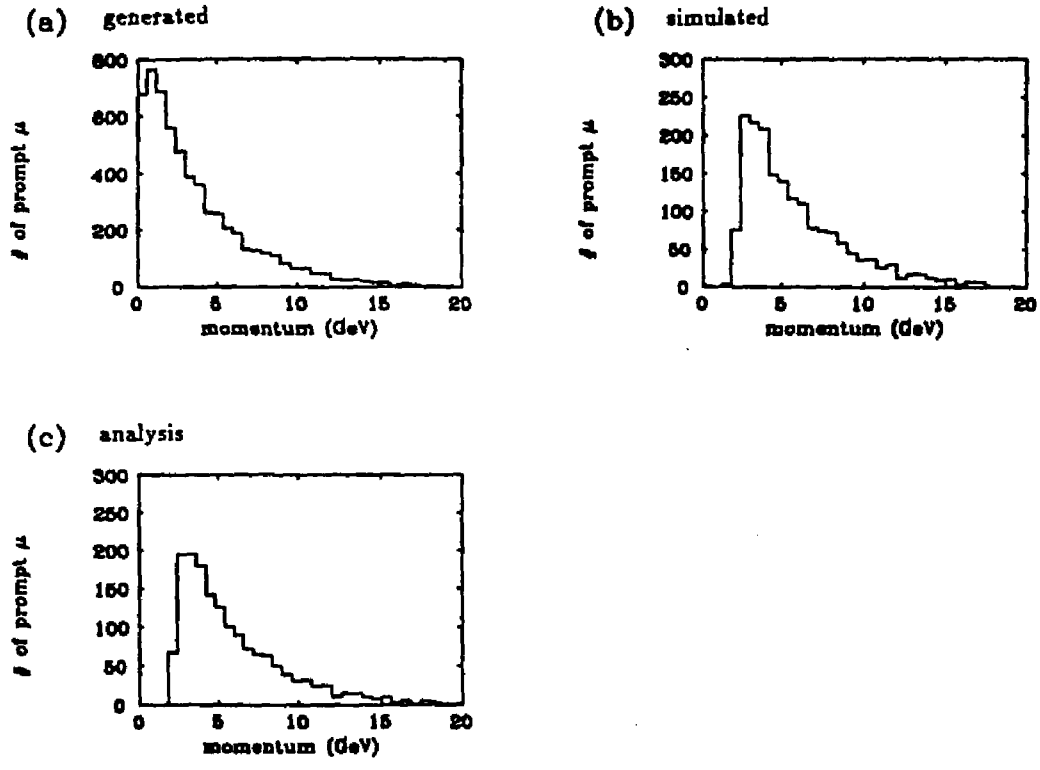

Figure 4.12: Monte Carlo prompt muon momentum distribution (a) generated prompt muons, (b) prompt muons reaching the MUO and (c) prompt muons found by analysis software

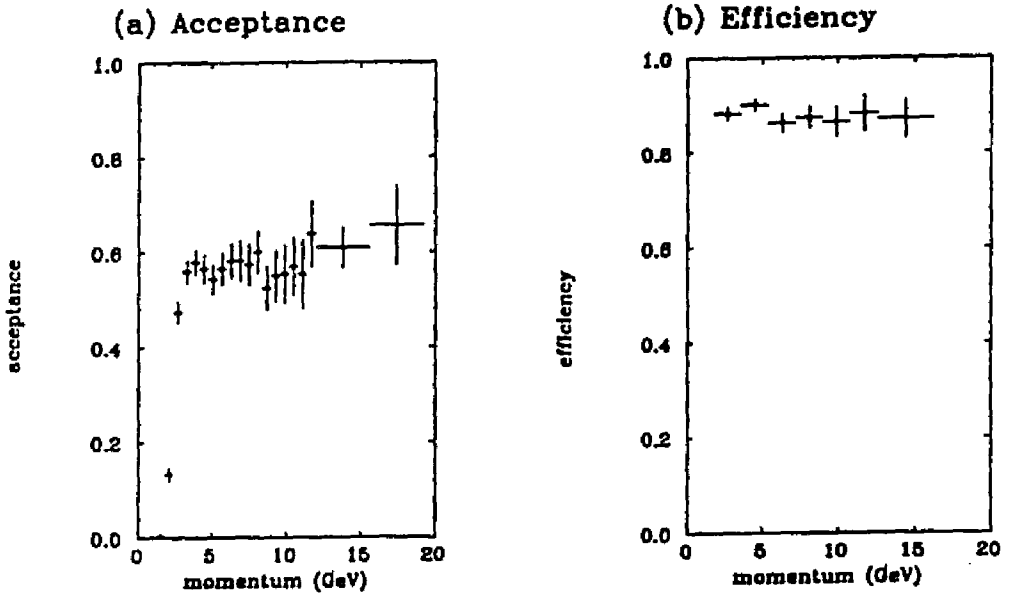

Figure 4.13: Acceptance and efficiency for selecting prompt muons using Monte Carlo simulated events

minimum 3 layer requirement, 98% of them have the remaining 4th layer hit as well. Therefore, the expected fraction of muons which should satisfy the minimum 3-layer requirement is at least 98%.

4.5 Data Sample

Data taken from June 1987 to July 1989 were used for the analysis of $b\bar{b}$ asymmetry. The center-of-mass energy $\sqrt{s}$ was from 52 GeV to 61.4 GeV and total integrated luminosity was 33.3 pb^{-1}.

Tables 4.4, 4.5 and 4.6 summarize the data used for this analysis. The scan was a series of runs between 57.25 GeV and 59.5 GeV.

4.5.1 Composition of inclusive muon data

A summary of the composition for 67,400 Monte Carlo simulated multihadronic events after applying the hadronic and muon selection cuts is given in table 4.7.

Mis-identified muons occur when the muon analysis program matches a muon to the wrong CDC track. Figures 4.14 shows a few examples of such events. This can happen when the CDC tracks are very close together. Most of the mis-identified tracks are from punchthrough and decay-in-flight fakes.

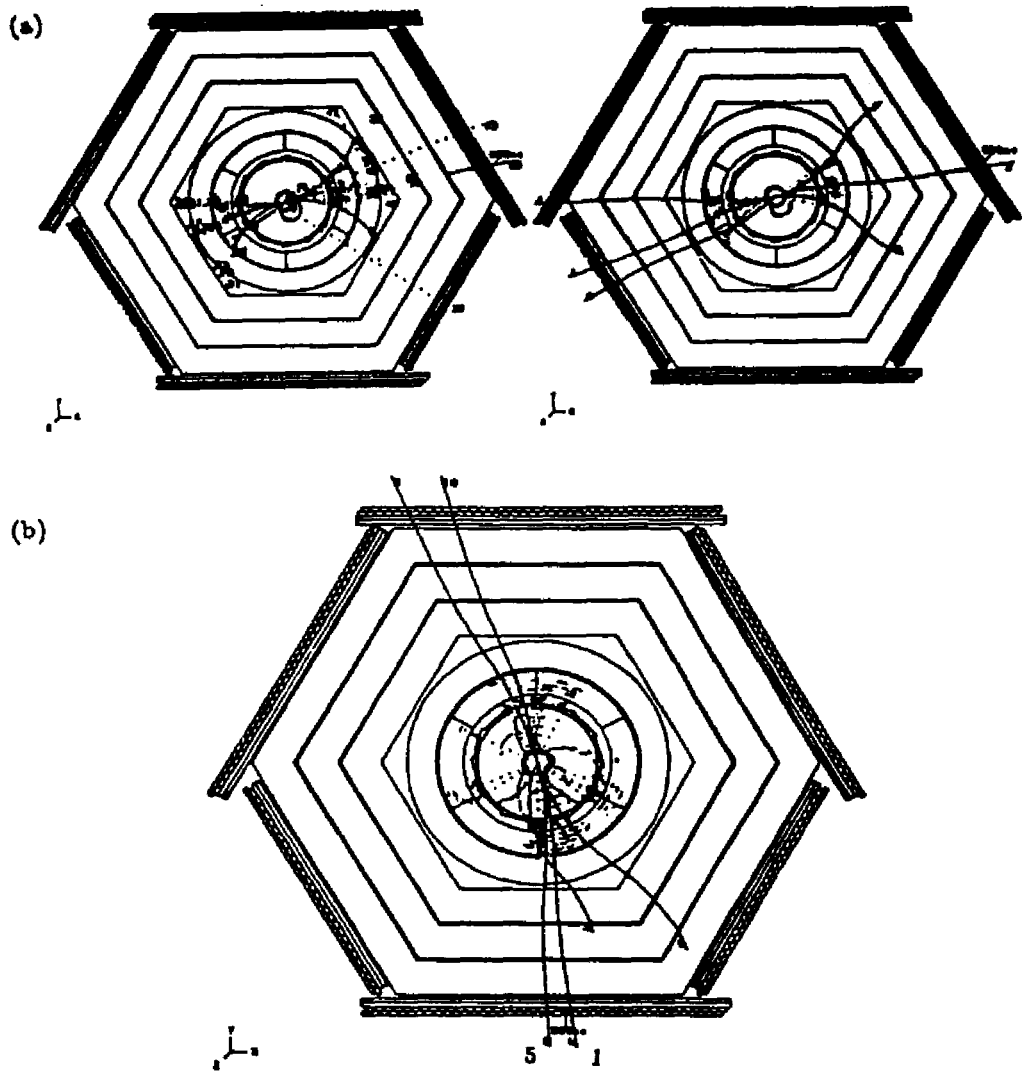

Figure 4.14: misidentified tracks (a) punchthrough track from manget was mistaken for a track inside the CDC. The plot on the left shows the tracks as they were simulated. The plot on the right shows the tracks as interpreted by the analysis software. (b) track 5 was the prompt muon. Track 1 was chosen as the muon candidate because it has a smaller matching distance.

4.6 A check for detector biasses

Checks were done to be sure that the detector is not biassed. The number of muons of both charges in the forward and backward region as well as the number of positively and negatively charged muons is shown in table 4.8.

A_{FB} is given by

$$A_{FB} = \frac{\text{number of forward } \mu^{\pm} - \text{number of backward } \mu^{\pm}}{\text{number of forward } \mu^{\pm} + \text{number of backward } \mu^{\pm}}$$

and $A_{\pm}$ is given by

$$A_{\pm} = \frac{\text{number of } \mu^{+} - \text{number of } \mu^{-}}{\text{number of } \mu^{+} + \text{number of } \mu^{-}}$$

For a symmetrical detector A_{FB} should be zero. $A_{\pm}$ will be zero for prompt muons from $b\bar{b}$ or $c\bar{c}$ production but not necessarily for muons from $\pi^{\pm}$, $K^{\pm}$ decay or punchthrough. Since the data is dominated by the prompt muons, it is therefore expected that $A_{\pm}$ will also be close to zero. These two numbers were found to be zero within statistical errors.

$\sqrt{s}$ (GeV)	52	55	56 + 56.5	57
hadronic event	482 ± 22.0	368 ± 19.2	850 ± 29.2	492 ± 22.2
MC expectation	475.6 ± 6.2	359.3 ± 7.1	752.6 ± 8.1	517.7 ± 5.1
inclusive μ event	28 ± 5.3	16 ± 4.0	49 ± 7.0	26 ± 5.1
MC expectation	25.0 ± 1.5	21.9 ± 1.8	46.0 ± 2.1	31.7 ± 1.3

Table 4.4: Summary of inclusive muon data with center-of-mass energies between 52 and 57 GeV

$\sqrt{s}$ (GeV)	scan	60	60.8	61.4
hadronic event	317 ± 17.8	405 ± 20.1	368 ± 19.2	431 ± 20.8
MC expectation	352.1 ± 3.3	387.5 ± 3.6	370.1 ± 4.1	458.2 ± 5.1
inclusive μ event	25 ± 5.0	9 ± 3.0	19 ± 4.4	20 ± 4.5
MC expectation	21.9 ± 0.9	24.0 ± 0.9	22.1 ± 1.0	27.4 ± 1.3

Table 4.5: Summary of inclusive muon data with center-of-mass energies between 57.25 and 61.4 GeV

$\sqrt{s}$(GeV)	Luminosity (pb−1)	$\sqrt{s}$(GeV)	Luminosity (pb−1)
52.00	3.98 ± 0.04	55.00	3.27 ± 0.04
56+56.5	6.98 ± 0.05	57.00	4.40 ± 0.05
57.25	0.0582 ± 0.004	57.50	0.0803 ± 0.005
57.75	0.0781 ± 0.005	58.00	0.0772 ± 0.005
58.50	0.8010 ± 0.016	58.75	0.0865 ± 0.005
59.00	0.7210 ± 0.021	59.05	0.5040 ± 0.013
59.125	0.7560 ± 0.005	59.25	0.0984 ± 0.006
59.50	0.0724 ± 0.005	60.00	3.55 ± 0.04
60.80	3.49 ± 0.05	61.40	4.32 ± 0.05

Table 4.6: Integrated luminosity of the data sample

P_t cut (GeV/c)	0.00	0.50	0.70	1.00	1.50
total muon	3,110 (100%)	2,120 (100%)	1,631 (100%)	1,094 (100%)	576 (100%)
prompt muon	2,130 (68.5%)	1,532 (72.3%)	1,220 (74.8%)	851 (77.8%)	457 (79.3%)
$b \to \mu^-$	682 (21.9%)	633 (29.9%)	583 (35.7%)	475 (43.4%)	264 (45.8%)
$b \to c \to \mu^+$	306 (9.8%)	193 (9.1%)	133 (8.2%)	68 (6.2%)	30 (5.2%)
$c \to \mu$	1,142 (36.7%)	706 (33.3%)	504 (30.9%)	308 (28.2%)	163 (28.3%)
punchthrough	317 (10.2%)	208 (9.8%)	152 (9.3%)	97 (8.9%)	51 (8.9%)
decay-in-flight	521 (16.8%)	306 (14.4%)	208 (12.8%)	121 (11.1%)	55 (9.6%)
misidentification	142 (4.6%)	74 (3.5%)	51 (3.1%)	25 (2.3%)	13 (2.3%)
$b \to \mu^-$	2 (0.06%)	1 (0.05%)	0 (0.00%)	0 (0.00%)	0 (0.00%)
$b \to c \to \mu^+$	5 (0.16%)	1 (0.05%)	0 (0.00%)	0 (0.00%)	0 (0.00%)
$c \to \mu$	23 (0.74%)	10 (0.47%)	8 (0.49%)	2 (0.18%)	2 (0.35%)
punchthrough	80 (2.57%)	49 (2.31%)	35 (2.15%)	19 (1.74%)	8 (1.39%)
decay-in-flight	32 (1.03%)	13 (0.61%)	8 (0.49%)	4 (0.37%)	3 (0.52%)

Table 4.7: Number of inclusive muon events

$\sqrt{s}$ (GeV)	Backward $\mu^\pm$	Forward $\mu^\pm$	A_{FB}
52 to 61.4	102	95	-0.04 ± 0.07
$\sqrt{s}$ (GeV)	μ^-	μ^+	$A_\pm$
52 to 61.4	101	96	-0.03 ± 0.07

Table 4.8: A check for detector biasses

Chapter 5

Analysis

192 multihadronic inclusive muon events were found from the data sample accumulated between $\sqrt{s}$ = 52 and 61.4 GeV. The data sample corresponds to an integrated luminosity of 33.3pb^{-1} and contained events of interest, namely $e^+e^- \rightarrow b\bar{b}$ with subsequent semileptonic decay either directly, $b \rightarrow \mu^-$ ($\bar{b} \rightarrow \mu^+$), or by the cascade decay, $b \rightarrow c \rightarrow \mu^+$ ($\bar{b} \rightarrow \bar{c} \rightarrow \mu^-$). (The expression $b \rightarrow \mu^-$ is used for the process $B \rightarrow X\mu^-\overline{\nu}_\mu$, where B is the b flavor hadron. The other expressions follow this notation.) It also contained additional prompt muons coming from $e^+e^- \rightarrow c\bar{c}$, followed by $c \rightarrow \mu^+$ ($\bar{c} \rightarrow \mu^-$), as well as non prompt muons from decay and non prompt muons. For the determination of A_b, the forward-backward charge asymmetry in $e^+e^- \rightarrow b\bar{b}$ and R_b, the ratio of the production cross-section of $e^+e^- \rightarrow b\bar{b}$ to the theorectical QED expectation for $e^+e^- \rightarrow \mu^+\mu^-$, it was assumed that the yield and asymmetry of $e^+e^- \rightarrow c\bar{c}$ was correctly described by the standard model.

The c quark form a doublet with the s quark with properties that are well established. Whereas, since the t quark has not been observed experimentally, the same cannot be said of the (t,b) doublet. An alternate method of measuring A_b without any assumptions about the cross section and asymmetry of $e^+e^- \rightarrow c\bar{c}$ is described in chapter 6. The five free parameters fitting method to obtain A_b, R_b, A_c, R_c and non-prompt muons simultaneously discussed in that chapter requires more data than presently available. The estimated contributions from $c\bar{c}$ production and from non-prompt muons were determined by using a Monte Carlo simulation, where five flavors were generated according to the standard model using the LUND 6.3 event generator [47]. These contributions were subtracted from the inclusive muon data in order to obtain the $e^+e^- \rightarrow b\bar{b}$ sample. Estimation of the fraction of non prompt muons coming from b flavored hadrons requires an assumption of $e^+e^- \rightarrow b\bar{b}$ cross-section and asymmetry which this analysis attempts to measure and these quantities were assumed to be given by the standard model. Although such an assumption is not strictly valid, it does not seriously affect the analysis because this fraction depends mostly on the decay kinematics of the b quark and the total number of non prompt muons coming from the b flavor hadrons was only about 1/10 of those originating from u,d,s, and c flavor hadrons. The Monte Carlo was also used for estimating the ratio of muons from $b\bar{b}$ cascade decays to those from direct decays. This ratio depends only on the decay kinematics of the b quark and not on the dynamics of $b\bar{b}$ pair production. Cascade decays produce muons

with charge opposite to those produced by direct decay and hence have the opposite asymmetry. This effect was corrected during the unfolding of the data described in section 5.2.

The angle between the outgoing b quark and the incoming e^- beam directions is referred to as θ (see figure 5.1a). In practice, it is not possible to find the $b\bar{b}$ quark direction. θ is therefore approximated by the angle made by the thrust axis and beam direction. The thrust, T, is defined as

$$T = \max_{\mathbf{t}} \frac{\sum_{i=1}^{N} |\mathbf{t}.\mathbf{p}_i|}{\sum_{i=1}^{N} |\mathbf{p}_i|} \tag{5.1}$$

where the $\mathbf{p}_i$'s are the momenta of the "good" CDC and SHC particles (see section 4.1). The unit vector $\mathbf{t}$ is chosen to maximize the thrust. In an ideal situation, the thrust axis would be the same as the initial $b\bar{b}$ quark axis. However, one still needs to know the direction of the b quark. This information is inferred from the charge and location of the prompt muon as follows: The particles are divided into two hemispheres by the plane perpendicular to the thrust axis. The hemisphere that contains the $\mu^-(\mu^+)$ is associated with the $b(\bar{b})$ quark and the angle θ is the angle made by the thrust axis in this hemisphere and the incoming $e^-(e^+)$ direction (see figure 5.1b). The thrust axis is a poor measure of the b-quark axis if many of the particles are missing. This can happen because of the limited geometrical acceptance of the CDC and SHC ($|\cos\theta| < 0.85$ and $|\cos\theta| < 0.73$ respectively). An angular cut of $|\cos\theta| < 0.60$ was therefore applied to the data. Figure 5.2 shows the good agreement between the the thrust distribution of the multihadronic events

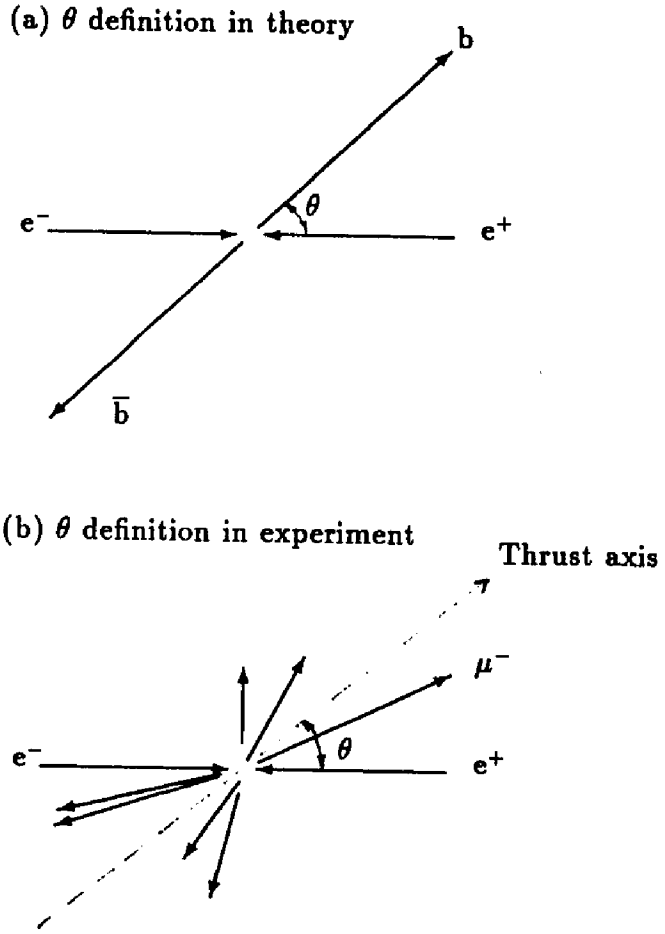

Figure 5.1: Definition of forward-backward direction

for the 52 GeV to 61.4 GeV data sample compared with the thrust distribution of Monte Carlo simulated events normalized to the same luminosity of 33.3 pb^{-1}. Figure 5.3 shows that difference in $\cos\theta$ for the b quark axis and the thrust axis for the Monte Carlo simulted events [48]. The results indicate that the difference is less than $\cos\theta = 0.10$ at 90% confidence level.

5.1 Enrichment of the $b \rightarrow \mu$ fraction

Semileptonic decays of heavy quarks ($b \rightarrow c\mu^-\bar{\nu}_\mu$, $c \rightarrow s\mu^+\nu_\mu$) lead to prompt muons with large transverse momentum (P_T) with respect to the event thrust axis. The average P_T of the prompt muon from a c quark generally is not as high as that from a b quark, reflecting the heavier mass of mesons with b-quark flavor. An enrichment of b-quark events is thereby obtained by selecting multihadronic events with high P_T muons.

The distribution for muon P_T for the data is shown in figure 5.4 together with the estimated contributions of $c\bar{c}$, non prompt muons and $b\bar{b}$. Figure 5.4 shows that the fraction of events from $b\bar{b}$ can be increased by making a P_T cut (eliminating events below a specified P_T). However beyond a certain muon P_T (around 1.5 GeV/c) the rate of rejecting $b \rightarrow \mu$ events would become bigger than the rate of rejecting background. Thus the data sample can be enriched with b-quark events by applying a suitable muon P_T cut. A study using Monte Carlo simulated events indicated that the statistical and systematic errors for A_b were minimized by a cut

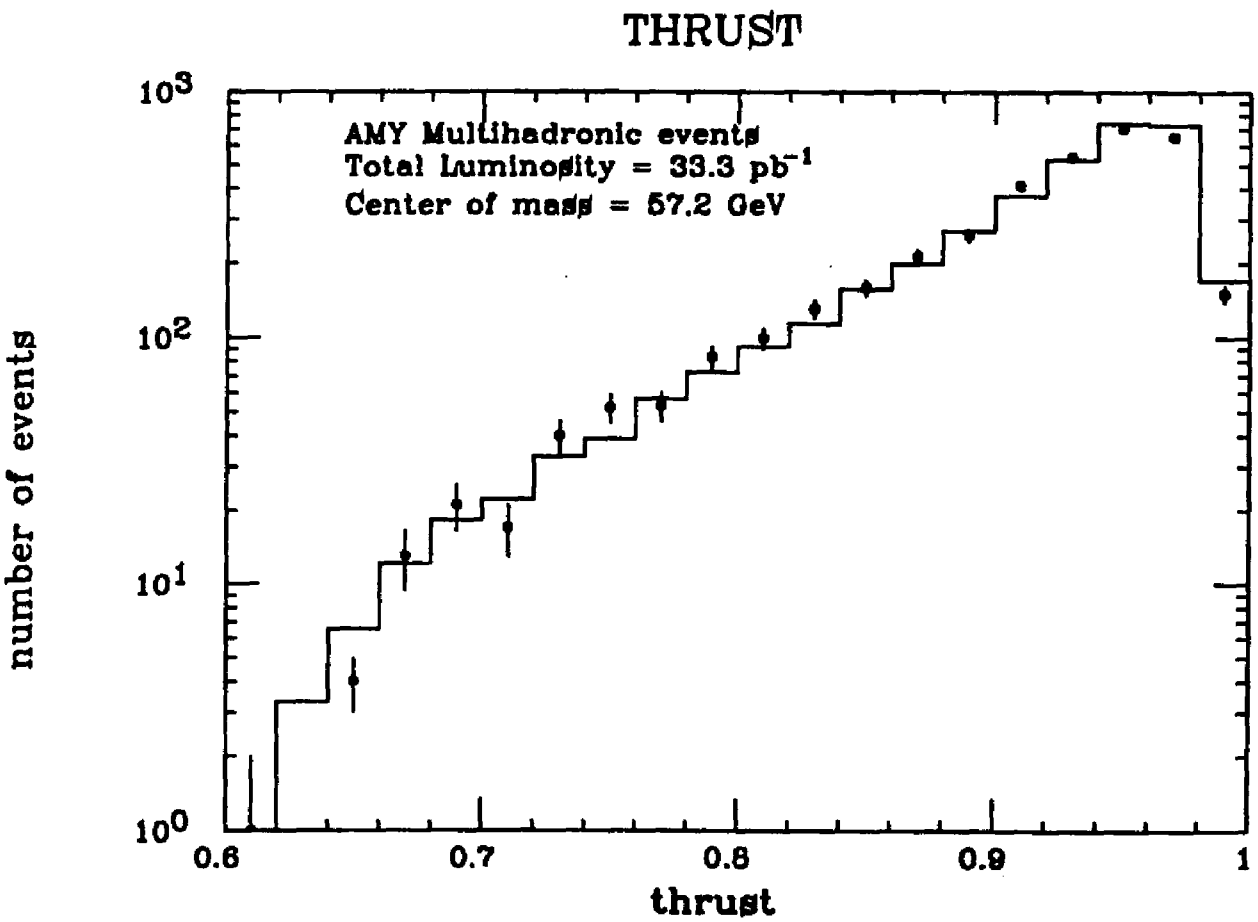

Figure 5.2: Thrust distribution for data and Monte Carlo simulated events

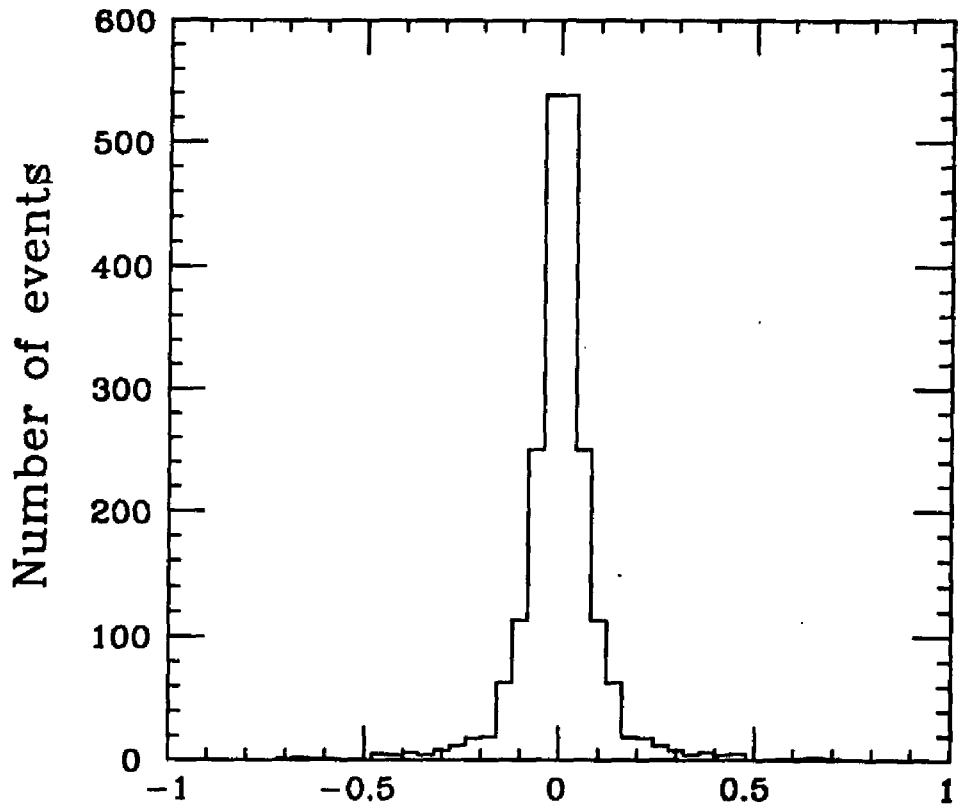

Figure 5.3: $\Delta\cos\theta$: The difference between $\cos\theta$ of b quark axis and thrust axis as determined by Monte Carlo simulated events

of 0.7 GeV/c on the muon P_T (figure 5.5). Hence the A_b and R_b were extracted from the distributions for $P_T \geq 0.7$ GeV/c. For events with muon $P_T \geq 0.7$ GeV/c, the non prompt muons were estimated to be about 25% of the inclusive muon data sample [see table 4.7]. About 50% of the non prompt muons were from punchthrough and the remainder from decays.

The distributions for $\cos\theta$ of the data and the expected background as determined by Monte Carlo are shown in figure 5.6. The angle θ used in figure 5.6 is defined as the direction of the thrust axis associated with $\mu^-(\mu^+)$ with respect to the incoming $e^-(e^+)$ direction. As expected, the angular distribution for non prompt muons does not show any asymmetry, while the $c\bar{c}$ contribution has a positive asymmetry. Actually $e^+e^- \rightarrow c\bar{c}$ also has a negative asymmetry. The positive asymmetry observed for $e^+e^- \rightarrow c\bar{c}$ is due to the convention of tagging the c-quark with a μ^- (remember $b \rightarrow \mu^-$ but $c \rightarrow \mu^+$).

5.2 The Unfolding Factor

After subtracting $c\bar{c}$ and non prompt muons from the data sample, the resulting distribution was unfolded to give the corrected $e^+e^- \rightarrow b\bar{b}$ differential cross-section. Monte Carlo simulation studies show that about 19% of $e^+e^- \rightarrow b\bar{b}$ events produce prompt muons with $P_T \geq 0.7$ GeV/c that are detected by AMY within $|\cos\theta| \leq 0.6$. This 19% includes the average efficiency for detecting the b quark from inclusive

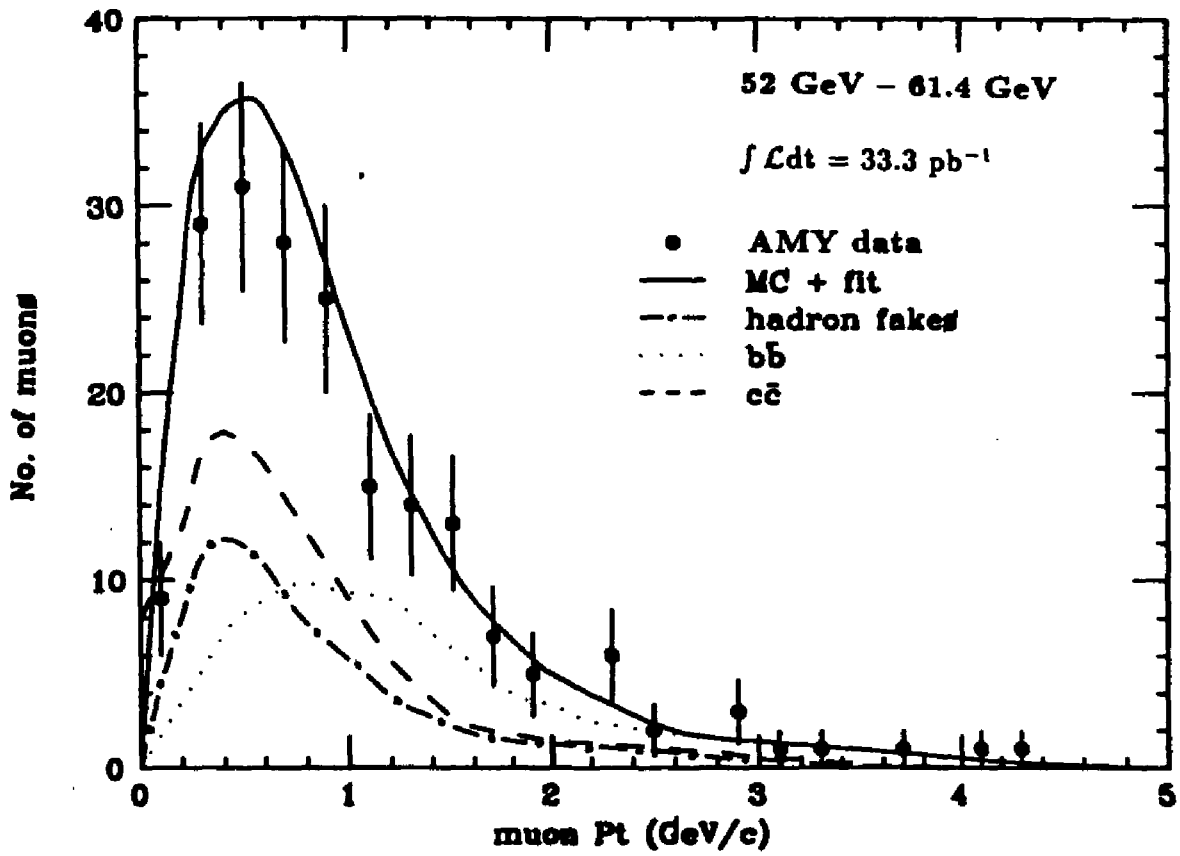

Figure 5.4: P_T distributions for data and Monte Carlo expectation

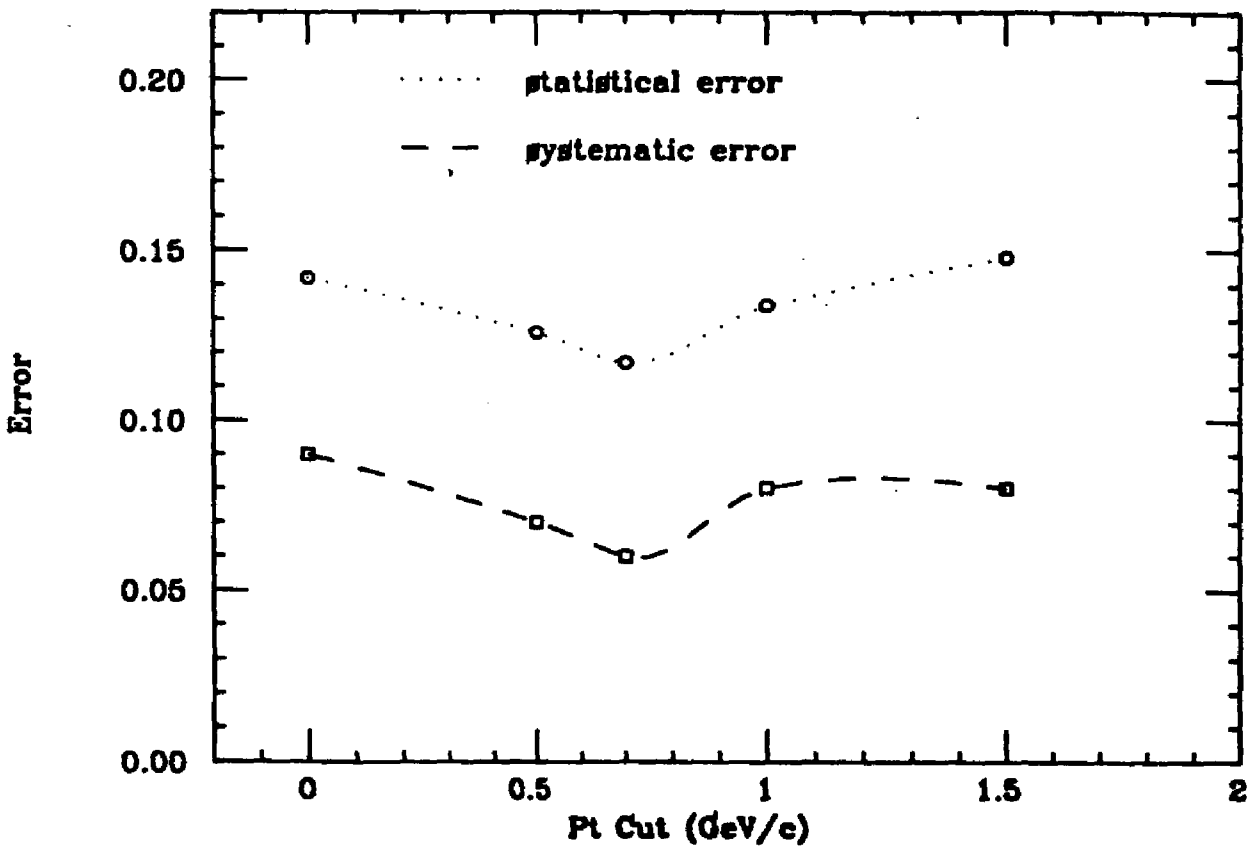

Figure 5.5: Errors on A_b as a function of P_T cuts from a study using Monte Carlo simulated events

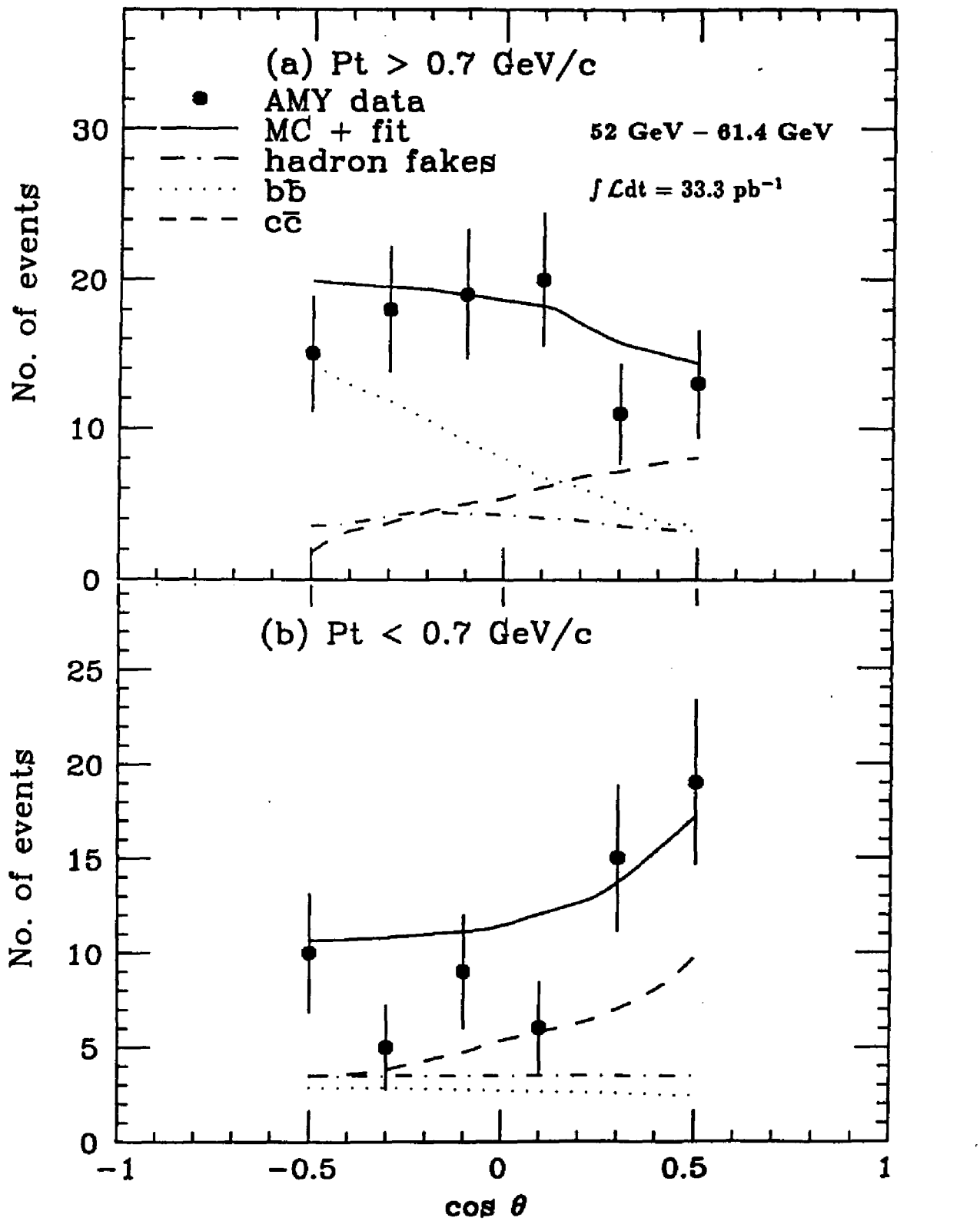

Figure 5.6: cosθ distributions for data and Monte Carlo

muon events and the muon detection effeciency of 82%. A simple way to unfold the data is by multiplying the number of events in each cosθ bin by a factor of 1/0.19. By doing this an asymmetry, $A_b = -0.66 \pm 0.36$ is obtained, consistent (within errors) with the standard model prediction of -0.58.

However this simple way of unfolding the data does not account for: 1) the effect of different θ definitions; i.e. the theoretical (generated) angle θ was defined by the b quark axis while the detected event angle θ was defined by the thrust axis and; 2) the effect of the cascade decay $b \rightarrow c \rightarrow \mu$. A more sophisticated unfolding factor was obtained by dividing a Monte Carlo generated $e^+e^- \rightarrow b\bar{b}$ angular distribution by an angular distribution of simulated $b\bar{b}$ events with a detected prompt muon. The unfolding factor is a function of cosθ given by

Unfolding factor (cosθ)

$$= \frac{\text{Total number of } e^+e^- \rightarrow b\bar{b} \text{ events } (\cos\theta)}{\text{Number of } b \rightarrow \mu \ (\cos\theta) \text{ and } b \rightarrow c \rightarrow \mu \ (\cos\theta)} \qquad (5.2)$$

The unfolding factor thus obtained is biased because the Monte Carlo simulated events that were used have the standard model predicted value for the $e^+e^- \rightarrow b\bar{b}$ charge asymmetry built into it. However, this is justified in the present case because the measurement made by a simple unfolding factor of 1/0.19 described above already show an asymmetry for $e^+e^- \rightarrow b\bar{b}$ that is consistent with the standard model prediction.

Figure 5.7 show the Monte Carlo generated and simulated cosθ distribution for $P_t \geq 0.7$ GeV/c of the (a) total number of $e^+e^- \rightarrow b\bar{b}$, (b) observed number of

$b \rightarrow \mu$ and (c) observed number of $b \rightarrow c \rightarrow \mu$ events.

The unfolding factor is shown in figure 5.8. This unfolding factor has an asymmetry due to the contribution from the cascade $b \rightarrow c \rightarrow \mu$ events, where a muon generated in a $\cos\theta$ bin is observed in the negative $\cos\theta$ bin.

5.3 Systematic Errors

There are two broad categories of systematic errors in this analysis arising from:

1. The detector and data analysis
   (a) luminosity measurement (3.3%)
   (b) trigger inefficiencies (0.3%)
   (c) detector acceptance (2%)
   (d) data recording failure (0.2%)
   (e) CDC calibration/reconstruction (0.8%)
   (f) background to multihadronic events from $\tau\tau$, two photons and beam gas (0.3%)
   (g) MUO inefficiency ($< 2\%$)
   (h) selecting $e^+e^- \rightarrow b\bar{b}$, $c\bar{c}$ events by requiring a muon ($< 1\%$).
2. The Monte Carlo simulated events to estimate data for
   (a) non-prompt background: punchthrough and muons from decay of pions and kaons (8%)

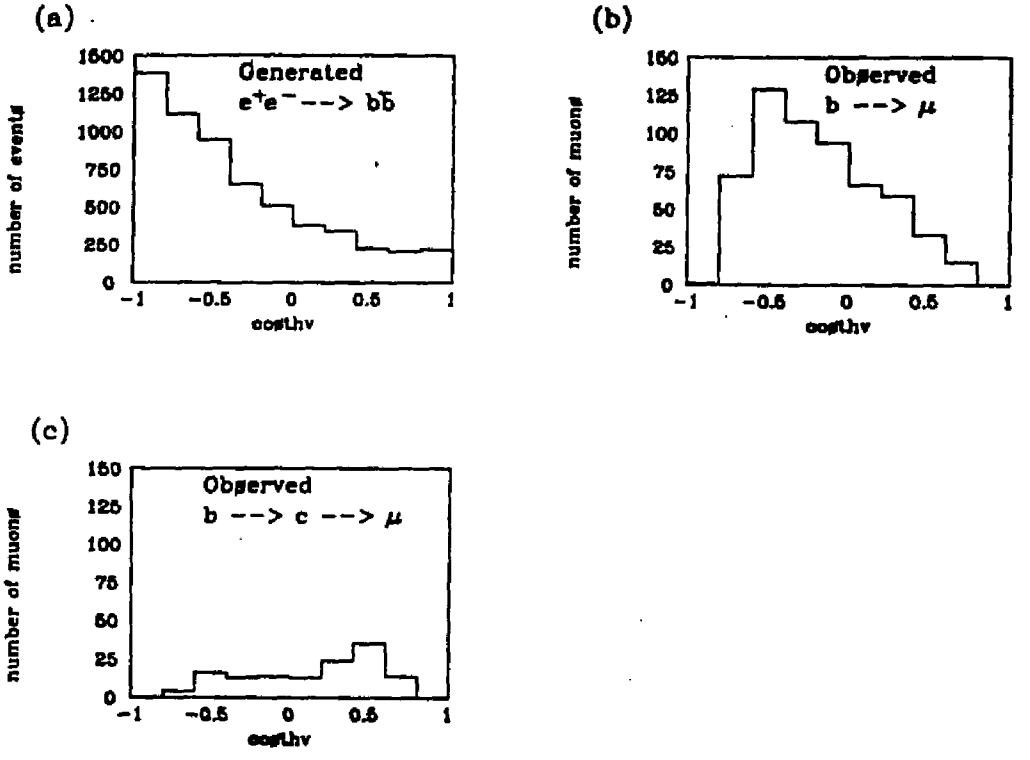

Figure 5.7: Monte carlo generated and simulated $\cos\theta$ distribution

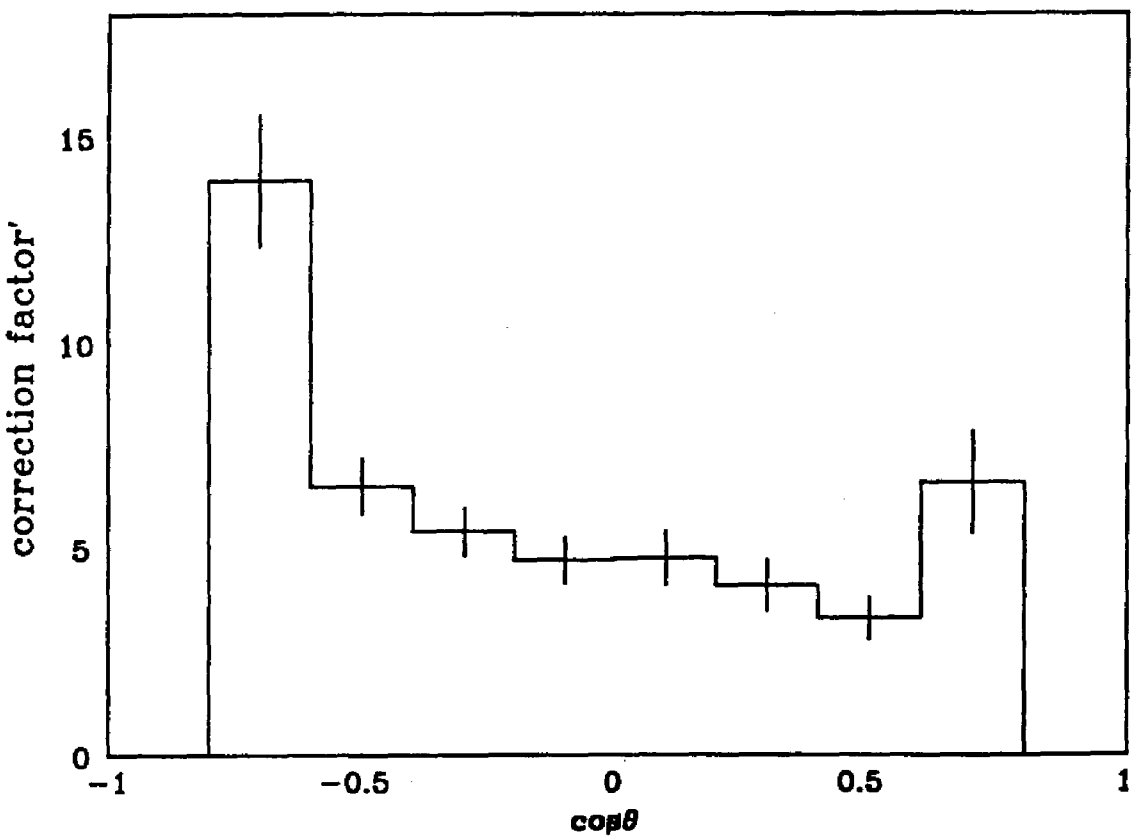

Figure 5.8: Unfolding factor for $P_T \geq 0.7$ GeV data; determined by Monte Carlo simulated events

(b) thrust axis angle calculation and smearing of θ by using thrust axis angle instead of b quark axis ($\sim$ 0%).

3. Cross section and asymmetry of $e^+e^- \rightarrow c\bar{c}$ (assumed standard model, 0%).

The systematic errors from the detector and data analysis (1a to 1f) have been studied in detail (see reference [49]). Together with the MUO inefficiencies (see section 4.4), this type of systematic error adds up to 4.5%.

Figure 4.4 shows that the RDIF distribution of the Monte Carlo simulted events closely resembles that for inclusive muons, indicating that the efficiency for selecting prompt muons as determined by the Monte Carlo simulated events must also be close to that for data, giving a very small systematic error.

The main systematic uncertainty from the Monte Carlo simulated events was from the non-prompt background. Pion punchthrough is well understood since there are data that can be compared to the results of the Monte Carlo simulation[50]. As discussed in section 4.3.2, the Monte Carlo systematically overestimated pion punchthrough by a factor of two, hence the contribution for punchthrough as obtained by the Monte Carlo simulation was halved. There are no data for kaon punchthrough in the TRISTAN energy range. This was estimated from Monte Carlo studies to cause approximately half of the punchthroughs, mainly because of the smaller absorption cross section for kaons in iron. The Monte Carlo event generator is in good agreement with measured results for the pion:kaon:proton ratio

[51] so estimates of the decay background are reliable. The selectión of $e^+e^- \rightarrow b\bar{b}$ events by requiring a muon depends only on the decay kinematics of the b quark and not on the dynamics of the $b\bar{b}$ pair production and the Monte Carlo simulation is therefore expected to be reliable. The systematic uncertainty from the non-prompt background was taken to be 30% of the total non-prompt events. At a P_T cut of 0.7 GeV/c, this contributes to 8% of the multihadronic inclusive muon data sample (see table 4.7). Figure 5.2 shows the good agreement between the data and Monte Carlo simulated events for the thrust distribution of multihadronic events and figure 5.3 shows that difference in $\cos\theta$ for the b quark axis and the thrust axis is small. Also, this smearing was corrected for in the unfolding factor. Overall, the systematic error for 2(b) is therefore very small.

The systematic errors for A_b and R_b are obtained by repeating the analysis with the non-prompt contribution varied by $\pm 30\%$ (corresponding to 8% of data sample) and the systematic errors of the data sample by $\pm 4.5\%$. The largest of the resulting shifts in A_b and R_b are used as estimates for the systematic errors.

5.4 Results

5.4.1 Obtaining A_b and R_b using minimum χ^2 fit

After subtracting $c\bar{c}$ and non-prompt backgrounds from the data sample, the resulting distribution was unfolded to give the corrected $e^+e^- \rightarrow b\bar{b}$ differential cross-

section. This was then fit to equation (2.55) with two free parameters (ie. A_b and R_b) over the angular range of $|\cos\theta| \leq 0.6$, allowing A_b and R_b to vary. The fit was accomplished using the Minuit χ^2 program from the CERN Computer Center Program Library for function minimization and error analysis. This program finds the values of R_b and A_b, such that χ^2 is a minimum, where

$$\chi^2 = \sum_{\cos\theta_i} \left(\frac{X_i - \overline{X}_i}{\sigma_{X_i}} \right)^2 . \tag{5.3}$$

Here X_i is the value of the differential cross-section for $\cos\theta_i$ and $\overline{X}_i$ the expected value obtained from equation (2.55) for particular values of R_b and A_b. σ_{X_i} is the standard deviation of X_i, including errors from data and Monte Carlo.

The results obtained for various P_T cuts at an average center-of-mass energy of $\sqrt{s}$=57.2 GeV, are given in table 5.1. The results agree with each other within errors for the different P_T cuts. The optimal P_T cut for minimizing the statistical and systematic errors as obtained using Monte Carlo simulated data is 0.7 GeV (see section 5.1). This is consistent with the results shown in table 5.1.

The final results are

$$A_b = -0.82 \pm 0.25 \pm 0.14 \text{ and}$$

$$R_b = 0.47 \pm 0.12 \pm 0.12,$$

where the errors are "statistical" and "systematic" respectively. The "statistical" error includes the statistical errors of the Monte Carlo as well as data. It also contains the errors in the unfolding factor. The results of the fit are shown in

	R_b	A_b	χ^2/d.o.f.
0.0	$0.35 \pm 0.12 \pm 0.20$	$-0.78 \pm 0.33 \pm 0.14$	0.33
0.5	$0.45 \pm 0.12 \pm 0.15$	$-0.68 \pm 0.28 \pm 0.14$	0.36
0.7	$0.47 \pm 0.12 \pm 0.12$	$-0.82 \pm 0.25 \pm 0.14$	0.43
1.0	$0.47 \pm 0.13 \pm 0.10$	$-0.90 \pm 0.31 \pm 0.16$	0.84
1.5	$0.49 \pm 0.17 \pm 0.07$	$-0.99 \pm 0.33 \pm 0.10$	1.17

Table 5.1: R_b and A_b for various P_T cuts

figure 5.9. No corrections were made for $B^0 - \overline{B}^0$ mixing. The measured results are consistent with the standard model prediction of $A_b = -0.58$ and $R_b = 0.56$.

Figure 5.10 compares the result for A_b with measurements by other experiments [53] which were also not corrected for the effects of $B^0 - \overline{B}^0$ mixing. Figure 5.11 shows the results for R_b compared with the standard electroweak prediction including QCD effects.

Since A_b and R_b are functions of the center-of-mass energies ($\sqrt{s}$), it would be interesting to see the results if the data were divided into two samples, with each sample having a smaller spread in $\sqrt{s}$: 52 GeV $\leq \sqrt{s} \leq$ 57 GeV with an integrated luminosity of 18.6 pb^{-1} and 57.25 GeV $\leq \sqrt{s} \leq$ 61.8 GeV with an integrated luminosity of 14.7 pb^{-1}. Using the same analysis procedures, the extracted A_b and R_b, at an average $\sqrt{s}$ of 55.2 GeV were

$$A_b = -0.72 \pm 0.28 \pm 0.14 \text{ and } R_b = 0.57 \pm 0.16 \pm 0.15.$$

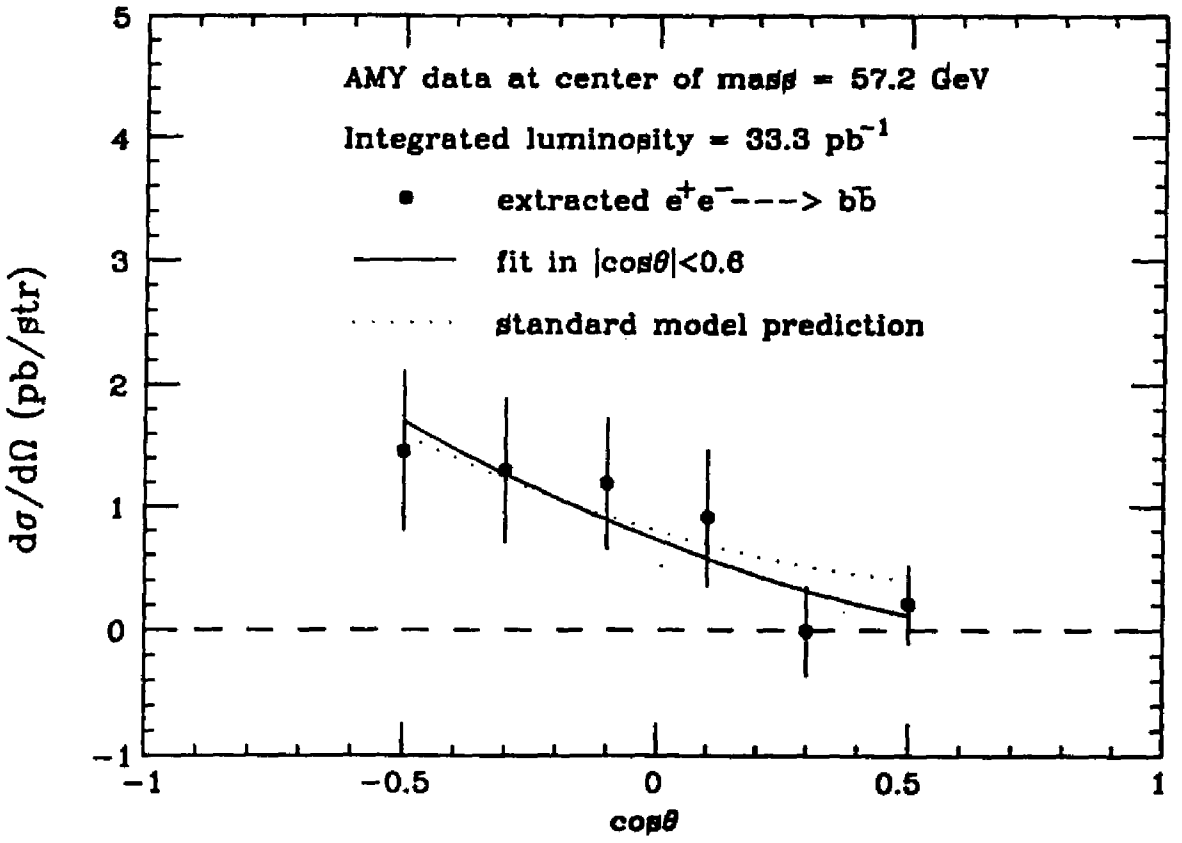

Figure 5.9: Results of fitting for A_b and R_b

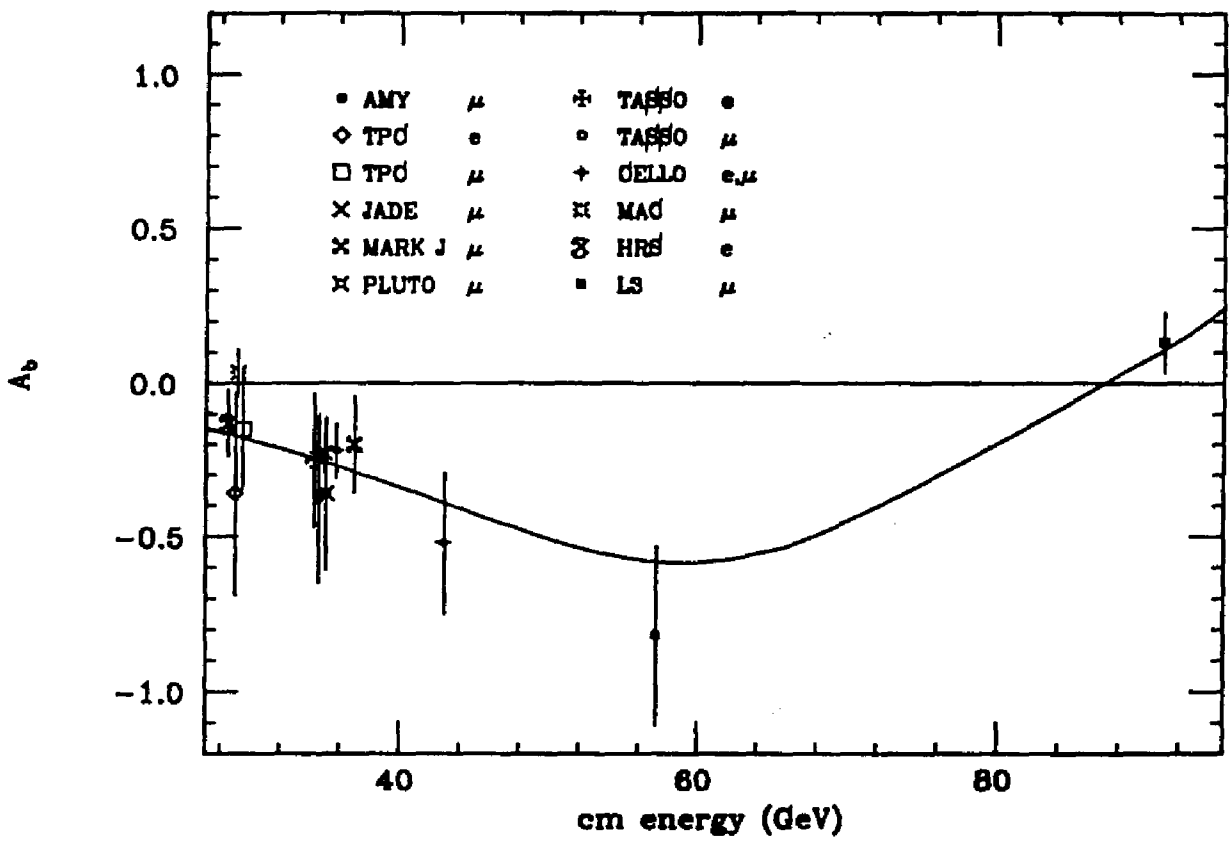

Figure 5.10: Results for A_b

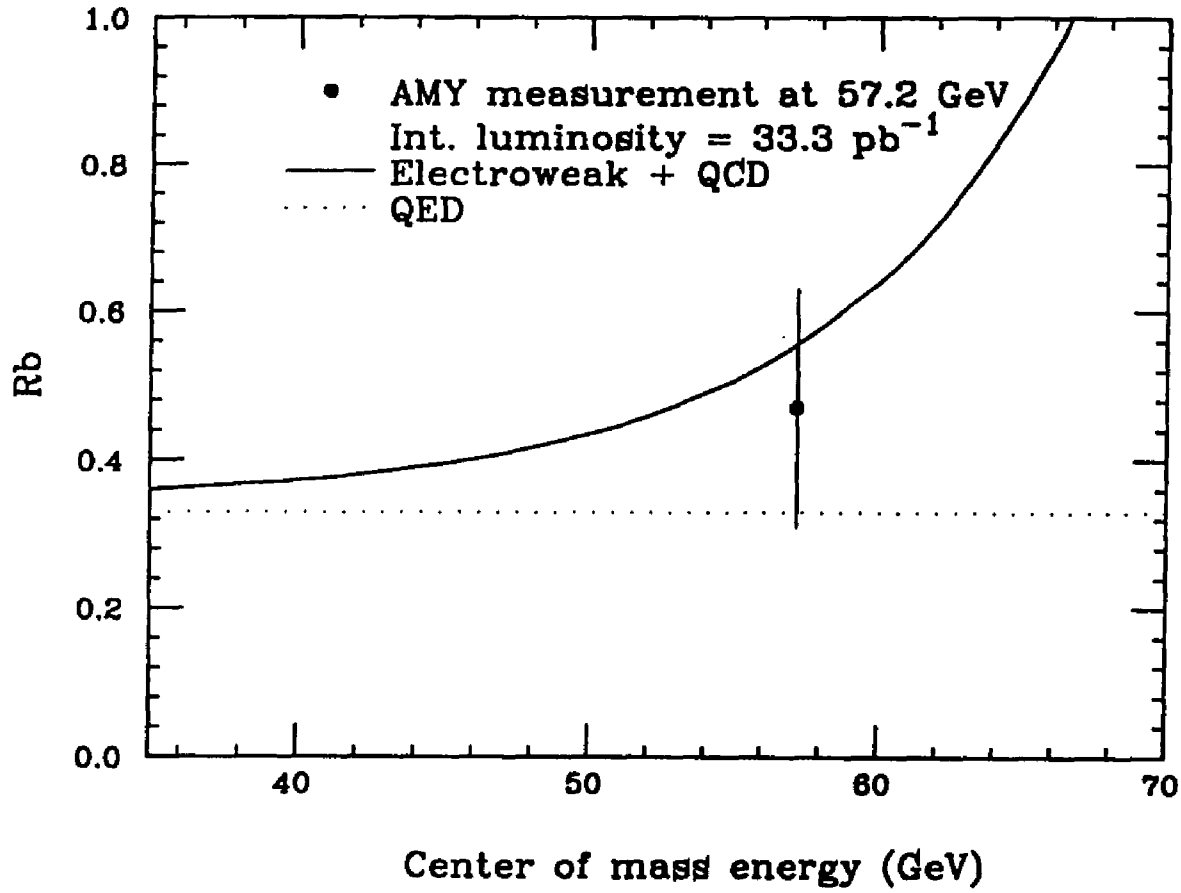

Figure 5.11: Results for R_b

The standard model predictions are $R_b = 0.50$ and $A_b = -0.56$. A_b and R_b at average $\sqrt{s}$ of 60.3 GeV were

$$A_b = -1.04 \pm 0.62 \pm 0.55 \text{ and } R_b = 0.26 \pm 0.15 \pm 0.11.$$

The standard model predictions are $R_b = 0.64$ and $A_b = -0.58$.

5.4.2 A_b and R_b from formulae

R_b can be calculated from the $e^+e^- \rightarrow b\bar{b}$ cross-section by integrating equation (2.55) over the angular acceptance,

$$\int_{0.6}^{-0.6} \frac{d\sigma}{d\cos\theta} = \frac{\pi\alpha^2}{2s} R_b \int_{-0.6}^{0.6} \left(1 + \cos^2\theta + \frac{8}{3} A_b \cos\theta\right) d\cos\theta \qquad (5.4)$$

giving

$$\sigma\Big|_{-0.6}^{0.6} (\text{pb}) = 1.344 \frac{\pi\alpha^2}{2s} R_b(\text{GeV}^{-2}). \qquad (5.5)$$

Similarly, A_b can be calculated from

$$\frac{\sigma_F - \sigma_B}{\sigma_F + \sigma_B}\Big|_{\cos\theta=-0.6}^{\cos\theta=0.6} = \frac{\int_{0.0}^{0.6} \frac{d\sigma}{d\cos\theta} d\cos\theta - \int_{-0.6}^{0.0} \frac{d\sigma}{d\cos\theta} d\cos\theta}{\int_{0.0}^{0.6} \frac{d\sigma}{d\cos\theta} d\cos\theta + \int_{-0.6}^{0.0} \frac{d\sigma}{d\cos\theta} d\cos\theta} = 1.4 A_b \qquad (5.6)$$

The results for R_b and A_b obtained by hand calculation using equation (5.5) and (5.6) is compared with that using the minimum χ^2 fitting method in table 5.2.

The results for A_b and R_b as obtained by the hand calculation and minimum χ^2 fitting methods agree very well for the 52 to 57 GeV and 52 to 61.4 GeV data samples. This indicates that the minimum χ^2 fitting with two free parameters is valid for these two sets of data sample. R_b as obtained by equation (5.5) is reliable since it is obtained from a simple counting the number of $e^+e^- \rightarrow b\bar{b}$ events

	$\sqrt{s}$ (GeV)	Calculation	χ^2 fit
R_b	55.2	$0.58 \pm 0.16 \pm 0.12$	$0.57 \pm 0.16 \pm 0.10$
	57.2	$0.50 \pm 0.12 \pm 0.12$	$0.47 \pm 0.12 \pm 0.12$
	60.3	$0.40 \pm 0.17 \pm 0.13$	$0.26 \pm 0.15 \pm 0.11$
A_b	55.2	$-0.77 \pm 0.35 \pm 0.15$	$-0.72 \pm 0.28 \pm 0.14$
	57.2	$-0.75 \pm 0.32 \pm 0.20$	$-0.82 \pm 0.25 \pm 0.14$
	60.3	$-0.71 \pm 0.59 \pm 0.33$	$-1.04 \pm 0.62 \pm 0.55$

Table 5.2: Comparison of R_b and A_b using hand calculation and minimum χ^2 fitting (obtained from unfolding the background subtracted inclusive muon events). The discrepancies in the values of R_b for the scan to 61.4 GeV data sample as obtained by the hand calculated and minimum χ^2 fitting methods would therefore indicate the break down of the minimum χ^2 method for this data sample. This can be understood from the fact the number of events in each $\cos\theta$ bin (figure 5.12) for the scan to 61.4 GeV data sample is small, making the differential cross-section distribution sensitive to statistical fluctuations. Indeed, the $d\sigma/d\Omega$ distribution for this data sample (figure 5.13) has two negative bins which is unphysical. The effect of the negative bins in the forward region tend to increase the asymmetry, thereby giving an unphysical $A_b = -1.04$ measured value. A_b by definition must be $|A_b| \leq 1$.

The proper way to resolve the problem in the scan - 61.4 GeV data sample is

to use the value of $R_b = 0.40$ obtained by hand calculation from equation 5.5. A_b is then obtained by the minimum χ^2 fit with one free parameter (ie. A_b). Doing this gives

$$A_b = -0.86 \pm 0.38 \pm 0.06 \tag{5.7}$$

with a χ^2/d.o.f. of 0.98.

5.4.3 Final Results

The final results are summarized in table 5.3.

average $\sqrt{s}$ (GeV)	R_b	A_b
55.2	$0.57 \pm 0.16 \pm 0.15$	$-0.72 \pm 0.28 \pm 0.14$
57.2	$0.47 \pm 0.12 \pm 0.12$	$-0.82 \pm 0.25 \pm 0.14$
60.3	$0.40 \pm 0.17 \pm 0.13$ (calculated value)	$-0.86 \pm 0.38 \pm 0.06$

Table 5.3: Final Results for R_b and A_b

5.5 Limit on $B^0 - \overline{B}^0$ mixing

Using equation (2.65) with a measured asymmetry of $A_b^{obs} = -0.82 \pm 0.29$ (the statistical and systematic errors are added in quaduture) and the standard model

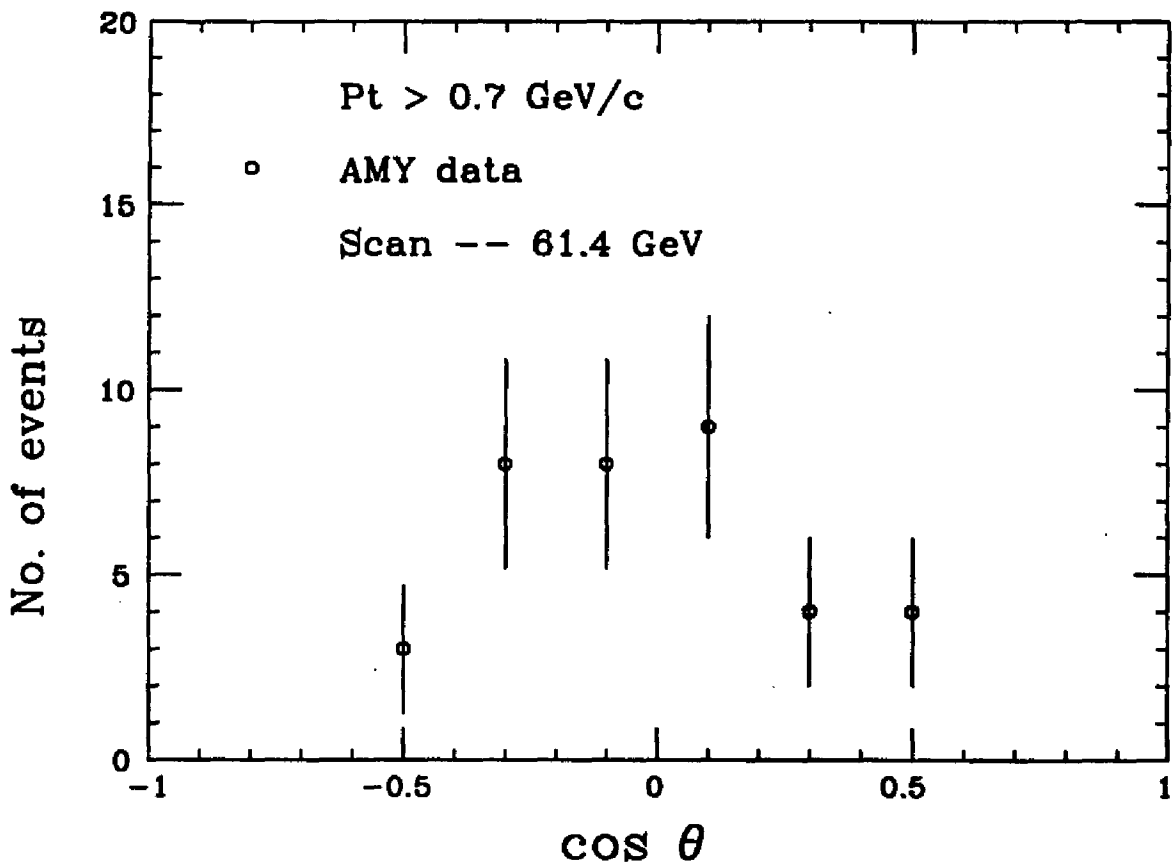

Figure 5.12: cosθ distribution for scan – 61.4 GeV data

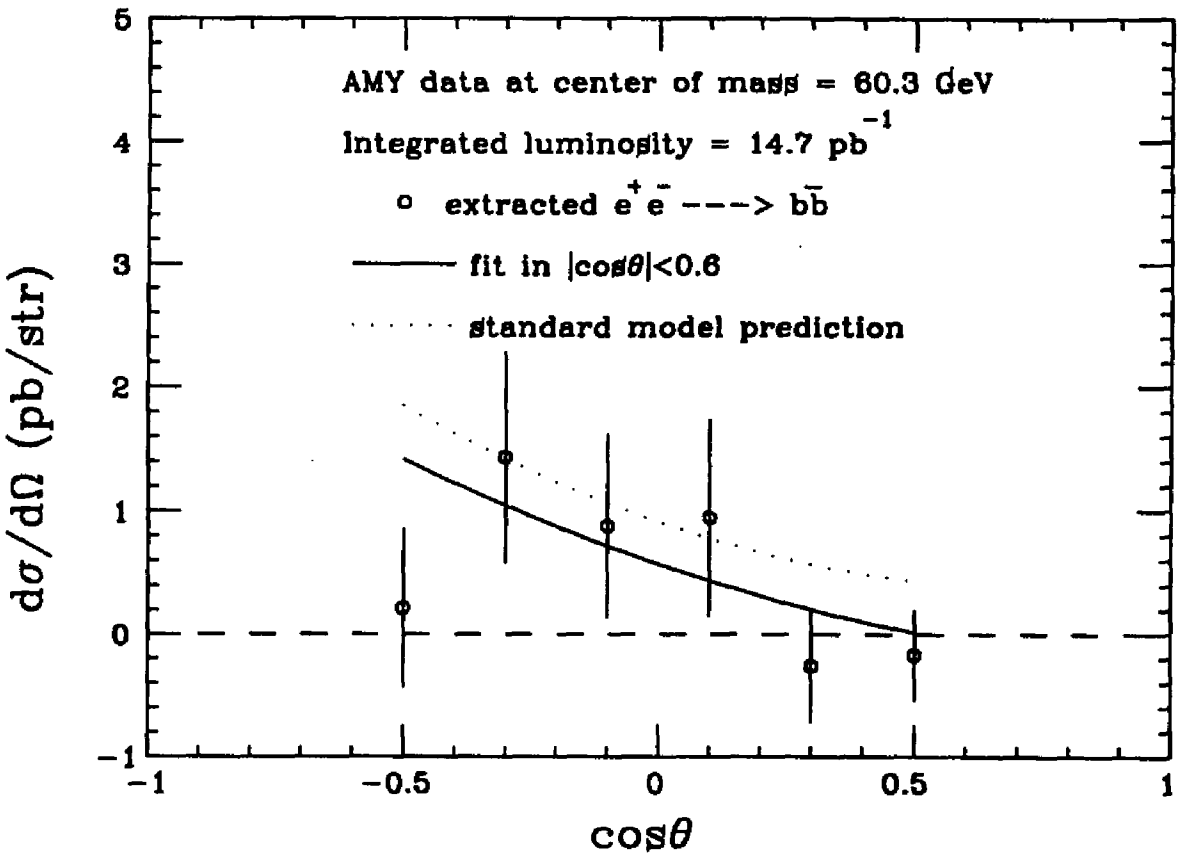

Figure 5.13: Minimum χ^2 fitting for scan – 61.4 GeV data

prediction of $A_b = -0.58$, the $B^0 - \overline{B}$ mixing parameter was deduced to be

$$\chi = -0.21 \pm 0.25. \tag{5.8}$$

Since $0 \leq \chi \leq 0.5$, this result indicate that there is not enough data to see any significant effect from $B^0 - \overline{B}^0$ mixing. However, a limit of $\chi < 0.20$ at 90% confidence level can be set. Figure 5.14 compares the $B^0 - \overline{B}^0$ mixing limit set by AMY with other experiments [54]. The plot for χ is determined using the simple assumption for average $\chi = \frac{3}{7}\chi_d + \frac{1}{1}\chi_s$ as described in section 2.6.

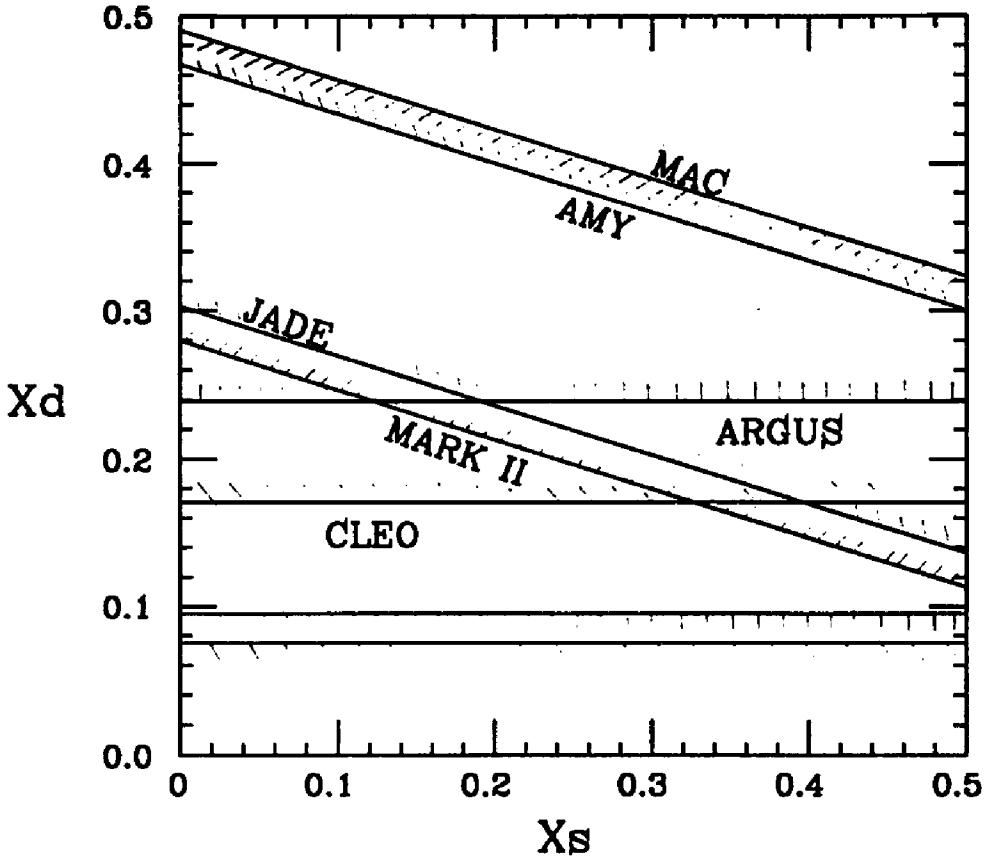

Figure 5.14: Results of $B^0 - \overline{B}^0$ mixing parameter

Chapter 6

Future measurements

From the first day of data taking in early 1987 until the spring of 1989, TRISTAN was the highest energy e^+e^- collider in the world, and thus the energy was increased at every opportunity in the quest for the discovery of new particles and physics.

Now that the battle for the highest energy has clearly been lost to SLC and LEP, TRISTAN can concentrate on achieving the highest possible luminosity by using micro-beta insertations [55]. The resulting increase in data will improve on all the measurements made by AMY. In the run period from February 1990 to July 1990, AMY expects to accumulate another 30 pb^{-1} of data at 60 GeV.

With the expected high statistics from the future runs, it will be possible to measure the relative cross-section and asymmetry for $e^+e^- \rightarrow b\bar{b}$, R_b and A_b , and for the $e^+e^- \rightarrow c\bar{c}$, R_c and A_c , using the matrix transformation method described in this chapter.

6.1 Matrix transformation method

In this method, the angular distribution of the inclusive muon events is fitted to an expected distribution with five free parameters and matrix elements which contain the information about the transformation between the ratio of the observed inclusive muons and the actual quarks which produced them. The five free parameters used are R_b , A_b , R_c , A_c and the yield of the hadron fakes, R_h, from all the five flavors; u, d, s, c and b.

The observed number of events in the i-th $\cos\theta$ bin, $N(\cos\theta_i)$ can be expressed as follows:

$$N(\cos\theta_i) = \sum_j [M_c(ij)R_cN_c(j) + M_b(ij)R_bN_b(j) + M_h(ij)R_hN_h(j)] \qquad (6.1)$$

where $N_f = \frac{\pi\alpha^2}{2s}\ (1 + \cos^2\theta_j + \frac{8}{3}A_f\cos\theta_j)$ is the number of events in the j-th $\cos\theta$ bin from the orginal quark, expressed in terms of a cross-section of one unit of R. $\cos\theta_i$ on the left hand side is defined by the thrust axis direction and $\cos\theta_j$ on the right hand side is defined by the quark direction. The matrix element M(ij) is the ratio of the number of observed muons in the $\cos\theta_i$ bin that come from the quark that was produced in the $\cos\theta_j$ bin in the $e^+e^- \rightarrow q\bar{q}$ process. The matrix M therefore determines the transformation between the number of observed muons and the number of quarks that produced them. M(ij) can be calculated using the LUND 6.3 Monte Carlo and it contains information regarding the effects of:

1. Smearing in θ due to the different definition of θ.

2. Efficiency for detecting b and c quarks by requiring a muon.

3. Cascade decay of b $\rightarrow$ c $\rightarrow \mu$.

4. Muon detection efficiency.

5. Hadron fakes (non prompt muons).

$M_b(ij)$ and $M_c(ij)$ are the transformation matrix elements for the prompt muon sources b and c respectively. $M_h(ij)$ is for the hadron fakes from all five flavors. As a first approximation, we can assume A_h to be zero since hadron fakes do not retain the charge information of the original quarks.

This matrix transformation method was used on the data collected between center of mass energies of 52 GeV and 57 GeV. We used 12 data points in the Minuit chi square fit. Six of these data points came from data with $P_t < 0.7$ GeV/c and $|\cos\theta| < 0.6$ and the other six from data with $P_t \geq 0.7$ and $|\cos\theta| < 0.6$.

The results were

$A_c = -0.68 \pm 0.33$ $\qquad$ $R_c = 1.64 \pm 0.61$

$A_b = -1.10 \pm 0.64$ $\qquad$ $R_b = 0.68 \pm 0.23$

measured at an average energy of $\sqrt{s} = 55.2$ GeV. The χ^2 for this measurement was 0.82. The yield of the hadron fakes, R_h, was 0.01 ± 5.26. Only the statistical errors are shown here. Figure 6.1 shows the $d\sigma/d\cos\theta$ versus $\cos\theta$ distribution for the data and the fit.

These values are consistent with the standard model expection of

$A_c = -0.40$ $\qquad$ $R_c = 1.51$

$A_b = -0.56$ $R_b = 0.50$

An estimated luminosity of around 180 pb^{-1} is required, however, to reduce the error for A_b to around ± 0.2 — a value comparable with the errors obtained in chapter 5.

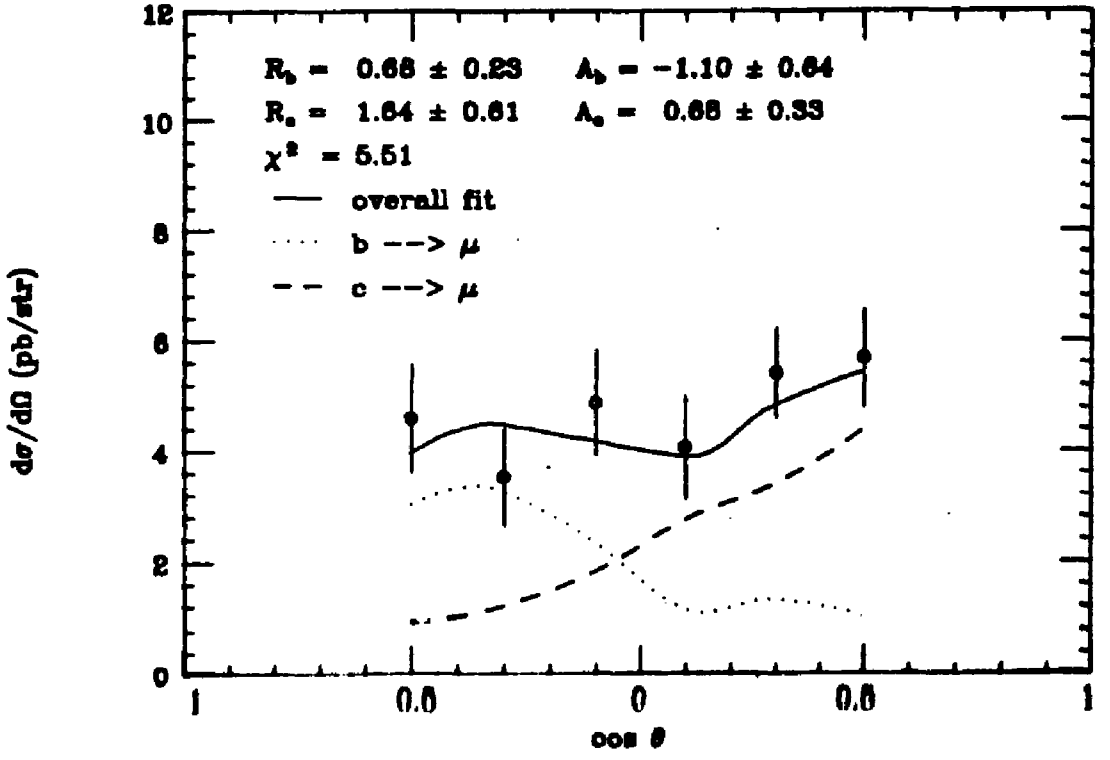

Figure 6.1: $d\sigma/dcos\theta$ versus $cos\theta$ distribution for matrix transformation fit to the 52GeV – 57GeV data

Chapter 7

Conclusion

The results for the $e^+e^- \rightarrow b\bar{b}$ cross section and forward-backward charge asymmetry using an integrated luminosity of 33.3 pb^{-1} at an average center of mass energy of 57.2 GeV are $R_b = 0.47 \pm 0.12 \pm 0.12$ and $A_b = -0.82 \pm 0.25 \pm 0.14$. These results are consistent with the standard model predictions of 0.56 and -0.58. The measurements of A_b are in fact consistent with the standard model prediction throughout the energy region explored so far. Thus the axial-vector coupling of the $b\bar{b}$ to the Z^0 is consistent with being $g_A^b = -1/2$. This in turn is consistent with the weak isospin asignments $T_{3L} = -1/2$ and $T_{3R} = 0$ for the b quark. The simple topless model discussed in section 2.5 predicts $A_b = 0.0$, hence the measurement rules out this model at greater than the 99% confidence level.

The main assumption for the analysis is that the yield and asymmetry for $e^+e^- \rightarrow c\bar{c}$ is correctly given by the standard model. With more data, it is possible

to measure A_b and R_b using the matrix element method described in chapter 6 without having to make such assumptions.

A_b and R_b measurements can also be obtained by using multihadronic inclusive electrons events, and this is now being done at AMY.

Using the measurement value of A_b, a limit on $B^0 - \overline{B}^0$ was set of $\chi < 0.20$ at 90% confidence level. This result is consistent with the 90% CL limits found by MARK II [56] ($\chi < 0.12$) and by JADE [57] ($\chi < 0.13$) but has poor agreement with the 95% CL limit found by MAC [58] ($\chi > 0.21$).

Bibliography

[1] W. Bartel *et.al.* (JADE), Phys. Lett. **B146**,437(1984); M. Althoff *et.al.* (TASSO), Phys. Lett. **B146**,443(1984); H.R. Band *et.al.* (MAC), Phys. Lett. **B218**,369(1989); S.L. Wu, Nucl. Phys. B (Proc. Suppl) **3**(1988).

[2] V. Barger and S. Pakvasa Phys. Lett. **B81**,195(1979).

[3] S.L. Glashow, Nucl. Phys. **22**,579(1961).

[4] S. Weinberg, Phys. Rev. Lett., **19**,1264(1967).

[5] A. Salam, Proceedings of the 8th Nobel Symposium, Aspenasgarden, p.367, Almqvist and Wiksell, Stockholm, 1968.

[6] F Halzen & A Martin, Quarks and Leptons, John Wiley & Sons, p. 335, 1984.

[7] Review of Particle Properties, Phys. Lett. **B204**p.51(1988).

[8] W.Celmaster and R.Gonsalves, Phys. Rev. Lett., **44**,560(1980).

[9] W.E. Caswell, Phys. Rev. Lett, **33**,244(1974).

[10] M.Dine and J.Sapirstein, Phys. Rev. Lett., **43**,668(1979).

[11] V. Barger and S. Pakvasa, Phys. Lett., **B81**,195(1979).

[12] K. Chadwick, Phys. Rev. Lett., **46**,88(1981).

[13] E. Ma, Phys. Rev. Lett., **57**,535(1986); E. Ma, Phys. Rev. D, **35**,851(1987).

[14] V. Barger Phys. Rev. D, **24**,1328(1981).

[15] E. Ma, Phys. Rev. D, **35**,851(1987).

[16] Y. Sakai *et.al.* (AMY), Phys. Lett. **B234**,534(1990).

[17] E. A. Paschos *et.al.* Phys. Lett. **B218**,240(1983); I. I. Bigi and A. I. Sanda, Phys. Rev. D **29**,1393(1984).

[18] M.Artuso *et.al.* (CLEO collab.), Phys. Rev. Lett. **62**(1989)2233.

[19] H.Albrecht *et.al.* (ARGUS), Phys. Lett. **B192**(1987)245.

[20] AMY Collaboration. TRISTAN Proposal for Study of e^+e^- Interactions with a High Luminosity, High Resolution Lepton Detector, TRISTAN-EXP-003, November 1984.

[21] TRISTAN Project Group, "TRISTAN Electron-Positron Colliding Beam Project", KEK Report 86-14(1987).

[22] Y. Fujii, *et.al.* X-Ray Detector, AMY Note 488.

[23] Review of Particle Properties, Phys. Lett. **B204**p.54(1988).

[24] Y. Doi *et.al.* "A 3 Tesla Super Conducting Magnet for the AMY Detector", Nucl. Instrum. Meth.,**A274**,95(1989).

[25] R. McNeil *et.al.* Progress Report on AMY Muon Detector System, AMY Note 272.

[26] Y.K.Li *et.al.* , Trigger Summary, AMY Note 272.

[27] T. Sjostrand *et.al.* , Com. Phys. Comm., **27**,243(1982); Com. Phys. Comm. **28**, 229(1983); Com. Phys. Comm., **43**,367(1982).

[28] B. Anderson *et.al.* , Phys. Rep. **97**, 33 (1983).

[29] W. Bartel *et.al.* (JADE), Phys. Lett. **B101**,129(1981); W. Bartel *et.al.* (JADE), Z. Phys. **21**,37(1983); W. Bartel *et.al.* (JADE), Phys. Lett. **B157**,340(1985); H. Aihara *et.al.* (TPC), Z. Phys. **28**,31 (1985); M. Althoff *et.al.* (TASSO), Z. Phys. **29**,29(1985).

[30] W.R. Nelson *et.al.* , "The EGS4 code System", SLAC Report, 265(1985).

[31] A. Grant, Nucl. Instr. Meth., **131**,167(1975).

[32] Review of Particle Properties, Phys. Letts. **B204**(1988)pp.165-221.

[33] F.F.Field and R.P.Feynman, Nucl. Phys. **B136**(1978)1.

[34] H.W.Zheng *et.al.* (AMY collab), KEK Preprint-90-5, Apr 1990.

[35] H. Sagawa, Selection of multihadronic events, AMY note 382; T.Kumita *et.al.* (AMY collab.), KEK-Preprint-89-188; T.Mori *et.al.* (AMY collab.), Phys. Lett. **B218**(1989)499.

[36] T. Mori, Doctoral Thesis, University of Rochester (1989)p.66.

[37] D.G. Cassel and M. Ogg, "DUET - a Track-Finding Program for Cylindrical Geometries", CLEO Internal Report (1983).

[38] T. Mori, Doctoral Thesis, University of Rochester (1989)p.66.

[39] S. Igarashi, developed the CDC extrapolation program. Source file resides in the TRISTAN mainframe computer (FACOM),1987.

[40] F.A. Harris *et.al.* Nucl. Instrum. Meth. **103**, 345(1972).

[41] T. Kumita, AMY Note 544.

[42] Carrol *et.al.* , Phys.Lett. **B80**(1979)319.

[43] K. Kato and T Munehisa, KEK Report 84-18 (1984).

[44] M. Derrick *et.al.* (HRS), Phys. Rev. D, **35**,2639(1987); H. Schellman *et.al.* (MARK II), Phys. Rev. D,**31**,3013(1985); R. Brandeli *et.al.* (TASSO), Phys. Lett. **B94**,91(1980); M. Althoff *et.al.* (TASSO), Z Phys. **C27**,27(1985); H. Aihara *et.al.* (TPC), Phys. Rev. Lett., **53**,2378(1984); Ch. Berger *et.al.* (PLUTO), Phys. Lett., **B104**,79(1981); W. Bartel *et.al.* (JADE), Z Phys., **C20**,187(1983)].

[45] TOPAZ and VENUS prelimary results (unpublished).

[46] T. Mori, Doctoral Thesis, University of Rochester (1989)p.71.

[47] T. Sjöstrand and M. Bengtsson, Comput. Phys. Commun. **43**, (1987) 367.

[48] David Stuart, Private communication, 1990.

[49] S.K. Kim, Doctoral Thesis, Korea University (1988)pp.52-61; T. Mori, Doctoral Thesis, University of Rochester (1989)pp.70-71.

[50] F.A.Harris *et.al.* Nuclear Instrum. Meth. **103**(1972)345.

[51] M.Derrick *et.al.* (HRS), Phys. Rev. D,**35**(1987)2639; H.Schellman *et.al.* (MARK II), Phys. Rev. D,**31**(1985)3013; R.Brandelik *et.al.* (TASSO), Phys. Lett.,**B94**(1980)91; M.Aihara *et.al.* (TASSO), Z Phys.,**C27**(1985)27; C.Berger *et.al.* (PLUTO), Phys. Lett.,**B104**(1981)79; W.Bartel *et.al.* (JADE), Z Phys.,**C20**(1983)187; VENUS and TOPAZ collaboration (unpublished).

[52] T.Bowcock *et.al.* (CLEO collab.), Phys.Rev.**D38**(1988)2679.

[53] W.Bartel *et.al.* (JADE collab.), Phys. Lett. **B146** (1984) 437; M.Althoff *et.al.* (TASSO collab.), Phys. Lett.**B146** (1984) 443; C.Kiesling, in Proceedings of the 29th Moriond Conference, March,1989; F.Ould-Saada, DESY report 88-177 (1988); H.R.Band *et.al.* (MAC collab.), Phys. Lett. **B218** (1989) 369; C.R.Ng *et.al.* (HRS collab.), ANL-HEP-PR-88-11; S.L.Wu, Nucl.Phys.B (Proc.Suppl.) 3 (1988).

[54] M.Artuso *et.al.* (CLEO collab.), Phys. Rev. Lett. **62**(1989)2233; H.Albrecht *et.al.* (ARGUS), Phys. Lett. **B192**(1987)245; T.Schaad *et.al.* (MARK II), Phys. Lett., **B160**(1985)188; W.Bartel *et.al.* (JADE), Phys. Lett.,**B146**(1984)437; H.Band *et.al.* (MAC), Phys. Lett.,**B218**(1989)369.

[55] AMY Collaboration. TRISTAN Proposal for study of e^+e^- Interactions with a High Luminosity, High Resolution Lepton Detector, November 1984, p.19.

[56] T.Schaad *et.al.* (MARK II), Phys. Lett., **B160**(1985)188.

[57] W.Bartel *et.al.* (JADE), Phys. Lett.,**B146**(1984)437.

[58] H.Band *et.al.* (MAC), Phys. Lett.,**B218**(1989)369.

[59] AMY Collaboration. TRISTAN Proposal for Study of e^+e^- Interactions with a High Luminosity, High Resolution Lepton Detector, TRISTAN-EXP-003, November 1984.

Appendix A: The AMY Collaboration

J. Lim,[a] R. Imlay,[a] P. Kirk,[a] R.R. McNeil,[a] W. Metcalf,[a] S.S. Myung,[a] C.P. Cheng,[b] P. Gu,[b] J. Li,[b,g] Y.K. Li,[b] M.H. Ye,[b] Y.C. Zhu,[b] A. Abashian,[c] K. Gotow,[c] K.P. Hu,[c] E.H. Low,[c] M.E. Mattson,[c] L. Pillonen,[c] K.L. Sterner,[c] S. Lusin,[d] C. Rosenfeld,[d] A.T.M. Wang,[d] S. Wilson,[d] M. Frautschi,[e] H. Kagan,[e] R. Kass,[e] C.G. Trahern,[e] R.E. Breedon,[f,g] G.N. Kim,[f] Winston Ko,[f] R.L. Lander,[f] K. Maeshima,[f] R.L. Malchow,[f] J. Rowe,[f] J.R. Smith,[f] D. Stuart,[f] K. Abe,[g] Y. Fujii,[g] Y. Higashi,[g] S.K. Kim,[g] Y. Kurihara,[g] A. Maki,[g] T. Nozaki, [g] T. Omori,[g] H. Sagawa,[g] Y. Sakai,[g] Y. Sugimoto,[g] Y. Takaiwa,[g] S. Terada,[g] R. Walker,[g,n] F. Kajino,[j] R. Poling,[j] T. Thomas,[j] Y. Ishi,[k] K. Miyano,[k] H. Miyata,[k] T. Sasaki,[k] Y. Yamashita,[l] A. Bacala,[m,n] J. Liu,[m] F. Sannes,[m] S. Schnetzer,[m] R. Stone,[m] J. Vinson,[m] P. Auchincloss,[o] D. Blanis,[o] A. Bodek,[o] H. Budd,[o] S. Eno,[o] C.A. Fry,[o,g] H. Harada,[o] Y.H. Ho,[o] B.J. Kim,[o] Y.K. Kim,[o] T. Kumita,[o] S.L. Olsen,[o,h] N.M. Shaw,[o] A. Sill,[o] E.H. Thorndike,[o] K. Ueno,[o] C. Velissaris,[o] H. W. Zheng,[o] S. Kobayashi,[p] A. Murakami,[p] J.S. Kang,[q] H.J. Kim,[q] M.H. Lee,[q] D.H. Han,[r] E.J. Kim,[r] D. Son,[r] T. Kojima,[s] S. Matsumoto,[s] R. Tanaka,[s] Y. Yamagishi,[s] T. Yasuda,[s] T. Ishizuka,[u] and K. Ohta[u]

[a] Louisiana State University, Baton Rouge, LA 70803

[b] Institute for High Energy Physics, Beijing

[c] Virginia Polytechnic Institute and State University, Blacksburg, VA 24061

[d] University of South Carolina, Columbia, SC 29208

[e] Ohio State University, Columbus, OH 43210

[f] University of California, Davis, CA 95616

[g] KEK, National Laboratory for High Energy Physics, Ibaraki 305

[h] Tsukuba University, Ibaraki 305; [i] Konan University ,Kobe 658

[j] University of Minnesota, Minneapolis, MN 55455

[k] Niigata University, Niigata 950-21

[l] Nihon Dental College, Niigata 951

[m] Rutgers University, Piscataway, NJ 08854

[n] University of the Philippines, Quezon City, 3004

[o] University of Rochester, Rochester, NY 14627

[p] Saga University, Saga 840; [q] Korea University, Seoul 132

[r] Kyungpook National University, Taegu 635; [s] Chuo University, Tokyo 112

[t] Tokyo Institute of Technology, Tokyo 152

[u] Saitama University, Urawa 338

Appendix B

Monitoring the performance of the MUO

TRISTAN "physics runs" occur three or four times each year, with each running period lasting for a few months. Cosmic ray data are collected before the beginning of a running period to determine the efficiency of the muon chamber. Dead or noisy channels are repaired whenever feasible.

During the run, physicists are on shift 24 hours a day to monitor the performance of the detector. The MUO gas system and power supplies are checked three times a day. The online VAX computer monitors fluctuations in the MUO high volatge (HV) and automatically ramps the HV up to the operating voltage of 3,100 volts at the beginning of a "fill" and lowers it to 2,000 volts at the end of the fill. A fill refers to the injection of the e^+ and e^- beams into the Main Ring, and subsequent acceleration of the beams to the targeted center-of-mass energy. The beams are dumped at the end of the fill when their currents become too low. Each fill typically last fromo one to three hours. An audible alarm is set off whenever the HV current exceeds a predetermined level and the HV is turned off automatically to prevent damage. This may happen if a drift chamber wire is broken causing a short-circuit or by less catastrophic occurrences such as accelerator noise bursts. At the end of a fill, the online system gives an end-of-run summary. The MUO efficiency is monitored by using cosmic rays obtained during the cosmic ray gate between beam crossing. This efficiency is reported in the end-of- run summary. Any abnormalities

are reported to the person-in-charge of the MUO. A more thorough diagnostic of the MUO is done off-line by running a program which plots the wire and counter hits in the MUO. Figure B.1 shows a diagnostic plot of the MUO using this program. The plot is used to monitor the performance of individual channels and dead or noisy channels are fixed whenever possible. For example, the plot shows that channel 63 in sextant 3 layer 1 is dead.

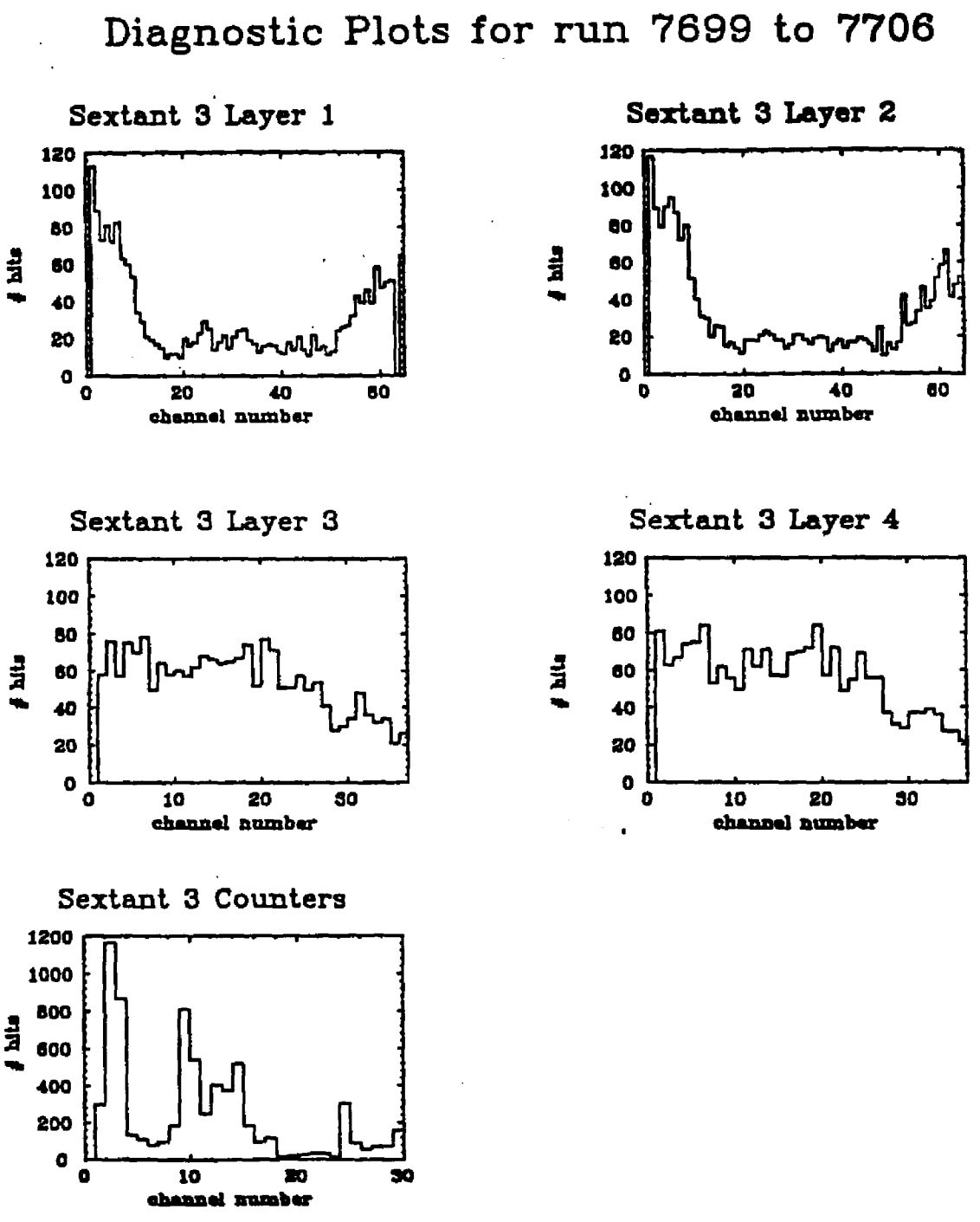

Figure B.1: Diagnostic plot of MUO

Appendix C

Where was I in the scheme of things?

The AMY detector cost in excess of $12 million and took two and a half year to design, construct and assembe. It involves the effort of more than 100 physicists and graduate students from 20 institutions. [see appendix A].

A successful collaboration of such a scale necessitates the distribution of responsibilitites for funding, construction, maintenance and data analysis. Table C.1 shows the institutions responsible for fabrication and funding of the major components [59].

Many of the components were built in the United States and shipped to KEK for assembly and installation. For instance, during the construction phase, the LSU group set up a laboratory in the basement of Nicholson Hall at LSU for the manufacture of the electronic end-boards for the muon chambers.

I arrived at KEK during the data taking phase and my hardware responsibilities was mainly in the maintenance and repair of the muon drift chambers. I was the on-site person from LSU who was responsible for the muon drift chambers, including the muon gas system and electronics. I repaired and replaced broken electronic end-boards, broken drift chamber anode wires, restored dead channels and repaired noisy ones. I have also performed repairs on the muon scintillation counters. During data taking runs, I was "on call" 24 hours a day to fix any problems related to the muon drift chambers. In addition, like all on-site personnel, I took the normal twice

	Item	Group Responsible	Funding Institution
1.	Beam Pipe		
	a) Background Calculation	On-Site Group	
	b) Radiation Masks	On-Site Group	KEK
	c) Vacuum Pumps	On-Site Group	KEK
	d) Beryllium Tube	Rochester	Rochester
	e) Detailed Design	On-Site Group	
2.	Luminosity Monitor	Saga University	KEK
3.	Veto Chambers	On-Site	KEK
4.	Central Drift Chamber		
	a) Hardware Construction	Rochester	Rochester
	b) Electronics & Cabling	Rochester	Rochester
5.	Trigger Scintillators	On-Site	KEK
6.	X-ray Detector	Niigata/On-Site	KEK
7.	Shower Counter		
	a) Pb Panel Fabrication	VPI	VPI
	b) Cathode Etching	UC (Davis)	UC (Davis)
	c) Assembly	Rutgers	Rutgers
	d) Cabling & Electronics	Rutgers	Rutgers

continue next page

	Item	Group Responsible	Funding Institution
8.	Magnet		
	a) Coil & Cryostat	On-Site	KEK
	b) Iron	On-Site	KEK
	c) Cryogenic System	On-Site	KEK
	d) Power Supply	On-Site	KEK
9.	Muon Detector		
	a) Purchase Extrusions	LSU	LSU
	b) Assembly and Test	LSU/TIT	LSU/TIT
	c) Scintilation Counters	LSU	LSU
	d) Electronics	LSU	LSU
10.	Low-β Quadrapoles	On-Site	KEK
11.	Data Acquisition		
	a) On Line Computer	Rochester	Rochester
	b) CAMAC & FASTBUS Interfaces	On-Site	Rochester
	c) Rack cooling scheme	On-Site	
	d) Trigger Electronics	OSU	OSU
12.	Experimental Hall	On-Site	KEK
13.	Electroincs Hut	On-Site	KEK
14.	Analysis		
	a) Monte Carlo	On-Site	
	b) Data Logging System	On-Site	
	c) Off line analysis	On-Site	
	d) Display System	On-Site	

Table C.1: Responsibilities for fabrication and funding of AMY

a week eight-hour shift to monitor and operate the detector. The shifts consists of two people who stay in the electronics hut to begin and end data taking for each fill, calibrate the pedestals for the electromagetic shower counters and check the end of run summary generated by the computerized detector monitoring system for any malfunctions or inefficiencies. Shift personnel also scan the events collected to look for possible interesting physics events and detector problems.

The physics topics that are of interest at AMY include:

1. The test of the standard model.
2. Tests for substructure of photons and leptons.
3. Searches for new particles.

Various off-line analysis groups were organized to concentrate on the different aspects of these physics goals. I was active in the multi-hadronic inclusive lepton group. This is one of the principal groups since AMY was optimized for lepton identification. One of my tasks was to study the efficiencies for inclusive muon detection and maintain the software for muon selection. The hadronic events were scanned one at a time to be sure that the software was doing its job in selecting muon events as designed. The scanning also noted for improper reconstruction of tracks and the information was fed back to the person in charge of the track reconstruction program.

The AMY collaboration, up to May 1990, has published 15 papers in professional

journals such as Physical Review Letters, Physical Review D and Physics Letters. In addition another twenty papers were contributed to international conferences.

In order to maintain a high standard in the results, drafts of papers intended for publication in professional journals are made available to all collaborators for comment and queries. Presentations are also given by the people who did the main analysis during the weekly and monthly group meetings. These presentations include detailed explanations of the method used in the analysis and the results obtained. In addition the proposed paper has to be approved by two internal referees before it can be submitted for publication.

Representatives of the AMY collaboration have also been active in giving numerous talks at local and international conferences, symposiums, summer schools, and annual meetings of the Japan Physical Society, Korean Physical Society and American Physical Society. The results have to be given at one of the AMY group meetings before presentation to outside meetings. All these measures are designed to maintain a high standard for results from AMY.

As a representative of this collaboration I have presented the results of the measurement of A_b and R_b at various AMY meetings while I was in Japan and the United States and at the Japan Physical Society Spring meeting in 1989.

The results for the measurement of the $e^+e^- \rightarrow b\bar{b}$ cross-section and forward-backward charge asymmetry from the 52 GeV to 57 GeV data sample were published in Physical Review Letters **63**(1989)2341. I updated the results to include

data up to 61.4 GeV as described in this dissertation and for the 25th International Conference for High Energy Physics to be held in Singapore starting August 2, 1990.

Vita

The author, Jit Ning Lim, was born in 1960 in Singapore, a first generation Singaporean whose parents emigrated from Hainan Island off mainland China. He received his B.S. degree from the National University of Singapore in 1984 and B.S.(with Honors) the following year. He attended graduate school at Louisiana State University in 1985 and received his M.S. in 1986. He began working on the AMY experiment at KEK in Tsukuba, Japan, in 1988. In 1990 he returned to the United States where he received his PhD degree in Physics.

DOCTORAL EXAMINATION AND DISSERTATION REPORT

Candidate: Jit Ning Lim

Major Field: Physics

Title of Dissertation: Measurement of e^+e^- --> $b\bar{b}$ Forward-Backward Charge Asymmetry

Approved:

Major Professor and Chairman

Dean of the Graduate School

EXAMINING COMMITTEE:

Date of Examination:

10 July 1990